2021 Workshop on Innovative Nanoscale Devices and Systems

Marriott Waikoloa – Kohala Coast, Big Island, Hawaii, USA

November 28 – December 3, 2021

Book of Abstracts

The 2021 Workshop on Innovative Nanoscale Devices and Systems (WINDS2021) was held November 28 – December 3, 2021, at the Waikoloa Beach Marriott Resort & Spa, Hawaii, USA.

WINDS is a week-long, international, and interactive workshop designed to explore the fundamental properties of nanoscale devices and applications thereof. In particular, WINDS provides a forum for material, device, and characterization as well as experimental and modeling researchers to interact.

The program consists of invited talks and regular talks. All contributions have been peer-reviewed by the program committee.

This workshop is composed of morning and evening sessions, with afternoons free for ad hoc meetings to encourage extended interaction and discussion among participants. It is the successor of the original WINDS and the International Symposium on Advanced Nanodevices and Nanotechnology (ISANN), which were held on alternate years. WINDS itself began as an outgrowth of the successful Advanced Heterostructures Workshop, which has a long history dating from the 1980s.

WINDS 2021 is an AVS Sponsored Topical Conference. The conference committee greatly appreciates the support.

© 2021 Institute for Microelectronics, TU Wien

Gußhausstraße 27-29, 1040 Wien, Austria

978-3-9504738-3-4

Conference Chairs

General Chair:	Tomoki Machida	University of Tokyo, Japan
Europe Co-Chair:	Jaroslav Fabian	University of Regensburg, Germany
US Co-Chair:	John Conley	Oregon State University, USA
Japan Co-Chair:	Akira Oiwa	Osaka University, Japan
Communications Chair:	Josef Weinbub	TU Wien, Austria
Local Arrangements:	Stephen Goodnick	Arizona State University, USA

Program Committee

Alexander Balandin, University of California, Riverside, USA

David K. Ferry, Arizona State University, USA

Matthew Gilbert, University of Illinois Urbana-Champaign, USA

Koji Ishibashi, RIKEN, Japan

Satoshi Iwamoto, University of Tokyo, Japan

David Janes, Purdue University, USA

Berend (Berry) Jonker, Naval Research Lab, USA

Victor Klimov, Los Alamos National Laboratory, USA

Valeria Lauter, Oak Ridge National Laboratory, USA

Saulius Marcinkevicius, KTH, Sweden

Kazuhiko Matsumoto, Osaka University, Japan

Wolfgang Porod, University of Notre Dame, USA

Viktor Sverdlov, TU Wien, Austria

Igor Zutic, University at Buffalo, USA

978-3-9504738-3-4

Workshop on Innovative Nanoscale Devices and Systems (WINDS2021)
Marriott Waikoloa – Kohala Coast, Big Island, Hawaii, USA
November 28 – December 3, 2021

Sunday, November 28

15:00-18:00 Registration *Outside Naupaka Salon 2*

18:00-20:00 Gala Reception *Paniolo Ocean Terrace*

Monday, November 29 *Naupaka Salon 4*

7:00-12:00 Registration *Outside Naupaka Salon 2*

Opening Welcome
9:00-9:15 Introductions Stephen Goodnick

Session 1: 2D Materials I: Excitonic properties
Session Chair: Alexander Balandin

9:15-9:45 (invited) Controlling excitons in 2D semiconductor heterostructures and hybrid plasmonic structures
J. R. Schaibley
University of Arizona, USA

9:45-10:00 First-principles calculations of minimally twisted $MoSe_2/WSe_2$ bilayers
M. Phillips and C. S. Hellberg
Naval Research Laboratory, USA

10:00-10:15 Single Photon Emitters in Monolayer WSe_2 by Nano-indentation
B. T. Jonker
Naval Research Laboratory, USA

10:15-10:30 Cavity exciton-polaritons in two-dimensional semiconductors from first principles
V. Despoja and D. Novko
Institute of Physics, Croatia

10:30-10:45 Watching Matter Move: Investigation of 2D half van der Waals heterostructures materials
F. Niefind, C. Dong, R. A. Maniyara, J. A. Robinson and S. Pookpanratana
National Institute of Standards and Technology, USA, University of Maryland, USA, Pennsylvania State University, USA

10:45-11:00 Monolayer borophene on Ir(111): Segregation-enhanced epitaxy and electrochemical transfer

978-3-9504738-3-4

M. Petrović , K. M. Omambac , B. Radatović , S. Kamal, V. Jadriško, P. Dreher, D. Janoschka, C. Brand , M. A. Kriegel , N. Hartmann , N. Vujičić , M. Kralj , F. J. Meyer zu Heringdorf , and M. Horn-von Hoegen
Institute of Physics, Croatia, University of Duisburg-Essen, Germany, Interdisciplinary Center for Analytics on the Nanoscale (ICAN), Germany, University of Duisburg-Essen Germany

11:00-11:30 Coffee break *Naupaka Lanai*

Session 2: Spintronics
Session Chair: Igor Zutic

11:30-12:00 (invited) Spintronic studies of ferrimagnetic and antiferromagnetic Weyl semimetals
Eric E. Fullerton
University of California, USA

12:00-12:15 Spin and Charge Drift-Diffusion Approach to Torque Computation in Spintronic Devices
S. Fiorentini , R. Lacerda de Orio , S. Selberherr , J. Ender , W. Goes , and V. Sverdlov
TU Wien, Austria, Silvaco Europe Ltd.,United Kingdom

12:15-12:30 Spin-orbit torque facilitated switching of topological insulator/ferromagnet heterostructures
M. A. Noyan , O. M. J. van 't Erve , C. H. Li , X. Zhang , J. Moon , M. Lohmann , E. Cobas , and B. T. Jonker
Naval Research Laboratory, USA

12:30-13:00 Magnetic diode type effect in artificial honeycomb lattice due to magnetic charge correlation
D. K. Singh , V. Lauter , G. Yumnam , Y. Chen and J. Guo
University of Missouri, USA, Oak Ridge National Laboratory, USA

13:00-19:00 Lunch and Ad Hoc Sessions: Free Time

18:30-19:30 Registration *Outside Naupaka Salon 2*

19:00-21:00 Beverages/Light Snacks *Naupaka Salon 3/Lanai*

Session 3: Optoelectronics and novel devises
Session Chair: Josef Weinbub

19:00-19:15 GeSn alloys on Si (100): A versatile platform for electronic and optical devices
D. Grützmacher , D. M. Buca , Q.-T. Zhao
Peter Grünberg Institute-9, Germany, JARA-Institute for Green-IT, Peter Grünberg Institute 10, RWTH Aachen University, Germany

19:15-19:30 Real-Time Quantum Dynamics of Long-Range Electronic Excitation Transfer in Plasmonic Nanoantennas
B. M. Wong
University of California, USA

978-3-9504738-3-4

19:30-19:45 Thermoelectric Nanoantennas for Mid- and Far-Infrared Detection
G. P. Szakmany , G. H. Bernstein , A. O. Orlov , E. C. Kinzel , and W. Porod
University of Notre Dame, USA

19:45-20:00 Enhanced Light-Matter Interactions in Shape-Engineered Silicon Phononic – Photonic Superlattice Structures
F. Kargar, C.-Y. Tammy Huang, and A. A. Balandin
University of California, USA

20:00-20:15 Infrared Photodetection Using Narrow Bandgap Conjugated Polymers
J. D. Azoulay
University of Southern Mississippi, USA

20:15-20:30 Improving MIM Diode Performance with Precisely Placed ALD Ti Defects
K.E.K. Holden, B. M. Kupp, J. Peterson, and J.F. Conley, Jr.
Oregon State University, USA

20:30-20:45 Optimization of matching networks for nanoscale charge and voltage sensors using reflectometry
M. Huebner, J. Chisum, A. O. Orlov, and G. L. Snider
University of Notre Dame, USA

Tuesday, November 30 *Naupaka Salon 4*

7:00-12:00 Registration *Outside Naupaka Salon 2*

Session 4: New approaches to solar energy conversion
Session Chair: Victor Klimov

9:00-9:30 (invited) Quantization of Semiconductor Nanostructures and Singlet Fission: Applications to Future Approaches for Highly Efficient Solar Photon Conversion to PV and Solar Fuels
Arthur J. Nozik
University of Colorado, USA, National Renewable Energy Laboratory (NREL), USA

9:30-10:00 (invited) Controlling photons and electromagnetic waves for energy applications
Shanhui Fan
Department of Electrical Engineering and Ginzton Laboratory, Stanford University, USA

10:00-10:30 (invited) Valley photovoltaics: A new approach towards the hot carrier solar cell
H. Esmaeilpour , K. R. Dorman, D. K. Ferry , V. R. Whiteside , J. Tang , T. D. Mishima, M. B. Santos , and I. R. Sellers
University of Oklahoma, USA, Arizona State University, USA

10:30-10:45 Seeking Nirvana (Hot Carrier Solar Cells)
D. K. Ferry
Arizona State University USA

10:45-11:00 Hot phonon and intervalley effects on the steady-state temperature of electrons in InGaAs Multi-Quantum Wells

978-3-9504738-3-4

Y. Zou , H. Esmaielpour , D. Suchet , J.-F. Guillemoles , S. M. Goodnick
Arizona State University, USA, CNRS-Institut Photovoltaique d'Ile de France (IPVF), France, CNRS-Ecole Polytechnique, France

11:00-11:15 An entertaining physics: On the possibility of energy storage enhancement in electrostatic capacitors using the compensational inductive electric field.
Alexander Khitun
University of California, USA

11:15-11:45 Coffee break *Naupaka Lanai*

Session 5: Optical devices and quantum dots
Session Chair: Valeria Lauter

11:45-12:00 Sensing with Quantum Cascade and Interband Cascade Devices
Gottfried Strasser
Technische Universität Wien, Austlia

12:00-12:15 Recent Progress Toward Colloidal Quantum Dot Laser Diodes
H. Jung, N. Ahn, Y.-S. Park, I. Fedin, C. Livache, and V. I. Klimov
Los Alamos National Laboratory, USA

12:15-12:30 Controlling the parity and time-reversal symmetry of non-Hermitian graphene Dirac plasmons and its application to terahertz lasers
T. Otsuji , A. Satou , H. Fukidome , M. Ryzhii , R. Victor , and K. Narahara
Tohoku University, Japan, University of Aizu, Japan, Kanagawa Inst. of Technology, Japan

12:30-19:00 Lunch and Ad Hoc Sessions: Free Time

18:30-19:30 Registration *Outside Naupaka Salon 2*
19:00-21:00 Beverages/Light Snacks *Naupaka Salon 3/Lanai*

Session 6: Memory, sensor, novel devices
Session Chair: Stephen Goodnick

19:00-19:30 (invited) Topological defect dynamics in ultrafast energy efficient charge configuration memory devices.
A. Mraz , R. Venturini , M. Diego , A. Kranjec , D. Svetin , Y. Gerasimenko , J. Ravnik , I. Vaskivskyi , D. Kazazis , Y. Ekinci , R. Sobolewski, and D. Mihailovic
Jozef Stefan Institute, Slovenia, CENN Nanocenter, Slovenia, University of Ljubljana, Slovenia, LMN-Paul Scherrer institute, Switzerland, University of Rochester, USA, Brimrose Technology Corporation, USA

19:30-19:45 Nanocryotron-driven Charge Configuration Memory
A. Mraz , V. V. Kabanov , and D. Mihailovic
Jozef Stefan Institute, Slovenia, University of Ljubljana, Slovenia

978-3-9504738-3-4

19:45-20:00 Sub-2-picosecond, sub-2 fJ/bit resistance switching between charge ordered phases with a single picosecond electrical pulse
R. Venturini , A. Mraz , I. Vaskivskyi , D. Svetin , S. B. Trivedi , J. Cheng , R. Sobolewski , and D. Mihailovic
Jozef Stefan Institute, Slovenia, CENN Nanocenter, Slovenia, University of Ljubljana, Slovenia, University of Rochester, USA, Brimrose Technology Corporation, USA

20:00-20:15 Rapid, multianalyte detection of opioid metabolites in wastewater
N. Kumar , M. Geiwitz , M. Rana , N. I. Khan , M. Catalano , J. C. Ortiz-Marquez , H. Kitadai , A. Weber , B. Dweik , X. Ling , T. van Opijnen , A. Argun , K. S. Burch
Boston College, USA, Giner Inc., USA, Boston University, USA

20:15-20:30 NEMS Devices to Enable Adiabatic Reversible Computing
R. Celis-Cordova, A. F. Brown, J. J. Gose, A. O. Orlov, and G. L. Snider
University of Notre Dame, USA

20:30-20:45 “Wiring-Up” Atom-Defined Device Elements: Ever Closer to Operational Ultra-Fast, Ultra-Low Power Circuits
R.Wolkow , J.Pitters , J. Onada , A.Khademi , T.Chutora , C.Leon , F.Altincicek , J.Croshaw , L.Livadaru , M.Salomons , M.Cloutier , M.Yuan , R.Achal , S.Yong , S.Bukhari
University of Alberta, Canada, National Research Council of Canada Nanotechnology Research Centre, Canada

20:45-21:00 TCAD Simulation of Novel Semiconductor Devices with NESS
A. Asenov
Glasgow University, UK, Semiwise Ltd., UK

21:00-21:15 Electron Quantum Optics for Quantum Interference Logic Devices
J. Weinbub , M. Ballicchia , and M. Nedjalkov
Institute for Microelectronics, TU Wien, Austria

Wedenesday, December 1 *Naupaka Salon 4*

7:00-12:00 Registration *Outside Naupaka Salon 2*

Session 7: Topological properties in the normal and superconducting state
Session Chair: Matthew Gilbert

9:00-9:30 (invited) Novel Topological Kink States with Spin-Valley-Momentum Locking
T. Zhou , S. Cheng , M. Schleenvoigt , P. Schüffelgen , H. Jiang , Z. Yang and I. Žutić
University at Buffalo, USA, Northwest University, China, Peter Grünberg Institute 9, Germany, School of Physical Science and Technology, Soochow University, China, Fudan University, China

9:30-9:45 Designer Topological Magnetic Materials
G.J. de Coster and M.J. Gilbert

978-3-9504738-3-4

Army Research Laboratory, USA, University of Illinois at Urbana-Champaign, USA

9:45-10:00 Towards Non-Abelian Statistics in Topological Planar Josephson Junctions
T. Zhou , M. C. Dartiailh , K. Sardashti , J. E. Han , A. Matos-Abiague , J. Shabani , and I. Žutić
University at Buffalo, USA, Center for Quantum Phenomena, Department of Physics, USA , Wayne State University Detroit, USA
University at Buffalo, State University of New York, USA, New York University, USA, Wayne State University, USA

Session 8: Oxide
Session Chair: Matthew Gilbert

10:00-10:15 Ultrafast carrier dynamics in β-Ga_2O_3
S. Marcinkevičius and J. S. Speck
AlbaNova University Center, Sweden, University of California, USA

10:15-10:30 Influence of microstructure on electrical properties of titanium dioxide thin films
K. Kulinowski , M. Radecka , and B. J. Spisak
AGH University of Science and Technology, Poland

10:30-10:45 Ultrathin MoO_3 (010) films grown by MBE on stepped c-plane sapphire
P. Novotný, A. J. Pedersen, and H. H. Lamb
North Carolina State University, USA

10:45-11:00 Dynamically tunable single-layer VO_2/metasurface based THz cross-polarization converter
R. Yahiaoui , Z.A. Chase , C. Kyaw , E. Seabron , J. Mathews , and T.A. Searles
University of Illinois at Chicago, USA, Morehouse College, USA, Howard University, USA

11:00-11:30 Coffee break *Naupaka Lanai*

Session 9: 2D Materials II: Carrier induced effects
Session Chair: John Conley

11:30-12:00 (invited) Relaxation and darkening of excitonic complexes in electrostatically-doped monolayer semiconductors
M. Yang , L. Ren , C. Robert , D. Van Tuan , L. Lombez , B. Urbaszek , X. Marie , and H. Dery
University of Rochester, USA, Universite de Toulouse, France

12:00-12:15 Modulation Doping in 2D Materials
K.S. Burch
Boston College, USA

12:15-12:30 Controlling interfacial charge transfer in two-dimensional van der Waals heterostructures
H. Zhao
The University of Kansas, USA

12:30-12:45 Ab-initio Calculations of Edge States in Topological 1T′ MoS_2 Nanoribbons
Al-Moatasem El-Sayed , H. Seiler , H. Kosina , S. Selberherr , and V. Sverdlov
Institute for Microelectronics, TU Wien, Austria

978-3-9504738-3-4

12:45-18:30 Lunch and Ad Hoc Sessions: Free Time

18:30-20:30 **Luau Reception and Dinner** *Paniolo Ocean Terrace*

Thursday, December 2 *Naupaka Salon 4*

7:00-12:00 Registration *Naupaka Foyer*

Session 10: Spintronics, topology, 2D CDW materials
Session Chair: David K. Ferry

9:00-9:30 (invited) Chiral spin textures and chiral spin-orbit torques for spintronic memories
Stuart S.P. Parkin
Max Planck Institute for Microstructure Physics, Germany

9:30-10:00 (invited) Topology and Chirality
Claudia Felser
Max Planck Institute Chemical Physics of Solids, Germany

10:00-10:15 Depinning and Phase Transitions in 2D Charge-Density-Wave Quantum Materials – Prospects for Applications in Beyond-CMOS Electronics
A. Mohammadzadeh , A. Rehman , F. Kargar , S. Rumyantsev and A.A. Balandin
University of California, USA, Polish Academy of Sciences, Poland

10:15-10:30 Room Temperature Higgs mode Quantum Pathway Interference in 2D Charge Density Wave materials
Y. Wang , S. Lei , L. M. Schoop , and K. S. Burch
Boston College, USA, Princeton University, USA

10:30-11:00 Coffee break *Naupaka Lanai*

Session 11: 2D Materials III: Future device applications
Session Chair: Berend T. Jonker

11:00-11:30 (invited) Two-Dimensional Semiconductors and Heterostructures for Advanced Logic, Memory and Photonics
Deep Jariwala
University of Pennsylvania, USA

11:30-12:00 (invited) Electronic Transport in Strain-Engineered Graphene
Nadya Mason
University of Illinois at Urbana-Champaign, USA

12:00-12:15 Novel Multilayer Architectures Based on Epitaxial Graphene

978-3-9504738-3-4

B. Pielić , C. Busse , K. Watanabe , and M. Kralj
Institute of Physics, Croatia
Universität Siegen, Germany, Kyoto University, Japan

12:15-12:30 One-Dimensional van der Waals Quantum Materials as Efficient Fillers for Multifunctional Composites – Applications in Electromagnetic Shielding
Z. Barani , F. Kargar , Y. Ghafouri , S. Rumyantsev , K. Godziszewski , G. Cywiński , Y. Yashchyshyn , T.T. Salguero and A.A. Balandin
University of California, USA, University of Georgia, USA, Polish Academy of Sciences, Poland, Warsaw University of Technology, Poland

12:30-19:00 Lunch and Ad Hoc Sessions: Free Time

13:00-14:30 Committee Luncheon

19:00-21:00 Beverages/Light Snacks *Naupaka Salon 3/Lanai*

Session 12: Quantum transport, novel devices
Session Chair: Igor Zutic

19:00-19:30 (invited) Observation of the Kondo screening cloud
M. Yamamoto and I. V. Borzenets
RIKEN Center for Emergent Matter Science, Japan, Texas A&M University, USA, City University of Hong Kong, Hong Kong

19:30-19:45 Transport in helical Luttinger liquids in the fractional quantum Hall regime
Y. Wang , V. Ponomarenko , Z. Wan , K. W. West , K. W. Baldwin , L. N. Pfeiffer , Y. Lyanda-Geller , and L. P. Rokhinson
Purdue University, USA, Ioffe Physico-Technical Institute, Russia, Princeton University, USA, Purdue University, USA

19:45-20:00 Biased distributions of random quantum states for high-performance quantum state reconstruction
S. Lohani, J. M. Lukens, D. E. Jones, T. A. Searles, R. T. Glasser, and B. T. Kirby
Howard University, USA, Tulane University, USA, Oak Ridge National Laboratory, USA, United States Army Research Laboratory, USA, Massachusetts Institute of Technology, USA

20:00-20:30 (invited) Ballistic Multiterminal Graphene Josephson Junctions
E. A. , T. Larson , L. Zhao , A. Seredinski , A. Draelos , T. Taniguchi , K. Watanabe , I. V. Borzenets , F. Amet , and G. Finkelstein
Duke University, USA, NIMS, Japan, TAMU, USA, Appalachian State University, USA

978-3-9504738-3-4

Friday, December 3 *Naupaka Salon 4*

Session 13: Wide-gap semiconductor
Session Chair: Berend T. Jonker

9:00-9:30 (invited) Substitutional or Charge Transfer Doping of Diamond for High Current PIN Diodes and Dielectric Diamond Channel Structures
R. J. Nemanich , H. Surdi , M. Malakoutian , Y. Yang , Y. Yao , X. Wang , F. A. Koeck , S. Chowdhury , and S Goodnick
Arizona State University, USA, Univ. of California, USA

9:30-9:45 High-Power Diamond Schottky P-I-N Diodes for Non-Linear RF Applications
V. Jha , H. Surdi , F. A. Koeck , R. J. Nemanich , S. M. Goodnick , and T. J. Thornton
Arizona State University, USA

9:45-10:00 Low-Field Electron Mobility in AlGaN/GaN Nano-FinFETs
V. N. Kumar , D. Vasileska and M. Povolotskyi
Arizona State University, USA, Jacobs Corporation, USA

10:00-10:15 Impact Ionization and Breakdown in Ultra-Wide Bandgap Materials
J. Shoemaker , R. Vatan , R. Nemanich , R. Kaplar , and S. Goodnick
Arizona State University, USA, Sandia National Laboratories, USA

10:15-10:30 Conference Closing

978-3-9504738-3-4

Controlling excitons in 2D semiconductor heterostructures and hybrid plasmonic structures

J. R. Schaibley[1]

[1]*Department of Physics, University of Arizona, Tucson, Arizona, 85721, USA*

Two dimensional (2D) semiconductors, such as $MoSe_2$ and WSe_2, host tightly bound excitons (electron-hole pairs) that interact strongly with light. These monolayer semiconductors can be stacked together to realize heterostructures that exhibit new excitonic effects. In this presentation, I will discuss the optical response of two different 2D semiconductor heterostructures. First, I will review the progress towards understanding interlayer excitons in $MoSe_2$ -WSe_2 heterobilayers. These interlayer excitons host a rich moiré physics associated with the spatially modulated interactions between layers. I will explain how two types of heterostructures, near 0° and near 60° twist angle, exhibit qualitatively different interlayer exciton behaviors as a function of temperature [1]. Interlayer excitons also possess a large permanent dipole moment that allows for their energy to be tuned with an out-of-plane electric field. By nano-patterning a gate on top of the $MoSe_2$-WSe_2 heterostructure, we are able to realize a ~30 nm diameter spatial trap for IXs, which has potential applications toward realizing deterministic single photon emitters [2]. Finally, I will discuss our work developing 2D semiconductor plasmonic modulators based on the nonlinear response of excitons on plasmonic waveguides [3].

[1] F. Mahdikhanysarvejahany *et al.* npj 2D Materials and Applications **5**, 67 (2021).

[2] D. N. Shanks *et al.* Nano Letters **21** (13), 5641-5647 (2021).

[3] M. Klein *et al.* Nat Commun **10**, 3264 (2019).

First-principles calculations of minimally twisted $MoSe_2/WSe_2$ bilayers

Madeleine Phillips[1] and C. Stephen Hellberg[1]
[1]*Center for Computational Materials Science, U.S. Naval Research Laboratory, Washington, D.C., USA*
madeleine.phillips@nrl.navy.mil

We present density functional theory (DFT) calculations of $MoSe_2/WSe_2$ bilayers twisted a small angle (~ 3°-5°) away from the commensurate 2H stacking. As the twist angle decreases, our calculations show the emergence of flat bands in both conduction and valence bands. The degeneracies of the flat bands suggest their origins in features of the 2H band structure. We also analyze the atomic relaxation of the twisted $MoSe_2/WSe_2$ bilayer away from the rigid moiré structure. While full reconstruction is not achieved at the angles we study, we begin to see the increase in area of regions of low energy stacking. We show that the states associated with the conduction and valence band flat bands are localized in different regions of local stacking. The localization of states is pronounced even though reconstruction is incomplete.

978-3-9504738-3-4

Single Photon Emitters in Monolayer WSe_2 by Nano-indentation

*Berend T. Jonker**

Naval Research Laboratory, Washington DC 20375, USA
e-mail: berry.jonker@nrl.navy.mil

Single photon emitters (SPEs), or quantum emitters, are key components in a wide range of nascent quantum-based technologies. A solid state host offers many advantages for realization of a functional system, but creation and placement of SPEs are difficult to control. We describe here a novel paradigm for encoding strain into 2D materials to create and deterministically place SPEs in arbitrary locations with nanometer-scale precision [1]. We demonstrate the direct writing of SPEs in 2D semiconductors based on a materials platform consisting of a WSe_2 monolayer on a deformable substrate consisting of 320 nm PMMA / 275 nm SiO_2 / Si using an atomic force microscope nano-indentation process (Figure 1). This *quantum calligraphy* allows deterministic placement and real time design of arbitrary patterns of SPEs for facile coupling with photonic waveguides, cavities and plasmonic structures. Because monolayer WSe_2 is a direct gap semiconductor, SPE emission at a given wavelength is often intermixed with classical light resulting from conventional excitonic recombination, reducing the purity of the quantum emission as quantified by the second order autocorrelation $g^{(2)}(t=0)$. We show that this undesirable classical emission, arising primarily from defect bound excitonic processes, can be significantly suppressed by electrostatic gating, as shown in Figure 2. Note that the defect bound excitonic feature X_{bd} is strongly suppressed by a modest gate bias of ±10V. Suppression of this classical emission allows a more accurate assessment of the quantum emission character, and results in values of $g^{(2)}$ as low as 0.07 at low temperature, as shown in Figure 3. In addition, the SPE intensity at a given wavelength can be strongly modulated by changing the polarity of the gate bias, as demonstrated by the SPE lines at ~ 1.70 eV, a feature of technological importance for practical applications.

[1] M.R. Rosenberger et al, *ACS Nano* **13**, 904 (2019). *DOI: 10.1021/acsnano.8b08730*

*Work done in collaboration with Matthew R. Rosenberger, Hsun-Jen Chuang, Madeleine Phillips, Kathleen M. McCreary, and C. Stephen Hellberg of the *Naval Research Laboratory*, Washington DC, and Chandriker Kavir Dass and Joshua R. Hendrickson of the *Air Force Research Laboratory*, Wright-Patterson AFB, OH.

† This work was supported by core programs at NRL.

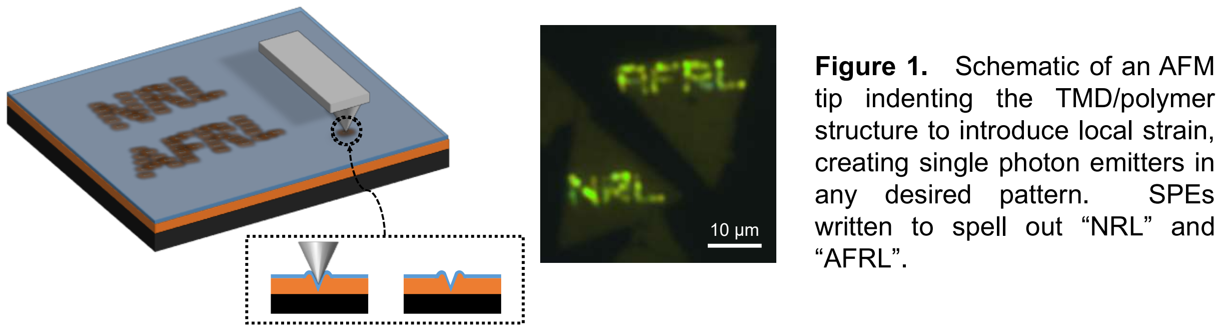

Figure 1. Schematic of an AFM tip indenting the TMD/polymer structure to introduce local strain, creating single photon emitters in any desired pattern. SPEs written to spell out “NRL” and “AFRL”.

Figure 2. Gate bias dependence of photoluminescence (T=10K) from nano-indents in monolayer WSe_2. Emission features are labeled as single photon emitters (E), defect bound exciton (X_{bd}), donor bound exciton (X_d), trion (X-) and neutral exciton (X^0). Note dramatic suppression of X_{bd} with gate bias, and modulation of SPE intensity at give wavelength with positive vs negative bias. The second order auto-correlation function $g^2(0) < 0.5$ confirms the SPE character of emission from the nano-indents.

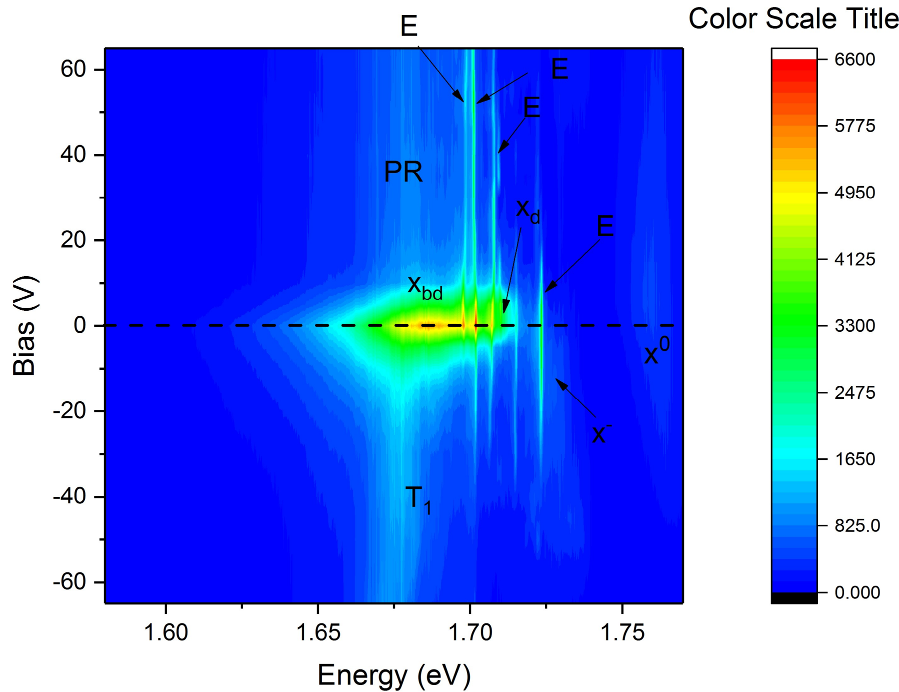

Figure 3. The second order auto-correlation function $g^2(0)$ confirms the SPE character of emission from the nano-indents, and is as low as 0.07 for a gate bias of +65V.

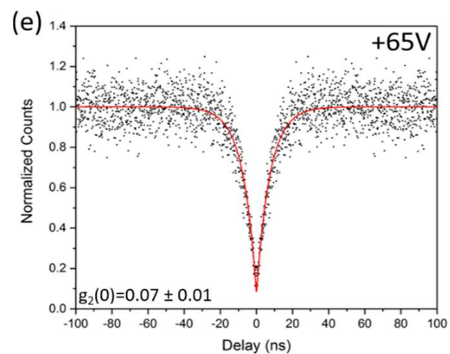

Cavity exciton-polaritons in two-dimensional semiconductors from first principles

V. Despoja[1] and D. Novko[1]
[1]*Institute of Physics, Bijenička 46, 10000 Zagreb, Croatia*
vito@phy.hr

Two-dimensional (2D) materials, such as semiconducting monolayers, thin heterostructures and films, due to the reduced Coulomb screening and the corresponding large exciton binding energies enable formation of well-defined exciton-polaritons even at room temperatures [1]. The first 2D exciton-polariton were realized in monolayer of transition metal dichalcogenide (TMD) MoS_2, where Rabi splitting between exciton and cavity photon of about 50meV was observed [2]. Further photoluminescence studies showed clear anticrossing behaviour and splitting of exciton-polariton in other 2D TMD cavity devices, e.g., in $MoSe_2$[3], WS_2[4] or in WSe_2 [5]. In this presentation I will briefly present our recently developed quantum-electrodynamical formulation of Bethe-Salpeter equation [6]. The formulation is applied to calculate the intensities of cavity exciton-polaritons in three prototypical two-dimensional single-layer semiconductors; single-layer black phosphorus (P_4), WS_2, and hBN embedded in Ag and Al cavities. Maximum Rabi splitting of 128meV is achieved in P_4 cavity, while remarkable value of about 440meV is predicted in hBN/Al device. The obtained Rabi splittings in WS_2 microcavity are in excellent agreement with the recent experiments [4]. Present methodology can aid in predicting and proposing potential setups for trapping robust 2D exciton-polariton condensates.

[1] T. Low, A. Chaves, J. D. Caldwell, A. Kumar, N. X. Fang, P. Avouris, T. F. Heinz, F. Guinea, L. Martin-Moreno and Frank Koppens, Nature Materials **16**, 182 (2017)

[2] Xiaoze Liu, Tal Galfsky, Zheng Sun, Fengnian Xia, Erh-chen Lin, Yi-Hsien Lee, Stéphane Kéna-Cohen and Vinod M. Menon, Nature Photonics **9** (1) (2014)

[3] S. Dufferwiel, S. Schwarz, F. Withers, A.A.P. Trichet, F. Li, M. Sich, O. Del Pozo-Zamudio, C. Clark 4, A. Nalitov, D.D. Solnyshkov, G. Malpuech, K.S. Novoselov, J.M. Smith, M.S. Skolnick, D.N. Krizhanovskii and A.I. Tartakovskii, Nature Communications **6**, 8579 (2015)

[4] L. C. Flatten, Z. He, D. M. Coles, A. A. P. Trichet, A. W. Powell, R. A. Taylor, J. H. Warner and J. M. Smith, Sci. Rep. **6**, 33134 (2016).

[5] S. Dufferwiel, T.P. Lyons, D.D. Solnyshkov, A.A.P. Trichet, A. Catanzaro, F. Withers, G. Malpuech, J.M. Smith, K.S. Novoselov, M.S. Skolnick, D.N. Krizhanovskii and A.I. Tartakovskii, Nature Communications **9**, 4797 (2018)

[6] D.Novko and V.Despoja, http://arxiv.org/abs/2105.05591

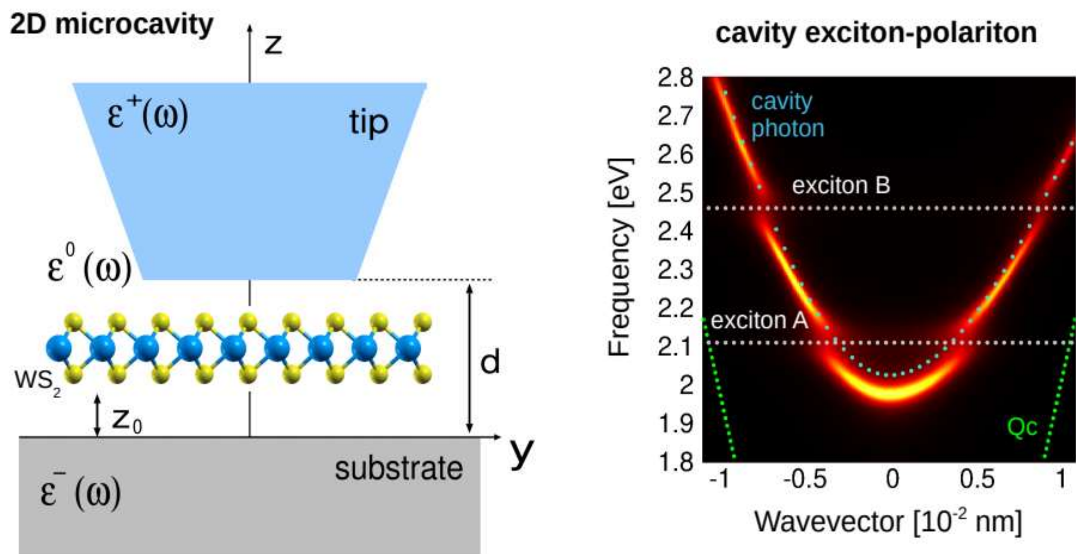

Figure 1. (left) The schematic of a micro-cavity device. The 2D crystals described by optical conductivity σ is inserted in micro-cavity which consists of substrate, dielectric media and tip described by macroscopic dielectric functions ε^-, ε^0 and ε^+,respectively. (right) The intensity of electromagnetic modes showing the hybiridisation between silver cavity mode n=1 (magenta dotted) and WS_2 A and B excitons (white dotted). Cavity thickness is d=260nm.

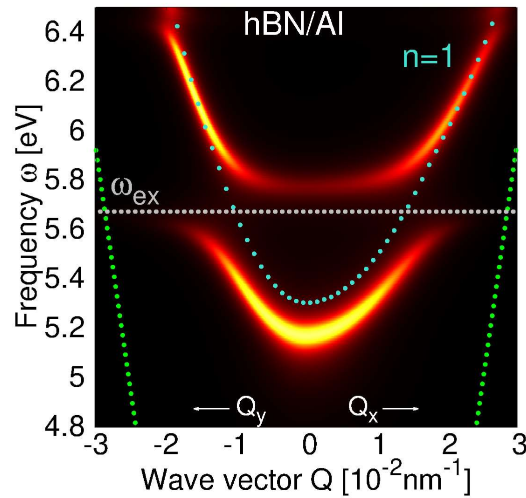

Figure 2. The intensity of electromagnetic modes in hBN/Al cavity device showing the hybridisation between cavity mode n = 1 (turquoise dotted) and hBN exciton (white dotted) . The thickness of aluminium cavity is d = 90 nm.

Watching Matter Move: Investigation of 2D half van der Waals heterostructures materials

F. Niefind[1,2], C. Dong[3], R. A. Maniyara,[3] J. A. Robinson[3] and S. Pookpanratana[1*]

[1] Nanoscale Device Characterization Division, National Institute of Standards and Technology, Gaithersburg, MD 20899, USA

[2] Department of Chemistry & Biochemistry, University of Maryland, College Park, MD 20742, USA

[3] Department of Materials Science & Engineering, Pennsylvania State University, University Park, PA 16802, USA.

sujitra@nist.gov

Atomically-thin, 2D layered systems provide a quantum materials landscape which enables tailoring electron interactions with heterointerfaces. Emergent quantum properties have been observed in these 2D heterosystems such as superconductivity in bilayer graphene[1] and inducing magnetism in WSe_2 when interfaced with CrI_3.[2] Recently, 2D metals have been confined between graphene and SiC, where 2D gallium displays superconductivity.[3] The confinement heteroepitaxy (CHet)[3] has been demonstrated in metals and GaN, and is still much unknown on how these transformations occur.

Here, we use photoemission electron microscopy (PEEM) to observe the silver (Ag) intercalation process between graphene and SiC with *in-situ* annealing. PEEM is a surface-sensitive, full-field imaging technique that can achieve nanometer-scale spatial resolution with topographic and electronic contrast. We find that after the *ex-situ* CHet process is performed, we can still drive a small portion of the Ag atoms above and below the graphene surface at moderate temperatures (300 °C) and observe the intercalation directly in real time (~1 s resolution). The process eventually ceases, where additional heating will not drive the diffusion process. Additional experiments are underway where we anticipate correlating microstructure (and its local variation) to the electronic properties of these nanoscale 2D systems.

In-situ PEEM imaging can be extended to address other technological issues such as measuring the efficacy of 2D layered materials as copper interconnect diffusion barriers. 2D materials, graphene and molybdenum disulfide (MoS_2), have been proposed and tested as possible diffusion barrier alternatives due to their inherent atomically thin layer thickness.

1. Y. Cao et al., Nature 556 (7699), 43-50 (2018).
2. D. Zhong et al., Science Advances 3 (5), e1603113 (2017).
3. N. Briggs et al., Nature Materials 19, 637-643 (2020).

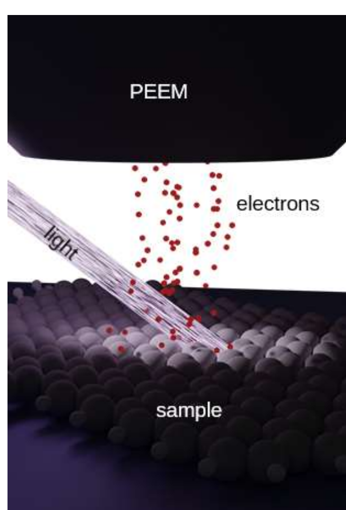

Fig. 1. Schematic of the full-field PEEM imaging which uses photons to eject photoelectrons (not to scale).

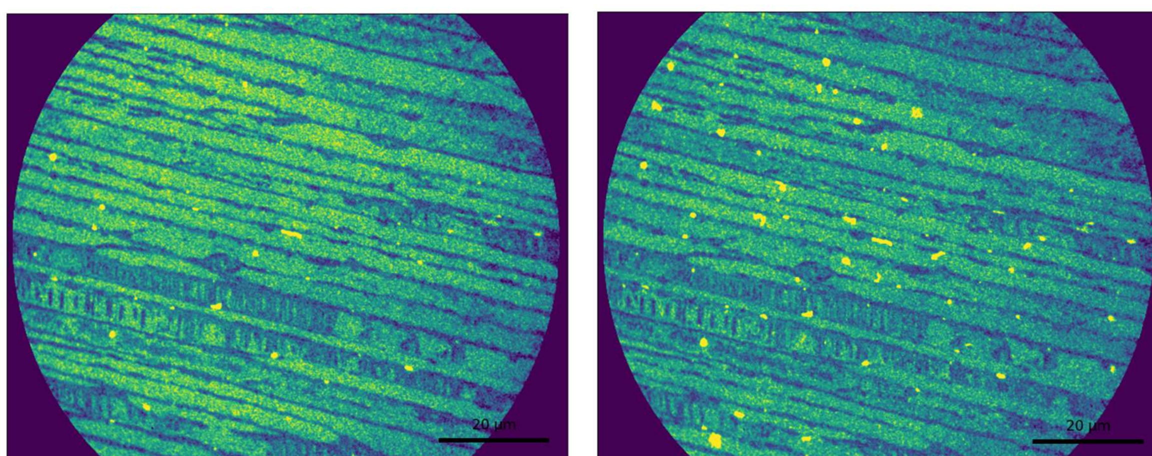

Fig. 2. Images of the intercalated 2D Ag epitaxial graphene surface where Ag (in yellow) before (left) and after (right) heating at 300°C for ~30 minutes. Scale bar in both images is 20 µm.

Monolayer borophene on Ir(111): Segregation-enhanced epitaxy and electrochemical transfer

M. Petrović[1,2], K. M. Omambac[2], B. Radatović[1], S. Kamal[1], V. Jadriško[1], P. Dreher[2], D. Janoschka[2], C. Brand[2], M. A. Kriegel[2], N. Hartmann[3,4], N. Vujičić[1], M. Kralj[1], F. J. Meyer zu Heringdorf[5,3], and M. Horn-von Hoegen[2]

[1]*Center of Excellence for Advanced Materials and Sensing Devices, Institute of Physics, 10000 Zagreb, Croatia*

[2]*Faculty of Physics, University of Duisburg-Essen, 47057 Duisburg, Germany*

[3]*Interdisciplinary Center for Analytics on the Nanoscale (ICAN), 47057 Duisburg, Germany*

[4]*Faculty of Chemistry, University of Duisburg-Essen, 45141 Essen, Germany*

[5]*Faculty of Physics and Center for Nanointegration Duisburg-Essen (CENIDE), University of Duisburg-Essen, 47057 Duisburg, Germany*

mpetrovic@ifs.hr

Well-established procedures for large-scale fabrication and utilization of many 2D materials (2DMs) are still missing, especially of 2DMs without naturally occurring layered bulk counterparts. One such material is borophene which is known to have metallic character [1] and which holds potential to serve as a conductive layer in future flexible electronics.
Here we tackle scalable synthesis of 2D boron by performing segregation-enhanced epitaxy of borophene on Ir(111) and its transfer to Si wafer. Our growth method utilizes borazine as a source of B atoms, which are dissolved in subsurface layers of Ir at high synthesis temperatures. During cooldown, B atoms segregate back to the surface and self-assemble into a full borophene monolayer (Fig. 1) [2]. The process of B atom dissolution and segregation is tracked in real time by low-energy electron microscope (LEEM) (Fig. 2), and is complemented by depth profiling of B in Ir obtained from time-of-flight secondary ion mass spectrometry (TOF-SIMS) (Fig. 3). In the transfer process, which involves temporary mechanical support by a PMMA layer, millimeter-sized borophene monolayer is electrochemically delaminated from the Ir substrate [3], and placed onto a Si wafer. Atomic force microscopy (AFM) (Fig. 4) and Raman spectroscopy have been utilized to characterize samples before and after the transfer, revealing transfer-induced modifications and defects in the material. Our results demonstrate a new route for fabrication of extended 2D boron layers, and bring borophene closer to integration into nanoscale (opto)electronic devices.

[1] B. Feng *et al.*, Phys. Rev. B **94**, 041408 (2016).

[2] K. M. Omambac *et al.*, ACS Nano **14**, 7421 (2021).

[3] L. Koefoed *et al.*, J. Phys. D: Appl. Phys. **48**, 115306 (2015).

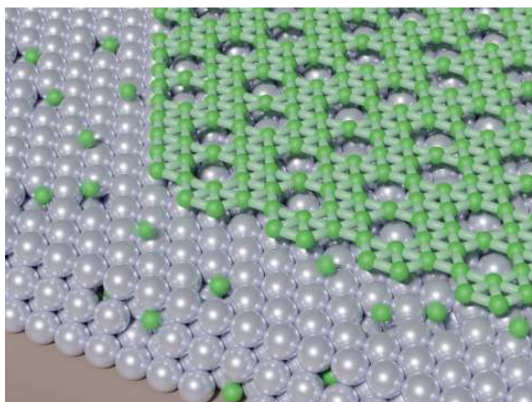

Fig.1: Schematic representation of B atoms (green spheres) segregating to Ir(111) surface during sample cooling, and their self-assembly into a borophene sheet. The process is self-limited to a single layer.

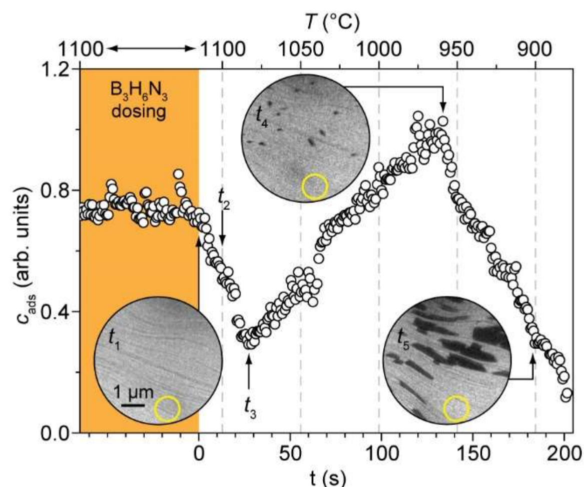

Fig.2: Concentration of adsorbates on the Ir(111) surface, calculated from local LEEM reflectivity (area encircled in yellow), as a function of sample temperature and cooling time. B atom dissolution and segregation is correlated with the emergence of borophene islands (black patches in the insets).

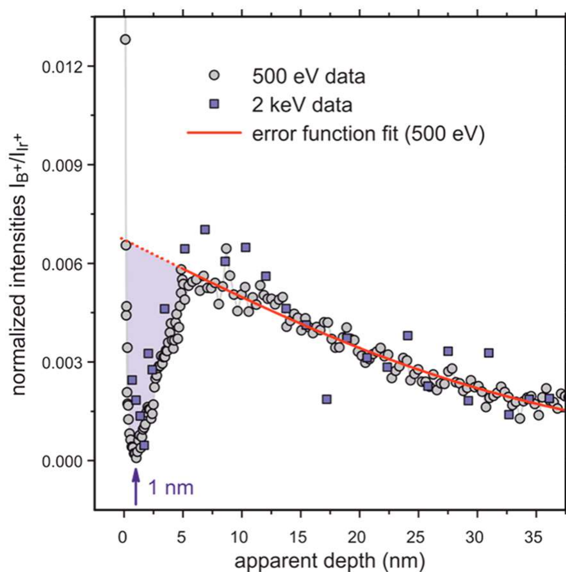

Fig.3: TOF-SIMS depth profile recorded on borophene-covered Ir(111), showing normalized $^{11}B^{+}$ intensity as a function of depth. Dip with a minimum at 1 nm corresponds to the B atoms which have segregated to the surface to form a borophene layer.

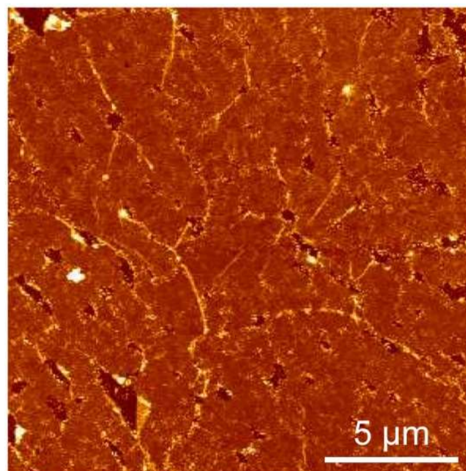

Fig.4: AFM topography of borophene transferred to an oxidized Si wafer by using the electrochemical transfer method.

Spintronic studies of ferrimagnetic and antiferromagnetic Weyl semimetals

Eric E. Fullerton[1]

[1]*Center for Memory and Recording Research, University of California San Diego, La Jolla CA 92093-0401 USA*

Topology has emerged in many areas of magnetism that included both chiral spin structures and emergent electronic structures such as Weyl semimetals [1]. The further lowering of the symmetry of the crystal via strain or magnetic order can provide additional functionality. I will discuss recent studies of thin films of candidate Weyl semimetals with ferrimagnetic order, $CrPt_3$ or antiferromagnetic order, $FePt_3$ and FeRh [2]. We have grown epitaxial chemically-ordered films and studied the spin structure, magneto-transport properties, and spin-to-charge conversion that is a source for spin torques. For $CrPt_3$ we obtain large anomalous Hall conductivity of 2000 S/cm and large negative magneto-resistance consistent with Weyl semimetal properties. For antiferromagnetic $FePt_3$ we obtain large magnetoresistance values and track this behavior to the tunable Néel vector orientation. Finally, I discuss recent measurement of large exotic spin torques in the antiferromagnetic phase of FeRh [3]. We observe extremely large, strongly temperature-dependent exotic spin torques with a geometry that is tied to the magnetic ordering direction. Having magnetic materials that generate large, tunable spin-orbit torques may be used in conventional computing to re-orient or switch nanomagnets for non-volatile memory schemes, or in novel computing implementations to drive spin dynamics in more complex magnetic systems. This work is supported by US Department of Energy under Grant No. DE-SC0019273

[1] M. J. Gilbert, Comm. Phys. **4**, 1-12 (2021).

[2] A. Markou *et al.*, Comm. Phys. **4**, 104 (2021).

[3] J. Gibbons *et al.*, arXiv:2109.11108 (2021).

Spin and Charge Drift-Diffusion Approach to Torque Computation in Spintronic Devices

Simone Fiorentini[1], Roberto Lacerda de Orio[2], Siegfried Selberherr[2], Johannes Ender[1], Wolfgang Goes[3], and Viktor Sverdlov[1]

[1] Christian Doppler Laboratory for Nonvolatile Magnetoresistive Memory and Logic at the

[2] Institute for Microelectronics, TU Wien, Gußhausstraße 27-29/E360, 1040 Vienna, Austria

[3] Silvaco Europe Ltd., Cambridge, United Kingdom

e-mail: fiorentini@iue.tuwien.ac.at

Various approaches have been proposed to describe the interplay between the magnetization and the charge and spin currents. Zhang and Li [1] introduced a model to describe torques acting on the magnetization in the presence of magnetization gradients, while the work from Slonczewski allows to compute the torques acting in spin-valves and magnetic tunnel junctions [2, 3]. The spin and charge drift-diffusion formalism [4] gives a way to bridge the gap between the two and compute both contributions using the same set of equations.

The original Zhang and Li equation takes into account the effects of the spin exchange length λ_J and the spin-flip length λ_{sf}, but does not include the spin dephasing length λ_φ [5, 6]. When this contribution is considered, the equation for the torque [1] is modified to

$$\mathbf{T}_{ZL} = -\frac{\mu_B}{e}\frac{\beta}{(1+(\epsilon+\epsilon')^2)}\Big(\big(1+\epsilon'(\epsilon+\epsilon')\big)\mathbf{m}\times[\mathbf{m}\times(\mathbf{J_C}\cdot\nabla)\mathbf{m}] - \epsilon\mathbf{m}\times(\mathbf{J_C}\cdot\nabla)\mathbf{m}\Big), \quad (1)$$

where $\epsilon = \lambda_J^2/\lambda_{sf}^2$ and $\epsilon' = \lambda_J^2/\lambda_\varphi^2$. In Fig.1 the comparison of the torque computed from (1) with the torque computed numerically from the spin drift-diffusion formalism [5,6] is reported, with $\lambda_{sf} = 10$ nm, $\lambda_J = 1$nm and $\lambda_\varphi = 5$ nm, for the magnetization texture in Fig.2. Here, the orientation of the magnetization is rotated from the z direction to the -x direction over a distance of 100 nm. In Fig.3, the same comparison is shown with the magnetization orientation changing within 3 nm. A clear discrepancy is observed. When the magnetization texture is shorter than the spin accumulation decay length, the assumption needed to derive the Zhang-Li model is violated. Therefore, the torque (1) deviates from the one computed with the complete spin drift-diffusion model. However, for shorter values of the spin dephasing length the agreement is recovered, as shown in Fig.4 for $\lambda_\varphi = 0.4$nm, because the decay of the transverse spin accumulation components is governed by the short value of λ_φ, and the validity of the assumption of the Zhang-Li model is restored.

When dealing with a spin-valve, the free layer is subject to a torque due to the current polarized by the reference layer. In this case, the presence of a short dephasing length allows for the torque computed from the spin drift-diffusion approach to rapidly decay, as expected from Slonczewski's work [2,3]. This rapid decay is showcased in Fig.5 for a spin current coming

from the left interface and $\lambda_{\varphi} = 0.4$ nm. Moreover, the spin drift-diffusion equations can be extended to include ballistic corrections to the spin-current formulation [7], governed by the electron mean free path λ. Fig.6 shows the torque computed using $\lambda_J = 1$ nm, $\lambda_{\varphi} = 4.3$nm, and $\lambda = 5.8$ nm, which qualitatively agrees with the ballistic torque derived in [8].

In conclusion, the reported results underline the potential of the spin and charge drift-diffusion formalism to compute spin-transfer torques acting on the magnetization in modern spintronic devices.

[1] S. Zhang, Z. Li., Phys. Rev. Lett. **93**, 127204 (2004).

[2] J.C. Slonczewski, J. Mag. Mag. Mat. **159**, L1 (1996).

[3] J.C. Slonczewski, Phys. Rev. B **71**, 024411 (2005).

[4] C. Abert *et al.*, Sci. Rep. **5**, 14855 (2015).

[5] S. Lepadatu, Sci. Rep. **7**, 12937 (2017).

[6] S. Fiorentini *et al.*, Sol. St. El. **186**, 108103 (2021).

[7] P. Graczyk *et al.*, Sci. Rep. **11**, 15692 (2021).

[8] M. Chshiev *et al*, Phys. Rev. B **92**, 104422 (2015).

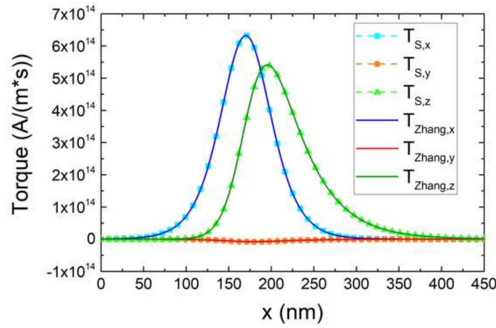

*Fig.1: Comparison of the torque computed from equation (1) and the one computed from the spin accumulation (**T**$_S$) in the case of long magnetization texture.*

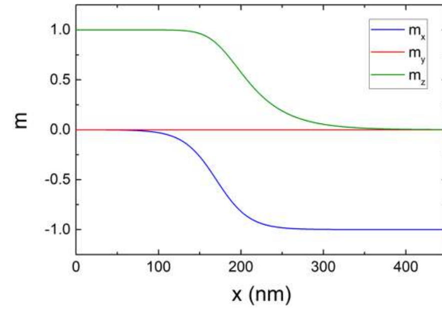

Fig.2: Magnetization texture employed for the Zhang-Li torque computation. The magnetization rotates from the z direction to the -x direction over a distance of 100 nm.

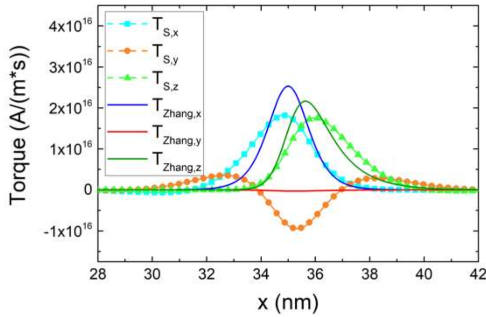

Fig.3: For magnetization textures shorter than λ_{sf}, the Zhang-Li assumption of vanishing spin gradients is not valid.

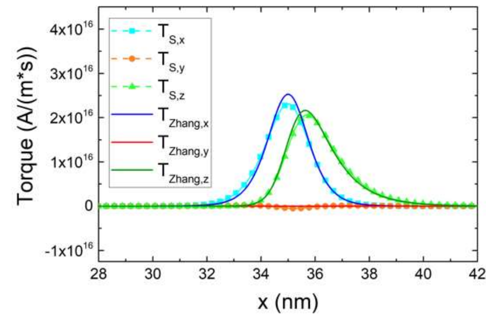

Fig.4: Using a short dephasing length recovers the agreement between the Zhang-Li and the spin accumulation approaches.

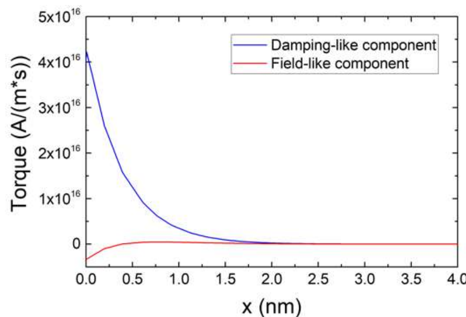

Fig.5: With a short dephasing length, the torque acting in the free layer of a spin valve is quickly absorbed in the span of 1-2 nm.

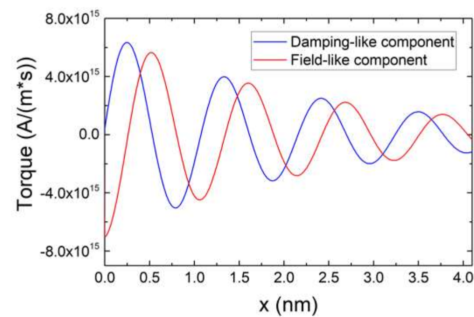

Fig.6: Additional terms in the spin current equation allow to reproduce the ballistic behavior of the torques.

Spin-orbit torque facilitated switching of topological insulator/ferromagnet heterostructures

M. A. Noyan[1], O. M. J. van ‘t Erve[1], C. H. Li[1], X. Zhang[4], J. Moon[2], M. Lohmann[3], E. Cobas[1], B. T. Jonker[1]

[1]*Materials Science and Technology Division, Naval Research Laboratory, Washington D.C.*

[2]*NRC Postdoctoral Fellow at NRL*

[3]*ASEE Postdoctoral Fellow at NRL*

[4]*Nova Research Associate at NRL*

mehmet.noyan@nrl.navy.mil

As worldwide demand for computing grows exponentially and processors become increasingly powerful, the need for memory technologies that are energy efficient, non-volatile and capable of ultrafast read/write operations is urgent. One promising technique is the use of materials with spin-orbit coupling to control magnetic layers using spin-orbit torque. In this talk I will discuss our group’s ongoing work to leverage spin-momentum locking in topological insulators to manipulate magnets, as measured using Kerr Rotation and using both pulsed and DC current modalities. I will focus on recent results in which we have switched the in-plane moment of a NiFe layer in a Bi_2Se_3/NiFe structure in which the Bi_2Se_3 has been specially engineered to be bulk insulating, maximizing the spin-momentum locking in the charge current. We find that we are able to switch the NiFe layer using a current density in the Bi_2Se_3 more than an order of magnitude lower than required in more commonly used heavy metals. I will contextualize these results with transport and spin-torque ferromagnetic resonance measurements and also touch on partial switching of Bi_2Se_3/Fe_2GeTe_2 structures, before closing with some discussion of future work.

978-3-9504738-3-4

Magnetic diode type effect in artificial honeycomb lattice due to magnetic charge correlation

Deepak K. Singh[1], Valeria Lauter[2], George Yumnam[1], Yiyao Chen[1] and Jiasen Guo[1]
[1]*Department of Physics and Astronomy, University of Missouri, Columbia, MO, USA*
[2]*Oak Ridge National Laboratory, Oak Ridge, TN, USA*
singhdk@missouri.edu

Magnetic or Spin diode is important prerequisite to the practical implementation of spin electronics. Yet, a functioning magnetic diode at room temperature is still illusive. The emergent phenomena of magnetic charge physics, realized in artificial spin ice materials, provides a new testing principle in this quest. Artificial magnetic honeycomb lattice depicts natural tendency to generate magnetic charges of low, ±Q, and high, ±3Q, multiplicities on the vertices under the dumbbell prescription of magnetic moment (Q is directly related to magnetic moment M along honeycomb element via Q = M/L, L being the length).[1] Magnetic charges relax by releasing net charge defect of |2Q| magnitude between the neighboring vertices. Neutron spin echo study has shown that the charge defects are highly dynamic with typical relaxation rate of ~ 50 ps.[2] Magnetic charge relaxation causes indirect interaction between fluctuating magnetic field, due to the charge defect dynamics, and electric charge carrier spin **s** (see inset in Fig. 1b). Consequently, electrical conduction in permalloy ($Ni_{0.81}Fe_{0.19}$) honeycomb lattice is propelled by more than an order of magnitude.[2] In this presentation, we describe the occurrence of diode-type phenomena due to magnetic charge mediated conduction in artificial honeycomb geometry, made of concave shape single domain permalloy element (~ 12 nm in length and 8 nm in thickness). We find that honeycomb lattice defies symmetry by populating vertices with low and high multiplicity magnetic charges, causing asymmetric magnetization, in applied current of opposite polarity, see Fig 2.[3] High multiplicity units create highly resistive network, thereby inhibiting magnetic charge dynamics propelled electrical conduction.[4] However, practical realization of this effect requires modest demagnetization factor in constituting element. Concave structure fulfills the condition. Subsequently, magnetic diode behavior with small forward threshold voltage emerges across broad thermal range of T = 40K - 300K. Finally, we will discuss the possibility of a new vista due to magnetic charge correlation for spintronic research.

Research at MU is supported by the U.S. Department of Energy, Office of Basic Energy Sciences under Grant No. DE-SC0014461. This research used resources at the Spallation Neutron Source, a DOE Office of Science User Facility operated by the Oak Ridge National Laboratory.

[1] G. Yumnam, Y. Chen, J. Guo, J. Keum, V. Lauter and D. K. Singh, **“**Quantum disordered state of magnetic charges in nanoengineered honeycomb lattice”, *Advanced Science* **8**, 2004103 (2021).
[2] Y. Chen, G. Yumnam, J. Guo, L. Stingciau, P. Zolnierczuk, V. Lauter and D. K. Singh, “Magnetic charge's relaxation propelled electricity in two-dimensional magnetic honeycomb lattice, *iScience* **24**, 102206 (2021)
[3] G. Yumnam, J. Guo, Y. Chen, A. Dahal, P. Ghosh, Q. Cunningham, V. Lauter and D. K. Singh, “Magnetic charge and geometry confluence for ultra-low forward voltage diode in artificial honeycomb lattice”, submitted 2021
[4] Y. Chen, B. Summers, A. Dahal, V. Lauter, G. Vignale and D. K. Singh, “Field and current control of the electrical conductivity of an artificial two-dimensional honeycomb lattice”, *Advanced Materials* **31,** 1808298 (2019).

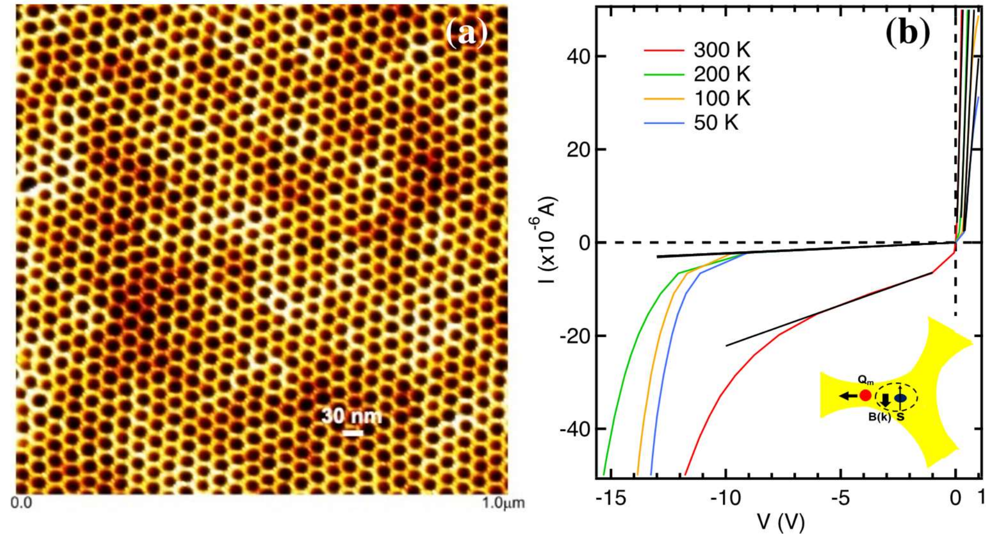

*Figure 1: (a) AFM image of artificial honeycomb lattice, made of ultra-small elements (~ 12 nm length, 8 nm thickness). (b) Electrical measurements reveal diode-type asymmetric conduction at low forward threshold voltage across broad thermal range. As depicted in the inset, interaction between fluctuating magnetic field **B(k)** (arising due to the longitudinal relaxation of magnetic charge Q_m, along honeycomb element at ~ 50 ps) and conduction electron's spin **s** causes a net faster drift to charge carriers. Consequently, electrical conductivity is propelled by more than an order of magnitude. Magnetic field application, larger than the coercivity of the sample, suppresses the diode-type behavior due to magnetic charge freezing along field direction.*

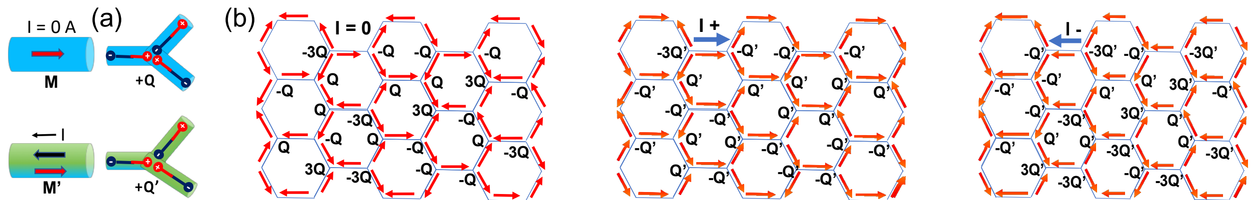

Figure 2: (a) Current application causes fractional transformation to net magnetic charge magnitude. (b-d) In unbiased state, low |Q| and high |3Q| multiplicity charges are randomly distributed across honeycomb vertices. In forward biased state (I+), most vertices are occupied by |Q| charges (fig. c). In the reverse biased state (I-), most vertices are occupied by high multiplicity |3Q| charges. |3Q| charges act as high energy scattering centers for charge carriers. Model calculations show that such charge configuration inhibits conduction.

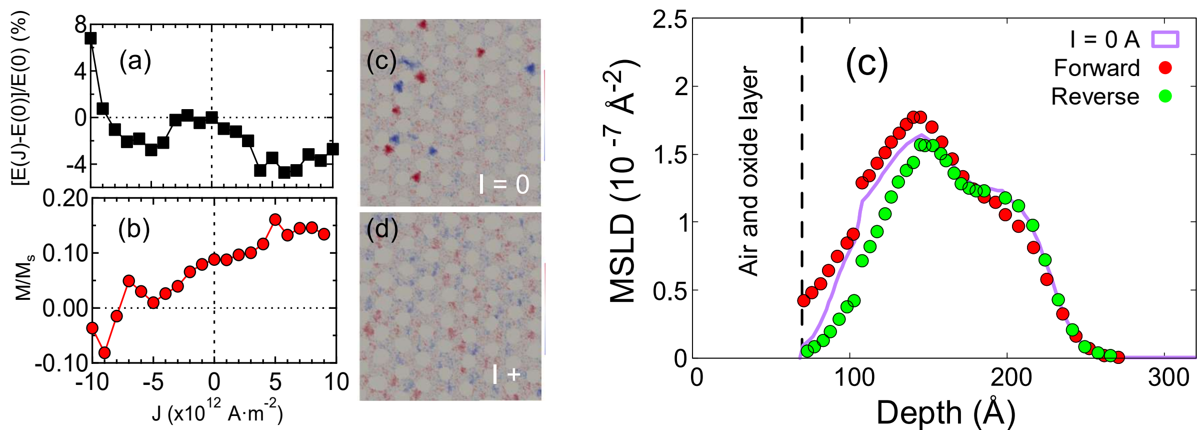

Figure 3. (a-b) Asymmetric magnetization and energy manifested by honeycomb lattice in current application, as revealed by micromagnetic simulations. (c-d) Honeycomb vertices occupied by high (dark red and blue spots) and low multiplicity charge in reverse and forward biased states, respectively. (e) Higher magnetization in forward biased state is confirmed by magnetic and neutron reflectometry measurements. The plot of magnetic scattering length density vs thickness shows higher magnetization in forward biased state.

GeSn alloys on Si (100): A versatile platform for electronic and optical devices

Detlev Grützmacher[1,2], Dan M. Buca[1], Qing-Tai Zhao[11]
[1]*Institute for Semiconductor Nanoelectronics , Peter Grünberg Institute – 9,*
Forschungszentrum Jülich, 52425 Jülich, Germany
[2]*JARA-Institute for Green-IT, Peter Grünberg Institute 10, RWTH Aachen University and*
Forschungszentrum Jülich, Germany
d.gruetzmacher@fz-juelich.de

GeSn alloys are considered as the most promising material for Silicon photonics entirely basing on group IV elements. Alloys with Sn contents above 8% exhibit a fundamental direct band-gap, similar to conventional III-V semiconductors and thus can be employed for Laser [1]. Moreover, the effective masses of electrons (m_e*) and holes (m_h*) can be smaller than those for InSb and Ge, respectively. This unique properties make GeSn an extraordinary candidate for opto-electronic integration.

Here, we report on recent achievements on optical and electronical devices based on GeSn. A µ-disc laser equipped with a SiN_x stressor layer is introduced. A GeSn alloy with 5% Sn, thus an indirect band gap, is transformed via tensile strain engineering into a direct band-gap semiconductor. Remarkably, for continuous wave (cw) as well as pulsed excitation lasing is detected at a wavelength of 2.5µm under optical pumping at thresholds as low as 0.8 kW/cm^2 for ns-pulsed, and 1.1kW/cm^2 for cw excitation [2]. These thresholds are more than two orders of magnitude lower than those previously reported for bulk GeSn lasers.

Using Si/Ge/GeSn n-i-p-i-n structures back to back Ge and GeSn photodetectors have been realized [3]. This two-terminal dual-band detector provides a bias-switchable spectral response in two distinct IR bands. The photoresponse can be switched by inverting the bias polarity between the near (Ge) and the short-wave (GeSn) IR bands, with specific detectivities of 1.9 x 10^{10} and 4.0 x 10^9 cm Hz$^{1/2}$/W, respectively.

Finally, high-performance vertical gate-all-around NW p-type FETs (p-FETs) are presented. The device concept is based on quasi-one-dimensional semiconductor NWs fabricated with a topdown approach [4]. The GeSn/Ge NW p-FETs exhibits a subthreshold slope of 72 mV/dec, a high I_{ON}/I_{OFF} ratio of 3x10^6 and small contact resistances. A 32% drive current enhancement is obtained compared to the vertical Ge homojunction NW control devices.

[1] S. Wirths et al., Nature Photonics 4, 075102 (2015).
[2] A. Elbaz, D. Buca et.al. Nature Photonics 14, 375 (2020)
[3] E.T. Simola et.al. ACS Photonics 8, 2166, (2021)
[4] M. Liu et.al. ACS Applied Nano Materials 4, 94 (2021)

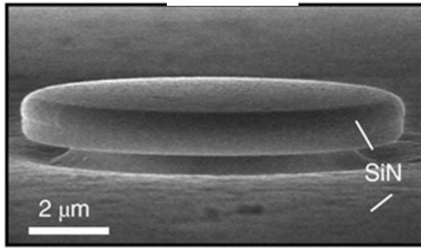

SEM image of a SiNx encapsulated GeSn μ-disc laser [2]

Right: ***a****, Emission spectra measured at 25 K for 9 μm-diameter disk, various c.w. excitation levels.* ***b****, Lasing mode peak intensity above threshold in logarithmic scale, illustrating high intensity compared to the spontaneous background emission. Inset: The intensity profile of the lasing mode, identified as $TM_{20,1}$.* ***c****, Detailed behaviour at threshold: L–L curve of the peak intensity of the 485 meV laser mode (black) and its linewidth (red).* [2]

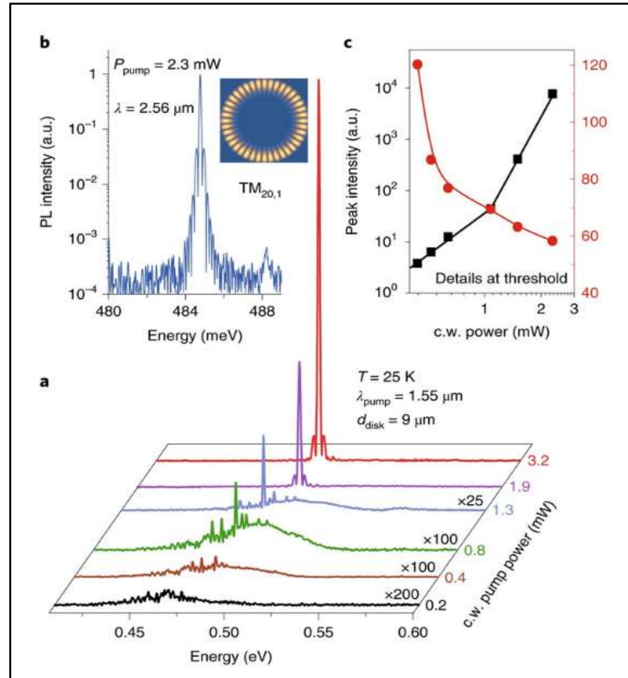

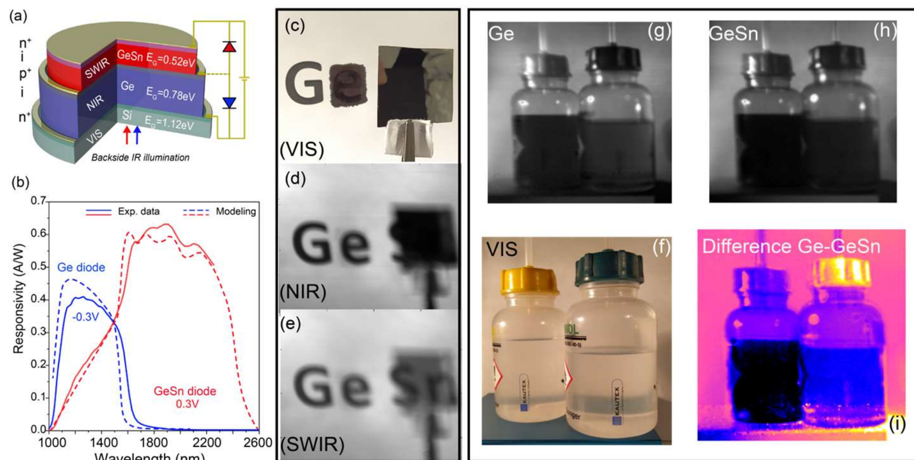

(a) Sketch of the dual band Photodetector (b) Responsitvity of Ge (NIR) and GeSn (SWIR) photodetector. Panel(c-e): same scene viewed by (c) a VIS camera; dual-band GeSn/Ge device under applied bias (d) of −0.3 V, Ge/Si diode and (e) of +0.3 V, GeSn/Ge diode. Panel (f-i)Comparison of imaging scene with VIS camera, Ge and GeSn detector with:differential imaging using the GeSn/Ge/Si dual-band device of two solvents. for the images taken with Ge (B2) and GeSn (B3) detectors.[3]

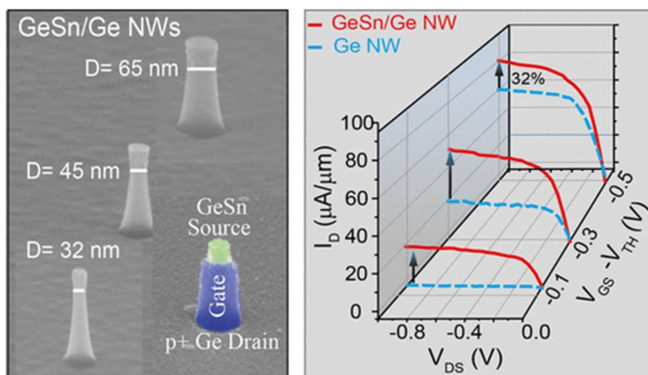

Left: Assembled SEM images of GeSn/Ge NWs of different diameters and a height of 220 nm [4]

Right: Comparison of the I_D–V_{DS} output characteristics of a GeSn/Ge heterostructure p-FET with that of a reference Ge homojunction device, for a NW diameter of 65 nm in both cases. The GeSn/Ge p-FET shows much larger currents than its Ge counterpart for any gate-driving voltage V_{GS}–V_{TH}. [4]

Real-Time Quantum Dynamics of Long-Range Electronic Excitation Transfer in Plasmonic Nanoantennas

Bryan M. Wong
Materials Science & Engineering Program, Department of Physics & Astronomy
University of California, Riverside
bryan.wong@ucr.edu

Using large-scale, real-time, quantum dynamics calculations, we present a detailed analysis of electronic excitation transfer (EET) mechanisms in a multiparticle plasmonic nanoantenna system. Our simulations provide a quantum-mechanical description (at an electronic/atomistic level of detail) for characterizing and analyzing these systems, without recourse to classical approximations. We also demonstrate highly long-range electronic couplings in these complex systems and find that the range of these couplings is more than twice the conventional cutoff limit considered by Förster resonance energy transfer (FRET)-based approaches. Furthermore, we attribute these unusually long-ranged electronic couplings to the coherent oscillations of conduction electrons in plasmonic nanoparticles. This long-range nature of plasmonic interactions has important ramifications for EET; in particular, we show that the commonly used "nearest-neighbor" FRET model is inadequate for accurately characterizing EET even in simple plasmonic antenna systems. These findings provide a real-time, quantum-mechanical perspective for understanding EET mechanisms and provide guidance in enhancing plasmonic properties in artificial light-harvesting systems.

978-3-9504738-3-4

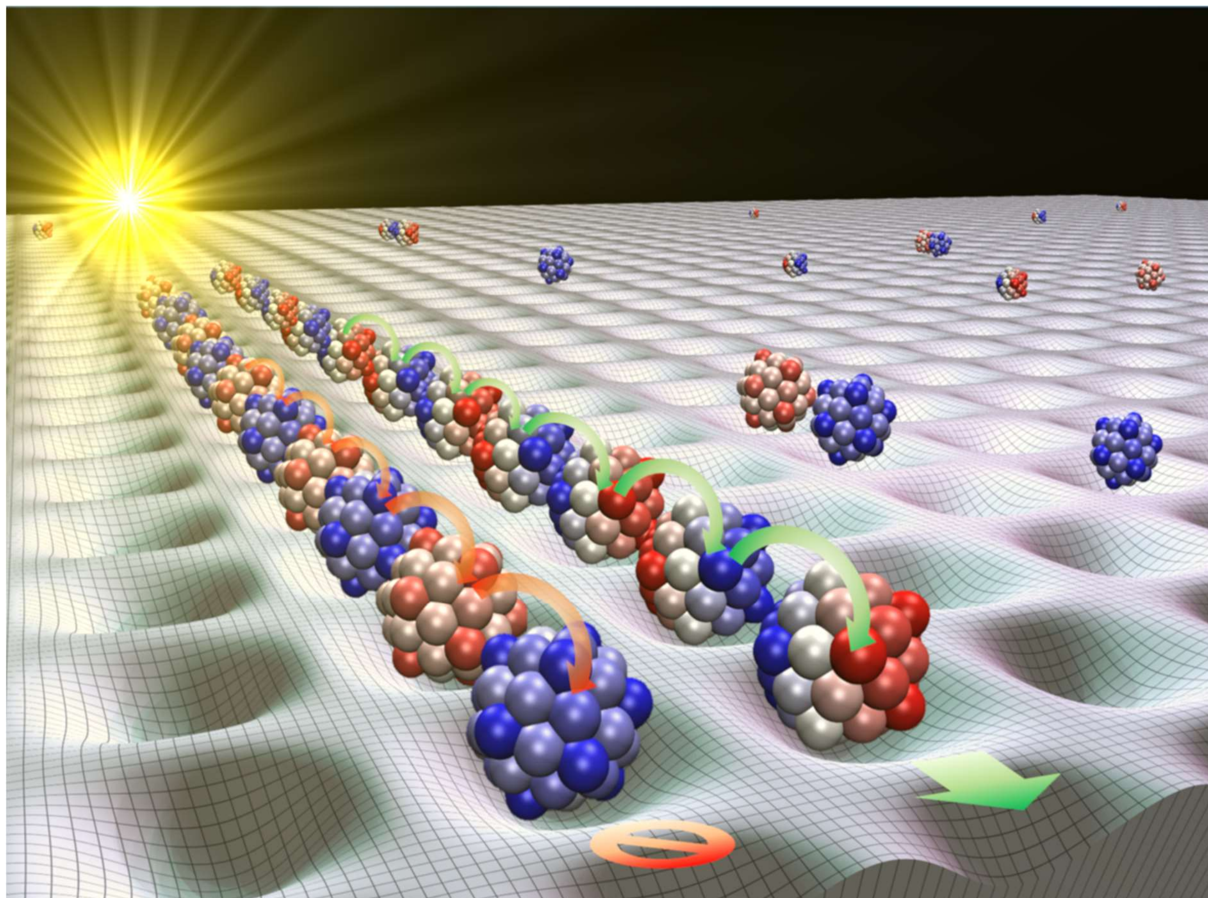

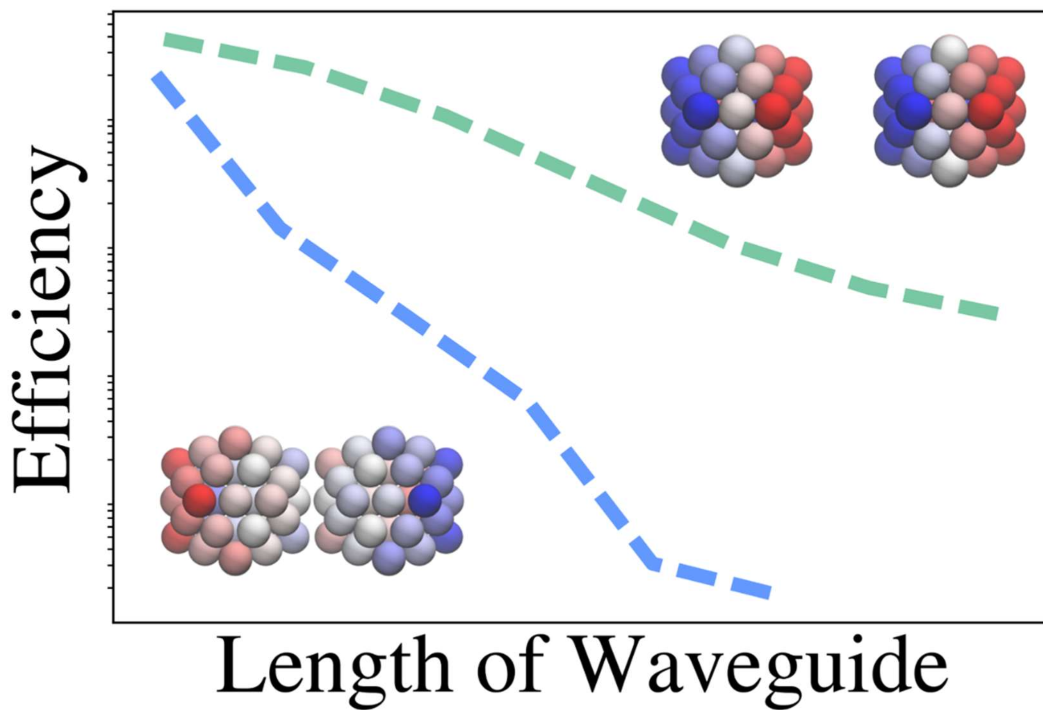
Efficiency
Length of Waveguide

Thermoelectric Nanoantennas for Mid- and Far-Infrared Detection

G. P. Szakmany[1], G. H. Bernstein[1], A. O. Orlov[1], E. C. Kinzel[2], and W. Porod[1]
[1]Department of Electrical Engineering and [2]Department of Aerospace and Mechanical Engineering, University of Notre Dame, Notre Dame, IN 46556, USA
gszakman@nd.edu

This work investigates a new type of infrared sensor that exploits the wave nature of infrared (IR) radiation. At IR wavelengths, radiation detection is complicated by the lower energy of photons that requires semiconductors with much narrower bandgaps than visible detectors. Bolometric solutions require biasing, which introduces additional noise, and pyroelectric detectors require modulation that reduces the time to response and consumes power.

Thermoelectrically coupled nanoantennas (TECNAs) resonantly absorb incident IR radiation by an antenna, and radiation-induced antenna currents heat the hot junction of a nanothermocouple that produces and open-circuit voltage proportional to the intensity of the incident IR radiation [1]. The nanoantennas provide spectral, directional, and polarization sensitivity; and the extremely low thermal mass of the device permits μs response time [2, 3].

Here, we show data for dipole and spiral antennas (Fig. 1). TECNAs are fabricated above a quasi-spherical cavity etched into the Si substrate (Figs. 2-3) that provides thermal insulation and focuses the radiation to the antenna, which increases the gain of the antenna [4]. We present antenna arrays having more than 3000 TECNAs connected in series and parallel combinations (Fig. 4). The antennas are designed to operate at 5.5 μm or at 10.6 μm.

Figure 5 shows the polarization dependent response of a 5.5 μm dipole antenna array excited by a CO laser (λ=5.5 μm). The laser polarization was rotated by a $\lambda/2$ wave plate and the TECNA response follows the cosine-square dependence. We also demonstrate TECNAs with spiral antennas designed to detect circularly polarized IR radiation. Figure 6 shows the simulated spectral response and the measured extinction ratio of spiral antennas. The devices were excited by a CO_2 laser (λ=10.6 μm), and a $\lambda/4$ wave plate was used to create left- and right-handed circularly polarized (LHCP and RHCP) IR radiation. An extinction ratio of 5 was measured, which is in good agreement with simulation. In our talk, we will discuss TECNA operation and energy absorption in the antenna structures at different polarizations.

[1]G. P. Szakmany, P. M. Krenz, A. O. Orlov, G. H. Bernstein, and W. Porod, IEEE Trans. Nanotechnol. **12**, 163 (2013).

[2]G. P. Szakmany, G. H. Bernstein, E. C. Kinzel, A. O. Orlov, and W. Porod, Sci. Rep. **10**, 13429 (2020).

[3]G. P. Szakmany, A. O. Orlov, G. H. Bernstein, and W. Porod, IEEE Transactions on Nanotechnology **15**, 567 (2016).

[4]G. P. Szakmany, A. O. Orlov, G. H. Bernstein, and W. Porod, Sci. Rep. **9**, 9606 (2019).

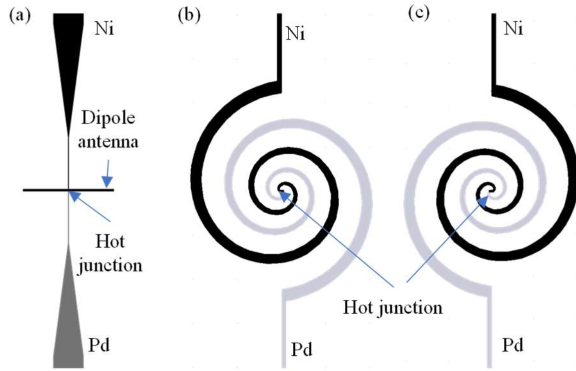

Fig. 1: Schematics of TECNA with various antennas. (a)Dipole antenna provides linear polarization sensitivity, and its length determines the spectral response. The log-spiral antenna selective to (b)left- and (c)right hand circularly polarized light.

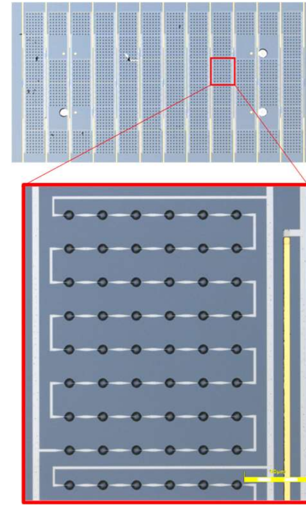

Fig. 4: Optical micrograph of an antenna array having more than 3,000 TECNAs. The inset shows a section of the array.

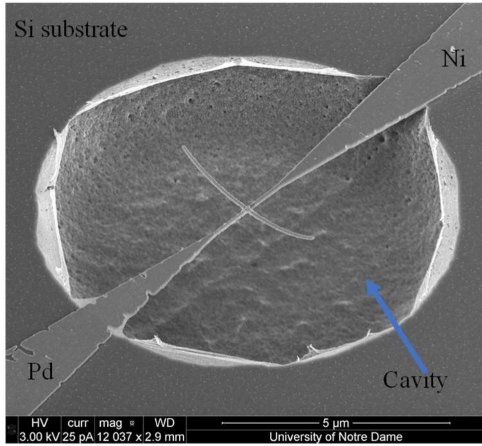

Fig. 2: SEM image of a TECNA with a dipole antenna above a cavity.

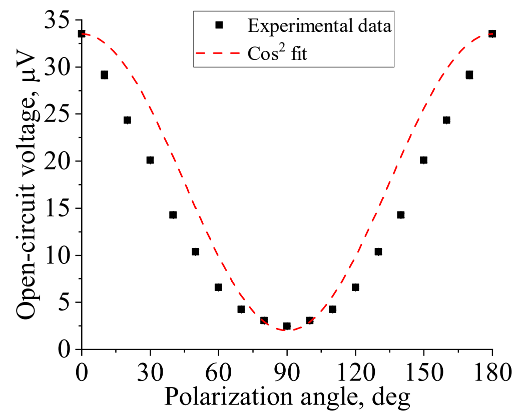

Fig. 5: Polarization dependent response of a 5.5 µm dipole antenna array. The response follows the cosine-squared dependence, expected from a dipole antenna in response to linear polarization excitation.

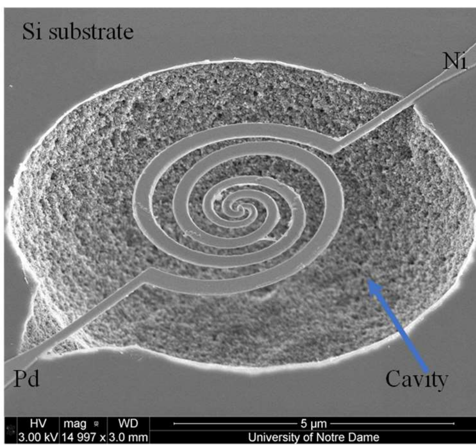

Fig. 3: SEM image of a TECNA with a spiral antenna above a cavity.

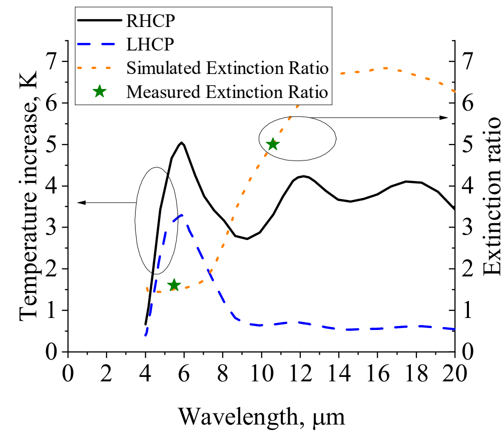

Fig. 6: Simulated spectral response of TECNAs with spiral antennas. The extinction ratio between RHCP and LHCP was experimentally determined at 5.5 µm. and 10.6 µm.

Enhanced Light-Matter Interactions in Shape-Engineered Silicon Phononic – Photonic Superlattice Structures

Fariborz Kargar, Chun-Yu Tammy Huang, and Alexander A. Balandin

Phonon Optimized Engineered Materials (POEM) Center, Department of Electrical and Computer Engineering, Materials Science and Engineering Program, University of California, Riverside, California 92521 USA

E-mail: fkargar@ece.ucr.edu https://balandingroup.ucr.edu

The possibility of controlling the acoustic phonon spectrum in periodic structures has led to an explosive growth in the field of phononic crystals [1-4]. The same periodic structures with properly tuned dimensions can act as photonic crystals affecting the light–matter interactions further. Here, we report on the design and fabrication of the silicon pillar structures, which act simultaneously as phononic and photonic crystals. The "pillar-with-hat" structures were fabricated using the electron beam lithography on a silicon (100) substrates followed by the inductively-coupled plasma cryogenic dry etching. We have used the Brillouin-Mandelstam spectroscopy (BMS) and spectroscopic ellipsometry to reveal intriguing phononic and photonic – also termed *phoxonic* – properties of such superlattices. Acoustic phonon states can be tuned either as a result of phonon confinement effects in individual nanostructures or as a result of artificially induced external periodicity. The shape of the nanoscale pillar array was engineered to ensure the interplay of both effects [3]. The BMS data indicated strong flattening of the acoustic phonon dispersion in the frequency range from 2 GHz to 20 GHz and the phonon wave vector extending to the higher-order Brillouin zones. The specifics of the phonon dispersion dependence on the pillar arrays orientation suggest the presence of both periodic modulation and spatial localization effects for the acoustic phonons. The ellipsometry data reveal a distinct scatter pattern of four-fold symmetry due to nanoscale periodicity of the pillar arrays. Our results suggest a possible new direction for fine-tuning the light-matter interaction in the next generation of photonic and optoelectronic devices [4].

The initial stage of the work was supported, in part, by the DARPA project W911NF18-1-0041 on Phonon Engineered Materials. The design developments for the Brillouin-Mandelstam spectroscopy were supported, in part, by the National Science Foundation (NSF) *via* the Major Research Instrumentation (MRI) project DMR 2019056.

[1] F. Kargar, *et al*., Nature Com, **7**, 13400 (2016).

[2] F. Kargar, *et al*., Appl. Phys. Lett., **112**, 191902 (2018).

[3] C. Y. T. Huang, *et al*., Nanotechnology, **31**, 30LT01 (2020).

[4] F. Kargar and A.A. Balandin, Nature Photon. (2021); https://doi.org/10.1038/s41566-021-00836-5

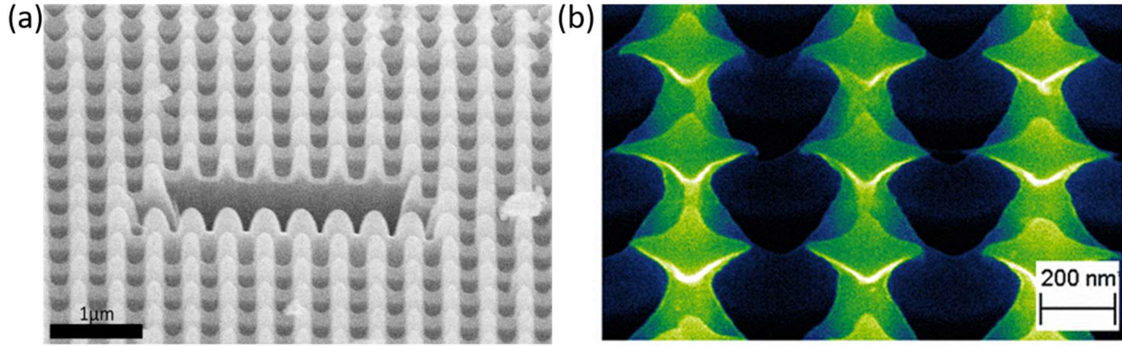

Figure 1: *(a) Top and (b) front SEM views of the pillar-with-hat structures. In the panel (b), the hat structure of the individual pillars is seen more clearly.*

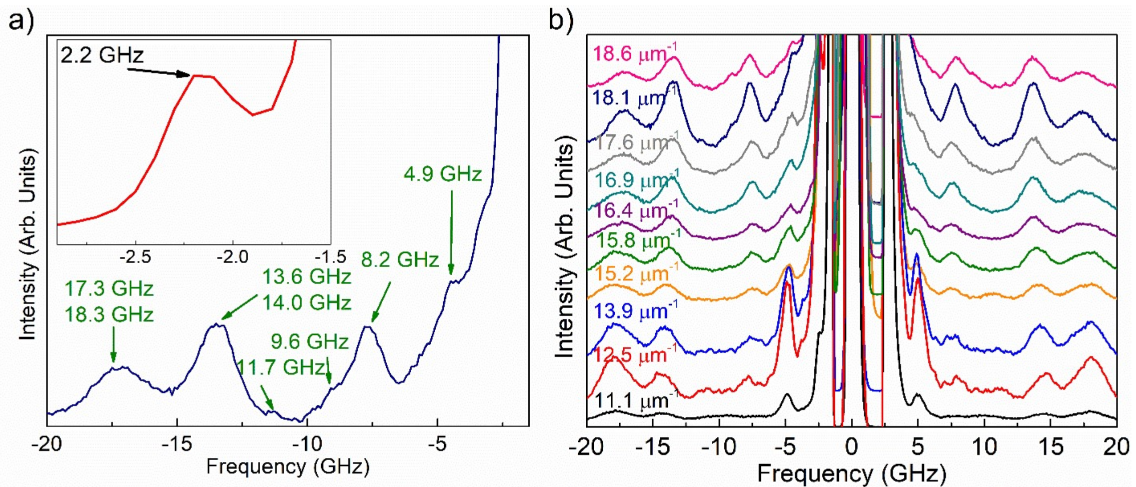

Figure 2: *(a) Measure BMS peaks at the in-plane phonon wave-vector of* $q = 18.1\ \mu m^{-1}$. *The inset shows the same plot in the proximity of 2* GHz *frequency. (b) Evolution of the phonon spectra with changing the laser incident angle and the phonon wave-vector.*

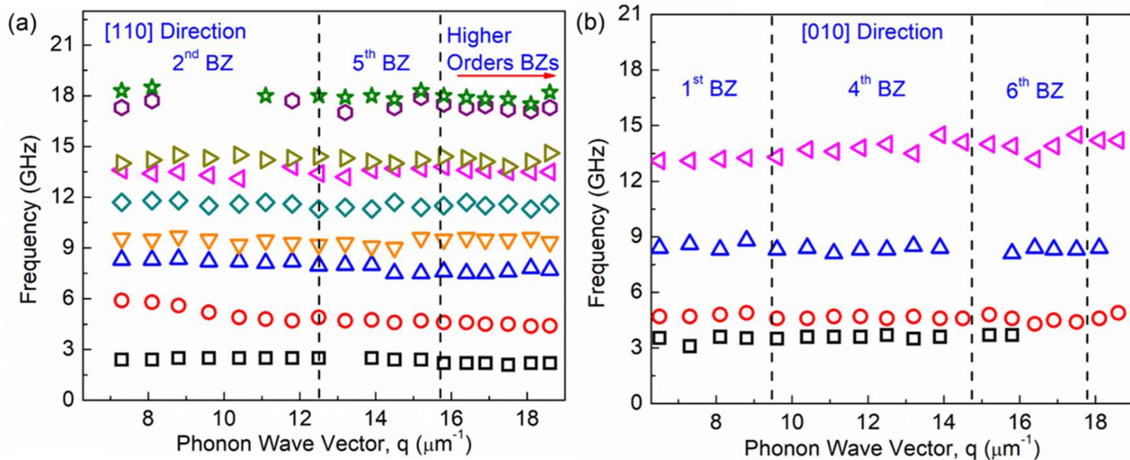

Figure 3: *Experimental phonon dispersion of the pillar-with-hat structures along the (a) [110] and (b) [010] crystallographic directions. The data are obtained by fitting the BMS spectra accumulated at different phonon wave-vectors along different crystallographic directions.*

Infrared Photodetection Using Narrow Bandgap Conjugated Polymers

Jason D. Azoulay
School of Polymer Science and Engineering
University of Southern Mississippi
jason.azoulay@usm.edu

Low-energy, infrared (IR) photon detection forms the foundation for industrial, scientific, energy, medical, and defense applications. State-of-the-art technologies remain dependent on epitaxially grown, lattice-matched, crystalline inorganic devices. These suffer from limited modularity, intrinsic fragility, low speed, high-power consumption, require cryogenic cooling, and are largely incompatible with integrated circuit technologies. Conjugated polymers offer a promising alternative offering low-cost and scalable fabrication, solution processability, room temperature operation, and many other attributes that are not available using current technologies. We have demonstrated the first example of control of the properties of donor-acceptor conjugated polymers in the IR spectral regions ($0.9 < \lambda < 16$ μm). Here, we demonstrate new materials, soft matter systems, and device paradigms that enable an understanding of emergent light-matter interactions and optical to electrical transduction of IR light. Photodiodes show a response to 2.0 μm, while photoconductors respond across the near- to long-wave infrared (NIR–LWIR, $\sim 0.9 < \lambda < 16$ μm). Fundamental investigations of polymer and device physics have resulted in improving performance to levels now matching commercial inorganic detectors. This is the longest wavelength light detected for organic materials and the performance exceeds that of graphene at longer wavelengths. Photoconductors outperform their inorganic counterparts and operate at room temperature with higher response speeds.

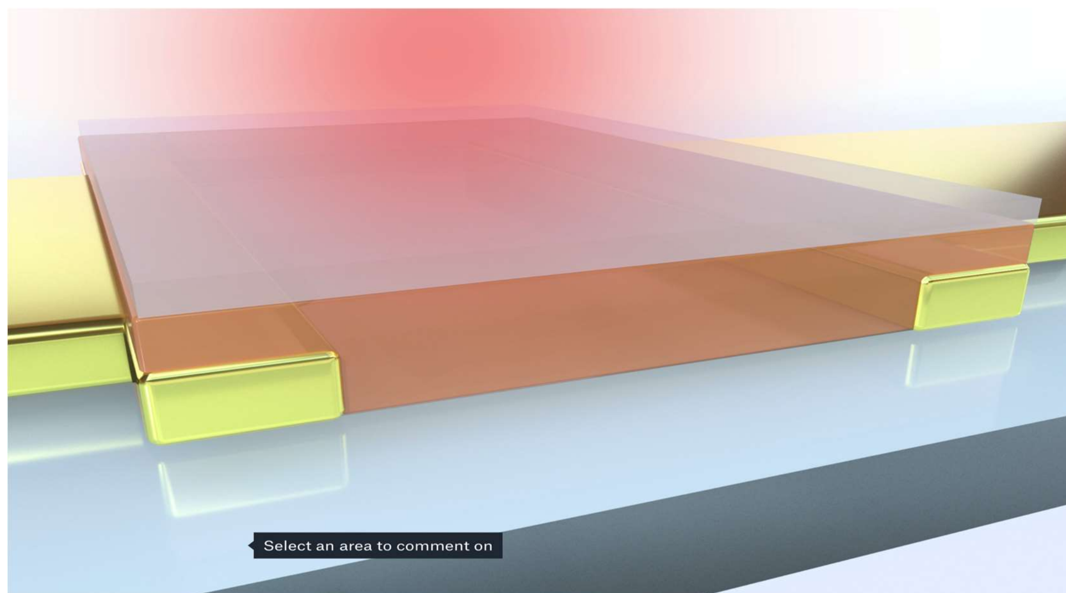

978-3-9504738-3-4

Improving MIM Diode Performance with Precisely Placed ALD Ti Defects

K.E.K. Holden,[1] B. M. Kupp,[2] J. Peterson,[1] and J.F. Conley, Jr. [1,2,*]
(Times New Roman, 12pt)
[1]*School of EECS, Oregon State University, Corvallis, OR, 97331*
[2]*Materials Science Program, Oregon State University, Corvallis, OR, 97331*
**jconley@eecs.oregonstate.edu*

Metal/insulator/metal (MIM) diodes promise ultra-fast rectification for applications in THz energy harvesting and detection. Previous methods for reducing MIM turn-on voltage (V_{ON}) and increasing current-voltage (*I-V*) asymmetry (f_{asym}) include the use of multiple insulators (MIIM, MIIIM) to promote resonant or "step" tunneling, geometric field enhancements (using, e.g., carbon nanotubes), and intrinsic defects to promote defect-enhanced conduction [1]. Recently, we applied atomic layer deposition (ALD) to place *extrinsic* Ni defects (D_{Ni}) at precise locations in the Al_2O_3 tunnel barrier of MIM diodes with the intent of promoting asymmetric trap-assisted tunneling (TAT) [2]. While f_{asym} was improved, V_{ON} increased, likely due to negative charge trapped at Ni defect states lying energetically near or below the equilibrium Fermi level ($E_{F,equil}$) of the electrodes. To promote asymmetric TAT, the defect states in the insulator gap should ideally lie above $E_{F,equil}$ (Fig. 1(a)). In Al_2O_3, it is predicted that Ti defect states should lie *above* the $E_{F,equil}$ of typical electrodes [3]. In this work, we use ALD to precisely place Ti defects (D_{Ti}) in Al_2O_3 based MIM diodes with dissimilar top and bottom electrodes (Fig. 1(b)).

ALD of Al_2O_3 using 100 cycles of $Al(CH_3)_3$ & H_2O at 300 °C was interrupted near the *Bottom, Middle*, and *Top* by two cycles of $Ti(O(CH_3)_2)_4$ & H_2O to place D_{Ti}. Current density-electric field (*J-E*) plots (Fig. 2) for Ti modified Pt/Al_2O_3(Ti)/Ag M_1IM_2 devices demonstrate the impact of D_{Ti}. For all electrode combinations, the *Middle* device is reduced to $f_{\text{asym}} \approx 1$, while the *Top* and *Bottom* devices retain $f_{\text{asym}} > 1$. The largest improvement (reduction) in V_{ON} with minimal impact to f_{asym} occurs for the *Top* device when $\Phi_{M2} > \Phi_{M1}$ (Fig. 3). When D_{Ti} is placed directly at either electrode interface, there is comparatively little effect on *J-E* behavior. Asymmetric TAT is likely responsible for reduced V_{ON} in the *Top* device while in all other instances, trapped positive charge at D_{Ti} likely reduces the onset of Fowler-Nordheim tunneling.

Using ALD to intentionally introduce Ti defect layers, we demonstrate enhanced performance of Al_2O_3-based MIM diodes. Capacitance-voltage (*C-V*), *I-V* versus temperature, and internal photoemission (IPE) spectroscopy are used to reveal the underlying mechanisms responsible for improvement (likely TAT) and will be discussed at the meeting.

[1] N. Alimardani and J.F. Conley, Jr. Appl. Phys. Lett. **105**, 082902 (2014).
[2] K.E.K. Holden, Y. Qi, and J.F. Conley, Jr. J. Appl. Phys. 129, 144502 (2021).
[3] Ichimura, J. Electron. Mater. **48**, 583 (2018).

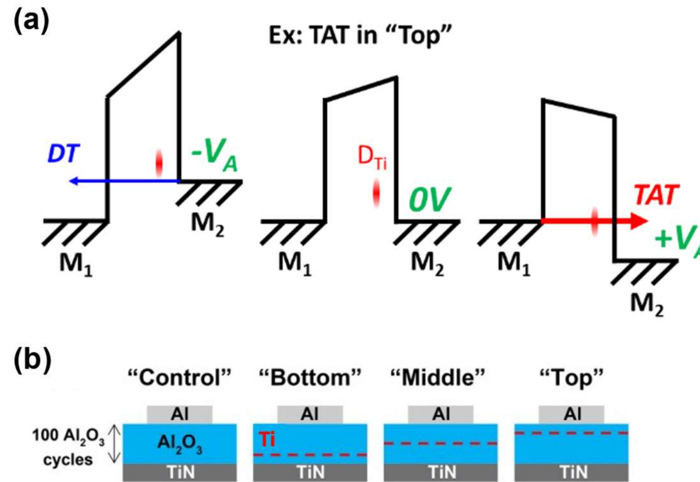

Fig. 1. (a) Band diagrams illustrating the intended effect of asymmetric trap-assisted tunneling in the "Top" device. (b) Schematic of ALD Ti defect layer (D_{Ti}, red dashes) placement inside the Al_2O_3 tunnel barrier with naming convention provided.

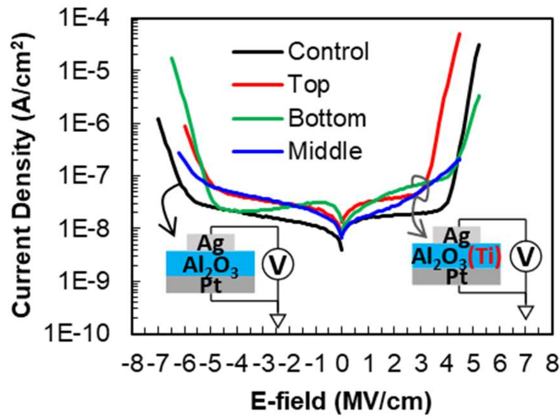

Fig. 2. Current density versus electric field sweeps (plotted after the 5th sweep) for $Pt/Al_2O_3/Ag$ MIM diodes without (black) and with D_{Ti} (colored) placed inside the Al_2O_3 tunnel barrier using ALD. Voltage bias is applied to the Ag top electrode while the Pt bottom electrode is grounded, as indicated with inset device cross-sections.

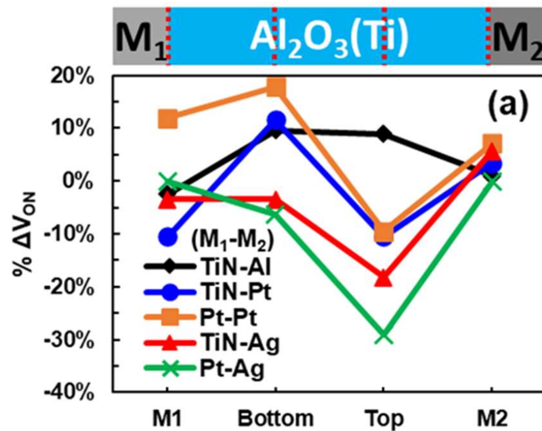

Fig. 3. Percent change in V_{ON} from the control device as a function of D_{Ti} placement ranging from the M_2/Al_2O_3 interface to the M_1/Al_2O_3 interface, for different electrode arrangements (color-coded). The "Middle" device is excluded due to highly symmetric behavior in all devices.

Optimization of matching networks for nanoscale charge and voltage sensors using reflectometry

M.Huebner, J. Chisum, A.O. Orlov, A.M.Mintairov, and G.L. Snider
Department of Electrical Engineering, University of Notre Dame, Notre Dame, USA
aorlov@nd.edu

Broadband sensing of nanodevices for applications such as high-speed qubit readout using spin to charge conversion and natural anyon molecules [1] is often accomplished using gate radio-frequency reflectometry of quantum dots (QD) [2, 3], Fig. 1. The parameter of interest is the change in the impedance of the QD resulting from single-electron charging accompanied by a change in the dynamic capacitance [4, 5]. The impedance variation associated with this process is small compared to the impedance of pad capacitance C_{pad} in parallel with QD. Sensitive measurements of such systems therefore are only possible if a properly designed matching network (MN) is used. The purpose of the MN is to convert the large impedance of C_{pad} || Z_{QD} into a value Z_{IN} close to characteristic impedance of transmission line Z_0=50 Ω. For properly designed MN a small change in Z_{QD} will result in a noticeable change of Z_{IN}. We use low temperature calibration and error correction procedure to achieve quantitatively accurate optimization of the measurement system for targeted bandwidth (BW) using single port reflectometry for various settings of the MN, Fig. 2. To test the effectiveness of MN for gate reflectometry we use arrays of parallel-connected Al-AlO_x single electron boxes as a robust prototype of QD which can withstand multiple thermal cycles, Fig. 3. Experiment shows that the design and simulations of MN must take into consideration parasitics of the components comprising MN to avoid errors in evaluation of sensitivity and bandwidth. Figure 4 shows a comparison of Coulomb blockade oscillations generated by array of 40 SEB for two settings of MN. We experimentally demonstrate that by using a properly designed MN one can achieve more than 30 dB improvement in an SNR. By achieving close-to-match conditions we achieve the most efficient energy transfer from QD to a measurement system, Fig. 5. As a result, the negative impacts of various non-idealities are canceled to in contrast with mismatched conditions. The obtained experimental results are in good agreement with the simulations, Fig. 6. This work was supported by the National Science Foundation Grants ECCS-1509087 and DMR-1904610

1. Mintairov, A., et al., Scientific Reports, **11**, 21440 (2021)
2. Crippa, A., et al., Nano Letters, 2017. **17**(2): p. 1001-1006.
3. Gonzalez-Zalba, M.F., et al., Nature Communications, 2015. **6**(1): p. 6084.
4. Zimmerman, N.M. and M.W. Keller, JAP, 2000. **87**(12): p. 8570-8574.
5. Mizuta, R., et al., Physical Review B, 2017. **95**(4): p. 045414.

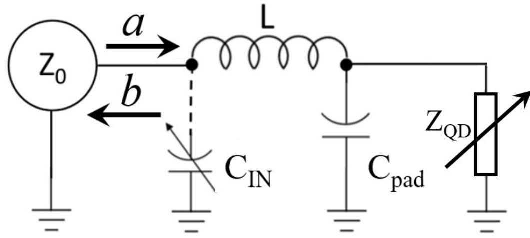

Fig.1: Generic schematic of gate reflectometry measurement. a and b represent incoming and reflected waves measured by a reflectometer with input impedance Z_0. Quantum dot impedance is represented by a variable impedance Z_{QD}. Components C_{IN}, L and C_{pad} are forming the Π matching network. C_{IN} is a balancing capacitor used to tune MN .

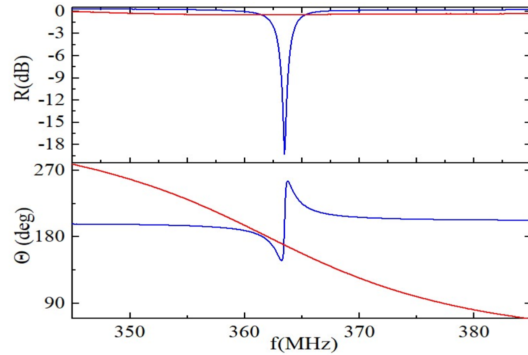

Fig.2: Experimental comparison of magnitude and phase response of MN for two cases : mismatched network, CIN=0, matched network, CIN=30 pF. L=270 nH, T=4K. Data are error corrected using calibration and error correction protocol

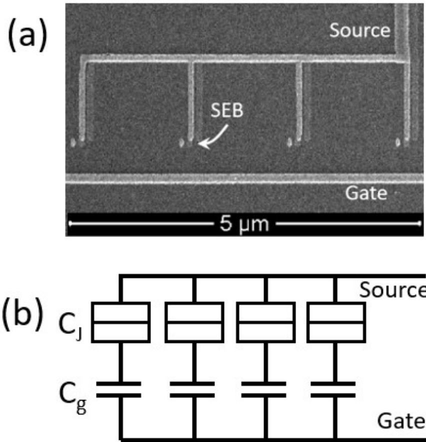

Fig.3: Electron micrograph (a) and circuit diagram (b) of the array consisting of 4 SEBs with shared source and gate. Overlap area that defines junction capacitor C_J is ≈ 1000 nm^2.

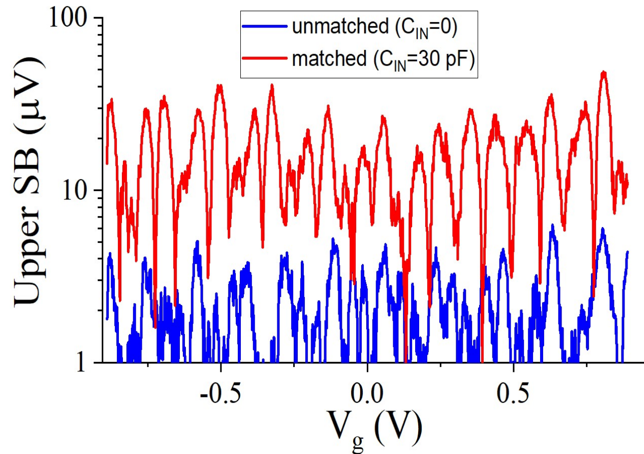

Fig.4: Coulomb blockade oscillations recorded as a magnitude of reflected side band for an array of 40 SEB. Blue curve - unmatched case, red – well matched case. The average SNR improvement is about 31 dB

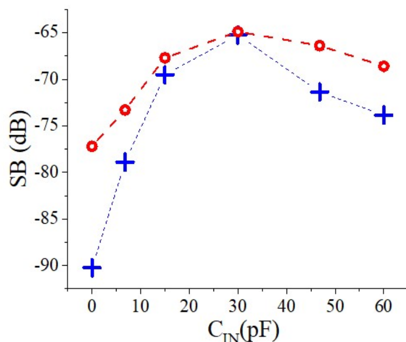

Fig.5: Simulated and measured dependence of sensitivity of 200 SEB array on balancing capacitor C_{IN} for MN composed of Cpad=470 fF, nd L= 240 nH Coilcraft 0805 LS chip inductor. f_{Mod}=8 kHz, modulation magnitude 0.07e. Note that simulations assume ideal reflectometer.

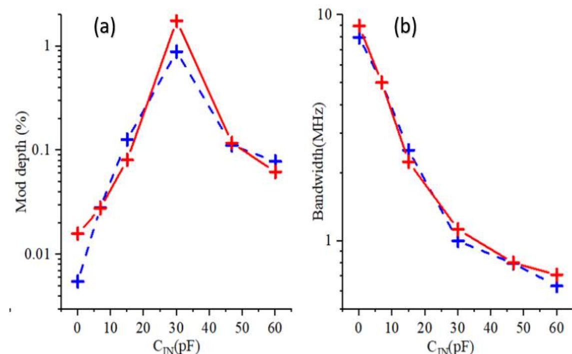

Fig.6: Simulated and measured dependence of modulation depth and bandwidth dependence on the value of balancing capacitance C_{IN}.

978-3-9504738-3-4

Quantization of Semiconductor Nanostructures and Singlet Fission: Applications to Future Approaches for Highly Efficient Solar Photon Conversion to PV and Solar Fuels.

A.J. Nozik[1]

[1]*Department of Chemistry and Renewable & Sustainable Energy Institute (RASEI)*
University of Colorado, Boulder, CO 80309, USA
and
National Renewable Energy Laboratory (NREL)
Golden, CO 80401, USA
arthur.nozik@colorado.edu

In order to utilize solar power for the production of solar electricity and solar fuels on a global scale, it will be necessary to develop solar photon conversion systems that have an appropriate combination of high efficiency (delivered watts/m^2) and low capital cost (\$/m^2). One potential, long-term approach to attain high conversion efficiencies above the well-known Shockley-Queisser thermodynamic limit of 32% is to utilize the unique properties of quantum dot/rod/film (QD/QR/QF) nanostructures to control the relaxation dynamics of photogenerated carriers to produce either enhanced photocurrent through efficient photogenerated electron-hole pair multiplication or enhanced photopotential through hot electron transport and transfer processes. To achieve these desirable effects it is necessary to understand and control the dynamics of hot electron and hole relaxation, cooling, charge transport, and interfacial charge transfer of the photogenerated carriers. These fundamental dynamics in various bulk and nanoscale semiconductors have been studied for many years using transient absorption, photoluminescence, photocurrent, and THz spectroscopy with fs to ns time resolution The prediction that the generation of more than one electron-hole pair per absorbed photon (which exist as multiple excitons) in size-quantized nanostructures and special molecules would be an efficient process has been confirmed over the past years in different classes of materials and their architectures. Very efficient and ultrafast multiple exciton generation (MEG), also called Carrier Multiplication (CM), from absorbed single high energy photons has been reported in many quantized semiconductors and associated solar photon conversion devices for solar electricity and solar fuels (e.g. H_2) production. Selected aspects of this work will be summarized and recent advances will be discussed, including the very remarkable and beneficial theoretical effects of combining MEG and/or SF with solar concentration and controlling the thicknesses of the photoactive layers in a two-photon cell structure for solar fuels. Finally, the analogous MEG effect (called singlet fission (SF)) in special molecules and its use in molecular-based solar cells will also be discussed.

Controlling photons and electromagnetic waves for energy applications

Shanhui Fan[1]
[1]*Department of Electrical Engineering and Ginzton Laboratory, Stanford University, Stanford, California 94305, USA*
shanhui@stanford.edu

In this paper we discuss some of our recent efforts in controlling photons and electromagnetic waves for energy applications. In particular, we discuss the design of non-reciprocal thermal emitters, and the implications of such emitters for reaching the Landsberg limit of solar energy conversion [1]. We also show that the optoelectronic physics can be used to create a photonic voltage transformer that allows voltage converter for direct current [2]. Such a voltage transformer overcomes many of the difficulties associated with conventional switch mode converter widely used for direct current voltage converter.

[1] Y. Park, V. S. Asadchy, B. Zhao, C. Guo, J. Wang, and S. Fan, "Violating Kirchhoff's Law of Thermal Radiation in Semitransparent Structures," ACS Photonics 8, 2417–2424 (2021).
[2] B. Zhao, S. Assawaworrarit, P. Santhanam, M. Orenstein, and S. Fan, "High-performance photonic transformers for DC voltage conversion," Nature Communications 12, 4684 (2021).

978-3-9504738-3-4

Valley photovoltaics: A new approach towards the hot carrier solar cell

H. Esmaeilpour[1], K. R. Dorman,[1] D. K. Ferry[1], V. R. Whiteside[1], J. Tang[1], T. D. Mishima, M. B. Santos[1], and I. R. Sellers[1]

[1]Department of Physics & Astronomy, University of Oklahoma, Norman, OK 73019, USA
2 School of Electrical, Computer, and Energy Engineering, Arizona State University, Tempe AZ 85287, USA
e-mail: sellers@ou.edu

Hot Carrier Solar Cells (HCSCs) are a proposed next-generation photovoltaic technology for overcoming the single-gap efficiency limit. Through maintenance of a population of high energy ("hot") carriers and extraction at better than band gap photovoltage, an enhanced solar conversion efficiency could be maintained. Proof-of-principle has been demonstrated for hot carrier generation and maintenance, both by mitigating thermalization mechanisms through the creation of a so-called phonon bottleneck in quantum wells, and through exploitation of intervalley scattering mechanisms to stabilize hot carriers in upper valleys of the band structure in the emerging field of *valley photovoltaics* (VPs) [1-3]. Intervalley scattering properties of an InGaAs absorber have been shown to provide an accessible pathway for VP hot carrier operation [2], removing high energy carriers from the Γ valley for extraction via the L or X valley [1, 2]. However, further development of this VP architecture is required to enhance the solar cell operation that increases both the efficacy of carrier extraction from the satellite valleys, and the establishment of electric fields inside the device to provide lower energy carriers access to this upper valley extraction pathway [3]. Here, our latest work in developing protocols for effective hot carrier extraction and field aided scattering will be presented. A study of various absorber/selective barrier material combinations provides insight into current bottlenecks towards the realization of a VP HCSC, and how these might be circumvented using several complementary experimental techniques.

This research is funded through Department of Energy EPSCoR Program and the Office of Basic Energy Sciences, Material Science and Energy division under Award No. # DE-SC0019384.

[1] H. Esmaielpour, D. K. Ferry, V. R. Whiteside, I. R. Sellers *et al.*, Nature Energy 5, 336 (2020)
[2] D. K. Ferry, Semiconductor Science & Technology 34, 044001 (2019)
[3] D. K. Ferry, S. M. Goodnick, V. R. Whiteside, and I. R. Sellers, Journal of Applied Physics 128, 220903 (2020)

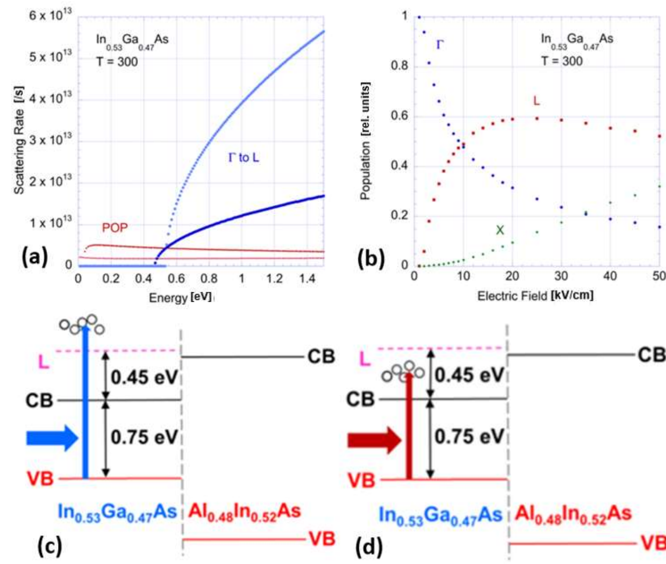

Fig. 1. (a) Scattering rates in InGaAs of intervalley phonons (blue) and polar optical phonons (red) as a function of energy [2]. The upper branch of the blue plot is the Γ to L emission, with the absorption beneath it. (b) Relative population of the Γ, L and X valleys of InGaAs as a function of electric field [2]. The alignment of the top interface of the proof-of-concept device, with accessibility of the L valley to blue (c) and infrared (d) monochromatic excitation [1].

Seeking Nirvana (Hot Carrier Solar Cells)

D. K. Ferry

School of Electrical, Computer, and Energy Engineering, Arizona State University
Tempe, AZ 85287 USA

Hot carrier solar cells were first proposed by Ross and Nozik many decades ago [1]. Over the intervening years, there has been a continuing quest to create these cells which hold promise to shatter the Shockley-Queisser efficiency limit [2] on single-junction solar cells. While there have been many suggestive results in recent years, there remains no true operational hot carrier solar cell. In this corner of the larger solar cell world, and perhaps beyond, there are some misconceptions and misguided approaches. In this talk, two of these will be discussed: (1) the love of efficiency, and (2) narrow-band energy-selective contacts. A more rational interpretation of both of these will be discussed. Then, the valley photovoltaics approach [3] will be briefly reviewed.

[1] R. T. Ross and A. J. Nozik, J. Appl. Phys. **53**, 3813 (1982).
[2] W. Shockley and H. J. Queisser, J. Appl. Phys. **32**, 510 (1961).
[3] D. K. Ferry, Semicond. Sci. Technol. **34**, 044001 (2019).

Hot phonon and intervalley effects on the steady-state temperature of electrons in InGaAs Multi-Quantum Wells

Y. Zou[1], H. Esmaielpour[2], D. Suchet[2,3], J.-F. Guillemoles[2,3], S. M. Goodnick[1]
[1]School of Electrical, Computer and Energy Engineering, Arizona State University, Tempe, AZ 85281, USA
[2]CNRS-Institut Photovoltaique d'Ile de France (IPVF), UMR IPVF 9006, 91120 Palaiseau, France
[2]CNRS-Ecole Polytechnique, UMR IPVF 9006, 91120 Palaiseau, France
Yongjie.Zou@asu.edu

Conventional solar cells extract carriers at the band edge of the absorber material, while losing all the excess energy of the photoexcited carriers through thermalization loss, which is severely limits the conversion efficient of solar cells. Hot carrier solar cells attempt to overcome this limitation by extracting carriers at energies well above the band edges, which requires a strongly nonequilibrium carrier distribution under photoexcitation [1,2]. Hence understanding of the thermalization dynamics in nanostructured materials is essential in realizing cells capable of extracting hot carriers. Towards this goal, in the present work we compare ensemble Monte Carlo (EMC) simulation of carrier dynamics in semiconductor multi-quantum well (MQW) structures with ultrafast optical studies. The EMC simulations include nonquilibrium hot phonon effects, intervalley scattering, carrier-carrier scattering and degeneracy effects, as well as the conventional scattering mechanisms in III-V materials, all within a multi-subband framework for MQW structures [3]. The electron-hole temperatures in an InGaAs multi-quantum-well structure under 405 nm and 980 nm continuous wave (cw) optical excitation have been extracted from photoluminescence (PL) spectroscopy, where high carrier temperatures under cw photoexcitation conditions havebeen reported [4]. The electron temperatures calculated with a realistic LO phonon lifetimes using EMC simulation show good agreement with the experimentally measured carrier temperatures. Further EMC analysis shows the hot-electron temperature is predominantly due to nonequilibrium LO phonons, with a significant fraction of carriers residing in the upper L-valleys, as has recently been reported [5,6].

[1] L. C. Hirst & N. J. Ekins-Daukes, Prog. Photovoltaics Res. Appl. **19**, 286–293 (2011).
[2] Y. Rosenwaks *et al.*, Phys. Rev. B **48**, 14675–14678 (1993).
[3] R. Hathwar *et al.*, J. Phys. D. Appl. Phys. **52**, 093001 (2019).
[4] H. Esmaielpour *et al.*, Nat. Energy **5**, 336–343 (2020).
[5] V. R. Whiteside *et al.*, Semicond. Sci. Technol. **34**, 094001 (2019).
[6] D. K. Ferry, Appl. Phys. Rev. **8**, 1–27 (2021).

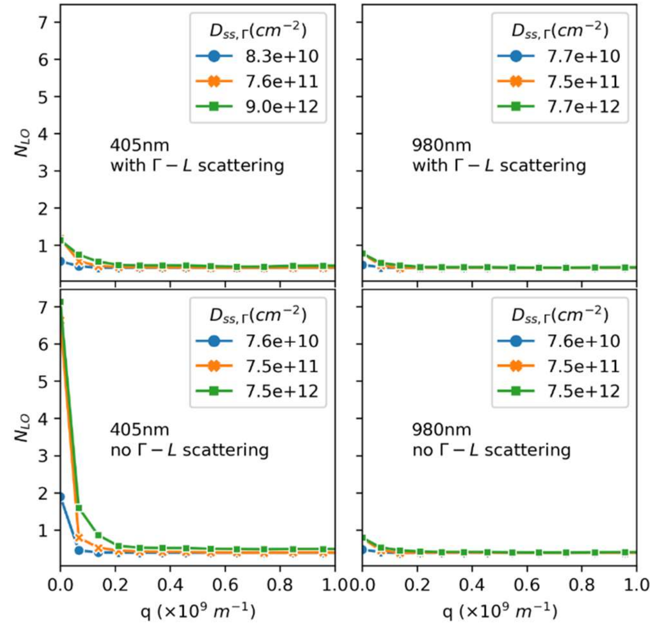

Fig.1: LO phonon occupation as a function of wavevector q, for different excitation wavelengths and carrier densities, with and without intervalley Γ-L scattering.

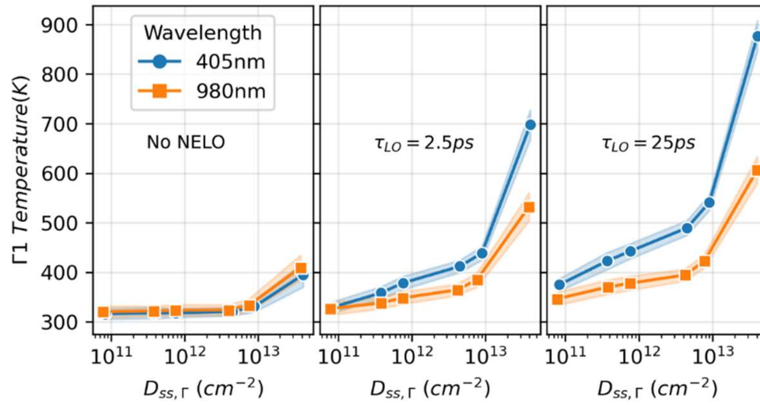

Fig.2: EMC steady-state temperatures of electrons in the Γ_1 with 405 nm and 980 nm excitation for different LO phonon lifetime.

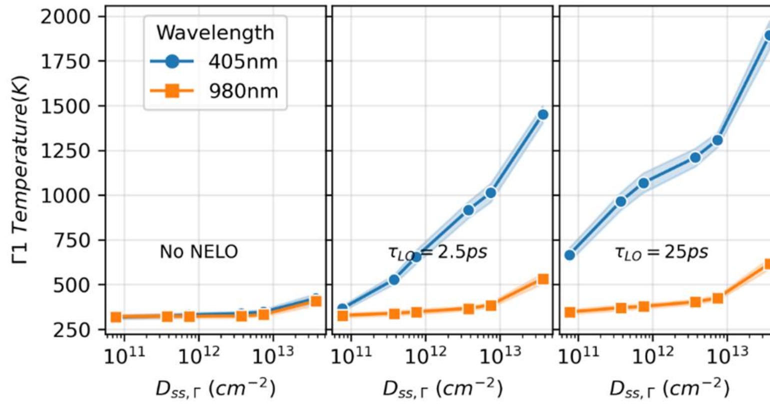

Fig.3: EMC steady-state temperatures of electrons in the Γ_1 with 405 nm and 980 nm excitation for different LO phonon lifetime, by artificially disabling Γ-L scattering.

978-3-9504738-3-4

An entertaining physics: On the possibility of energy storage enhancement in electrostatic capacitors using the compensational inductive electric field.

Alexander Khitun
Department of Electrical and Computer Engineering, University of California – Riverside, Riverside, California, 92521, USA.
akhitun@engr.ucr.edu

In this work, we consider the possibility of energy storage enhancement in electrostatic capacitors using the compensational method. The essence of the proposed approach is the use of inductive voltage V_{ind} to partially compensate the electrostatic voltage q/C produced by the electric charges on the capacitor plates. We hypothesize that it may be possible to increase the amount of charge stored on the plates before the breakdown and increase the energy stored in the capacitor using the compensational inductive voltage. There are several possible scenarios of manipulating the inductive voltage to increase the amount of energy released via the discharge. We also consider several electro-magnetic capacitors for practical utilization. Potentially, the energy per volume stored in a simple parallel plate capacitor may exceed the one of gasoline. The physical limits and technological shortcomings of the proposed approach are also discussed.

A. Khitun, Applied Physics Letters 117(15):153903, (2020)

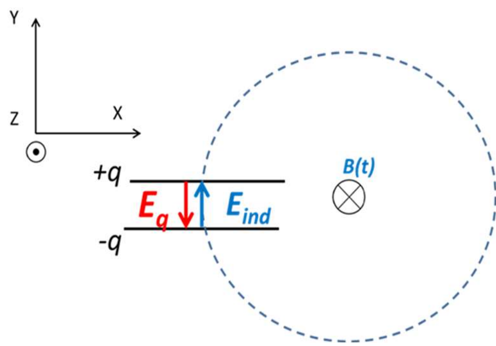

Fig.1: Schematics of a parallel-plate capacitor in a time-varying magnetic field B. The red and the blue arrows show the direction of the electrostatic $\vec{E}_q$ and the inductive electric field $\vec{E}_{ind}$, respectively. The direction of the inductive field is chosen to compensate the electrostatic field.

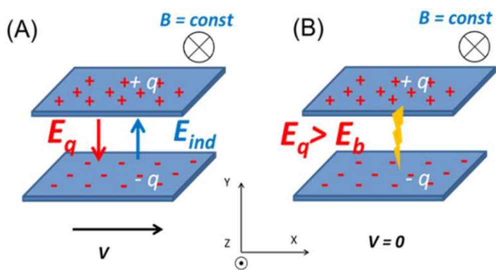

Fig.2: Illustration of using the magnetic part of the Lorentz force for compensating the force of electrostatic attraction. (A) A parallel plate capacitor is moving with constant velocity $v > 0$ in the constant and uniform magnetic field B. The direction of motion is chosen such that the magnetic part of the Lorentz force compensates the force of electrostatic attraction. (B) The capacitor is instantly stopped ($v = 0$). The electric field across the plates is defined by the charge only.

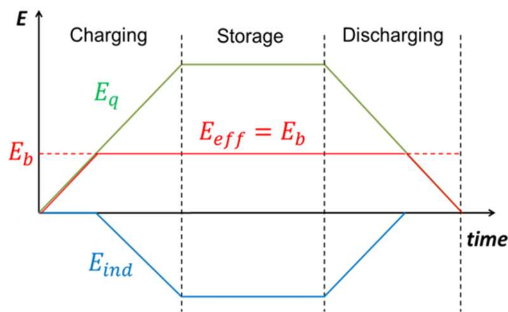

Fig.3: Illustration of the principle of operation. The charging of the capacitor starts at zero inductive electric field E_{ind}. As the electric field produced by charges E_q approaches the breakdown value E_b, the source of magnetic field is turned on to provide the inductive electric field E_{ind}. The inductive field E_{ind} is directed opposite to E_q to compensate the charge-induced electric field. The charging is continued till some charge is stored on the plates. In the storage regime, the inductive field E_{ind} remains constant. The effective magnetic field is kept close to E_b till the last electron is discharged.

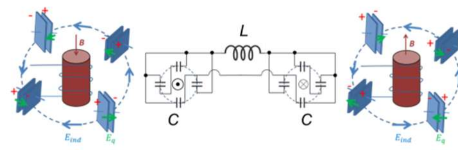

Fig.4: Schematics of a complementary electro-magnetic device comprising two coupled oscillators. Each oscillator is shown to have four parallel plate capacitors placed around a source of time varying magnetic field . The rate of magnetic field change is adjusted to compensate the electrostatic force of attraction between the charges on the capacitor plates.

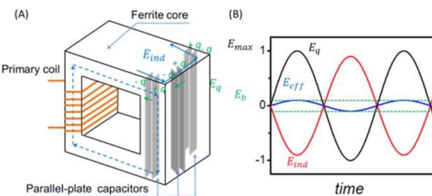

Fig.5 A) Schematics of the proposed electro-magnetic capacitor 1. There are shown three parallel-plate capacitors placed inside a ferrite core. The compensational inductive filed is provided by AC in the primary coil. (B) Results of numerical modeling showing the electrostatic (black curve) and inductive (red curve) fields oscillating in time. The total effective field is below the breakdown value (dotted green lines).

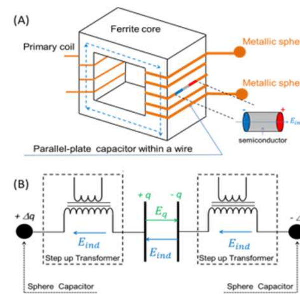

Fig.6: (A) Schematics of the proposed electro-magnetic capacitor 2 where the parallel-plate capacitors are placed inside the secondary coil of the transformer. The capacitor is formed by replacing a part of the coil by a semiconductor. (B) The equivalent circuit. It is an open circuit comprising a parallel plate capacitor (in the center), two step-up transformers, and two sphere capacitors at the edges. The inductive voltage completely compensates for the electrostatic potential difference between the plates. There is zero leakage current in the secondary coil.

Sensing with Quantum Cascade and Interband Cascade Devices

Gottfried Strasser
Institute of Solid State Electronics and Center for Micro- and Nanostructures
Technische Universität Wien, Fakultät für Elektrotechnik und Informationstechnik
gottfried.strasser@tuwien.ac.at

This talk aims to give a short introduction in the field of quantum cascade and interband devices with a strong focus on quantum cascade lasers (QCLs), interband cascade lasers (ICLs) and detectors (QCDs and ICDs).

Since the first proposal using intraband transitions in QWs to achieve lasing intraband and interband cascade lasers have been intensively studied in terms of bandstructure engineering, cavity design and fabrication technology. Nowadays, QC lasers are compact and coherent light sources covering the spectral range from the mid-infrared to the terahertz region.

Recent advances in chemical sensing applications are based on surface and/or substrate emitting QCLs [1]. The low threshold power of ICLs makes them very attractive for mobile systems. We will report on substrate emitting ICL ring lasers [2] (Fig. 1).

In addition to QC lasers we report on the design, fabrication, and characterization of MIR QCDs optimized for large electrical bandwidth. QCDs are photovoltaic mid-infrared detectors based on intersubband transitions. The sub-picosecond carrier transport between subbands and the absence of a bias voltage of QCDs is interesting for high-speed applications at room temperature [3] (Fig. 2). Using femtosecond pulses generated by a mid-infrared optical parametric oscillator, the impulse response of QCDs has a full-width at half-maximum of less than 5 ps. Considerable detection capability beyond the 3-dB bandwidth is reported up to at least 50 GHz. Interband cascade detectors (ICDs) combine interband optical transitions with fast intraband transport to achieve high-frequency and broad-wavelength operation at room temperature [4] (Fig. 3). Bias-dependent electronic impulse response of ICDs with a mid-infrared synchronously pumped OPO shows two decay times. A reverse bias voltage applied to the ICD reduces both time scales and leads to an increased electrical cut-off frequency.

[1] B. Hinkov, et al., Optics Express **27**(10), 14716-14724 (2019)
[2] H. Knötig, et al., Appl. Phys. Lett. **116**(13), 131101 (2020)
[3] J. Hillbrand, et al., Optics Express **29**(4), 5774-5781 (2021).
[4] L.M. Krüger, et al., Optics Express **29**(9), 14087-14100 (2021).

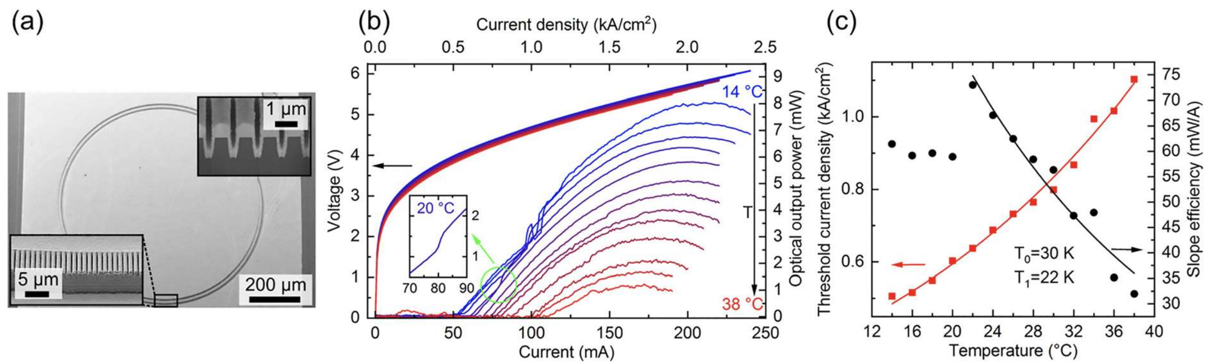

Fig. 1. (a) Scanning electron micrograph of a fabricated ring interband cascade laser. The top right inset shows an image of a FIB cut in the middle of the waveguide through the grating structure. (b) Light–current–voltage characteristics of the ring ICL in cw operation. The inset shows a jump in optical output power at a temperature of 20 C. (c) Threshold current densities (red squares) and differential slope efficiencies (black circles) measured at different heatsink temperatures and the corresponding fits (red and black lines) are shown. (From Ref 2).

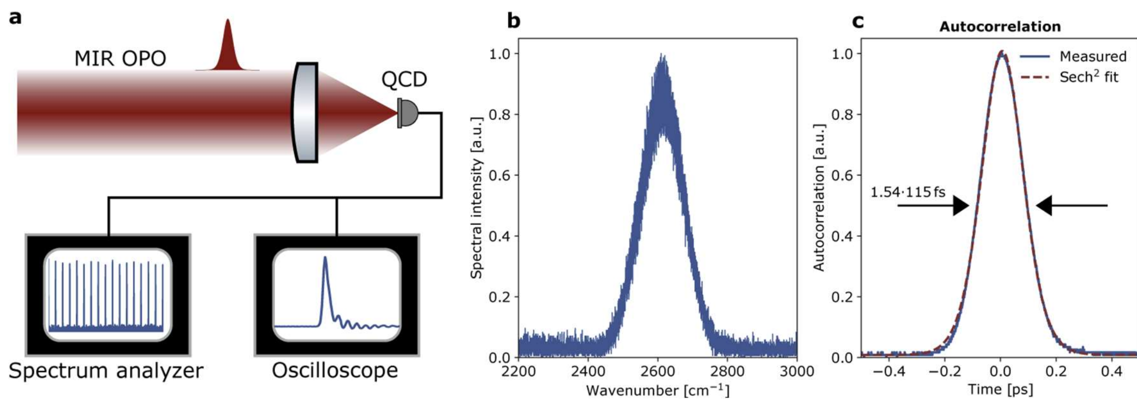

Fig. 2. a: experimental setup for measuring the impulse response of the QCD using femtosecond pulses. b: optical spectrum of the OPO operating around 3.85 µm. The FWHM of the spectrum is approximately 130 cm−1, suggesting a transform limited pulse duration of 115 fs. c: autocorrelation of the OPO pulses operating at 3.3 µm. At 3.85 µm, the response of the InGaAs detector used in the autocorrelator is decreased considerably. We estimate that the pulse width is increased to 140 fs. (From Ref. 3).

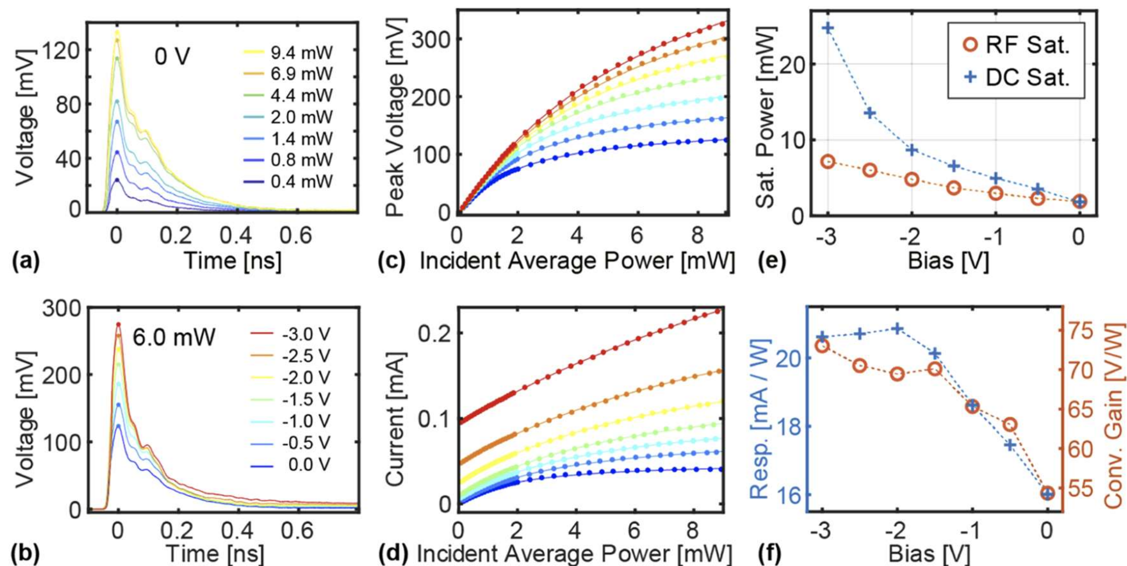

Fig. 3. (a) Power-dependent temporal response of the unbiased interband cascade infrared photodetector (ICIP). The signal-to-noise ratio was improved by averaging 128 consecutive traces for each power value. (b) Bias-dependent temporal response at an incident average power of 6.0 mW. The applied reverse bias ranges from 0 V (blue curve) to -3 V (red curve). (c) Generated peak voltage and (d) Photocurrent as a function of incident average power and applied bias. (e) Fitted saturation power to RF voltage response (orange circles) and DC photocurrent (blue crosses). (f) The fitted responsivity of DC photocurrent response (blue crosses) as well as maximum conversion gain of the voltage RF response (From Ref. 4).

Recent Progress Toward Colloidal Quantum Dot Laser Diodes

H. Jung, N. Ahn, Y.-S. Park, I. Fedin, C. Livache, and V. I. Klimov
Chemistry Division, Los Alamos National Laboratory, Los Alamos, New Mexico, USA
klimov@lanl.gov

Due to high emission efficiencies and size-controlled emission wavelengths, colloidal quantum dots (QDs) are attractive materials for the realization of solution-processable laser diodes [1, 2]. In addition to facile spectral tunability, QD gain media benefit from a wide separation between their atomic-like states, which inhibits thermal depopulation of the band-edge 'emitting' levels and thereby reduces lasing thresholds and improves temperature stability [3]. Despite these advantageous features, colloidal QD lasers are yet to reach the stage of technologically viable devices. A primary obstacle is nonradiative Auger recombination, which leads to very fast relaxation of optical gain [4]. This represents an especially serious challenge in the case of inherently slow electrical pumping when multiexciton states, required for optical gain, are generated via step-by-step injection of individual carriers. Another complication is poor stability of QD solids under high current densities needed to enact the lasing effect. Here we are able to resolve these challenges and achieve broad-band optical gain spanning the band-edge (1S) and the higher-energy (1P) transitions. This demonstration is enabled by continuously graded QDs with strongly suppressed Auger recombination (Fig. 1a) [5], incorporated into a current-focusing electroluminescent device driven by short electrical pulses (Fig. 1b). Using this approach, we achieve ultra-high current densities of >1000 A cm^{-2} and, as a result, boost device brightness to ~10 million cd m^{-2}. Furthermore, we realize unusual two-band electroluminescence, in which the intensity of the higher-energy 1P feature exceeds that of the lowest-energy 1S band (Fig. 1c). This observation provides direct evidence for extremely high excitonic occupancies realized in our devices (up to ~8 excitons per dot) that are sufficient to achieve optical gain saturation for both 1S and 1P transitions (Fig. 1d).

[1] Y.-S. Park, J. Roh, B.T. Diroll, R.D. Schaller, V.I. Klimov, Colloidal quantum dot lasers, Nature Reviews Materials **6,** 382 (2021).
[2] H. Jung, N. Ahn, V.I. Klimov, Prospects and challenges of colloidal quantum dot laser diodes, Nature Phot. **15**, 643 (2021).
[3] Y. Arakawa, H. Sakaki, Multidimensional Quantum Well Laser and Temperature-Dependence of Its Threshold Current, Appl. Phys. Lett. **40,** 939 (1982).
[4] V.I. Klimov, A.A. Mikhailovsky, A. Malko, J.A. Hollingsworth, C.A. Leatherdale, H.J. Eisler, M.G. Bawendi, Optical gain and stimulated emission in nanocrystal quantum dots, Science **290,** 314 (2000).
[5] J. Lim, Y.-S. Park, V.I. Klimov, Optical Gain in Colloidal Quantum Dots Achieved by Direct-Current Charge Injection, Nature Mater. **17**, 42 (2018).

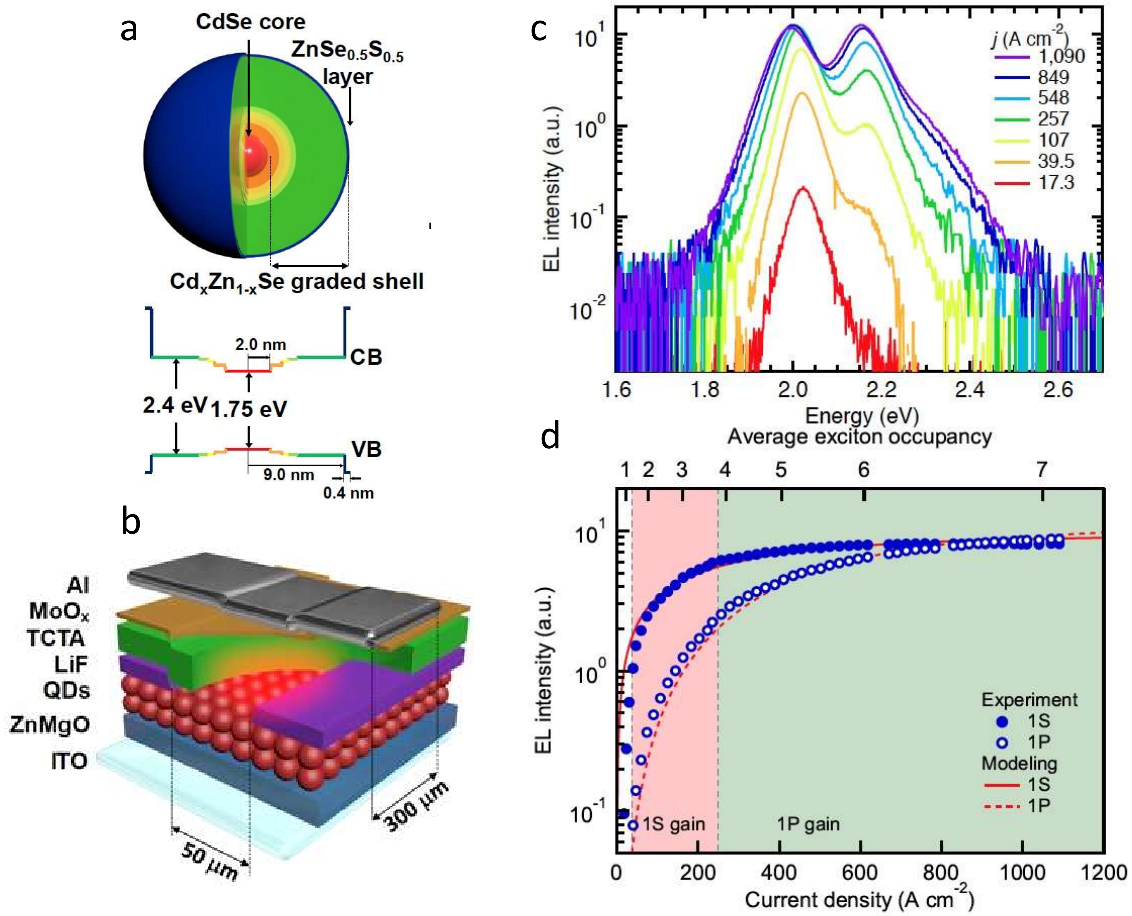

Fig.1: (a) The internal structure of the continuously graded QDs (cg-QDs) and the corresponding conduction- and valence-band (CB and VB, respectively) confinement potentials. (b) An LED device stack used in the present work. An emitting layer of cg-QDs is sandwiched between a ZnMgO electron transport layer and an organic (TCTA) hole transport layer, separated from the QDs by a current-focusing aperture (50-µm-wide slit) in a LiF interlayer. To enhance the current focusing effect, the Al anode is prepared as a 300-µm strip, oriented orthogonally to the slit. (c) The electroluminescence (EL) spectra of a current-focusing device under pulsed bias (τ_{pulse} = 1 µs) as a function of current density (j). (d) The 1S and 1P EL intensities (solid and open circles, respectively; determined from integrated areas) as a function of j inferred from the EL spectra in **c**. The lines are the calculations conducted using the 'correlated-injection' model of ref. [5]. The ranges of j that correspond to 1S and 1P optical gain (pink and green shadings, respectively) are determined based on the condition of achieving population inversion for the 1S and 1P transitions [5].

Controlling the parity and time-reversal symmetry of non-Hermitian graphene Dirac plasmons and its application to terahertz lasers

Taiichi Otsuji [1], Akira Satou [1], Hirokazu Fukidome [1], Maxim Ryzhii [2], Ryzhii Victor [1], and Koichi Narahara [3]

[1]*Tohoku University, Sendai, Miyagi 981-0908, Japan*

[2]*University of Aizu, Aizu-Wakamatsu, Fukushima 965-8580, Japan*

[3]*Kanagawa Inst. of Technology, Atsugi, Kanagawa 243-0292, Japan*

otsuji@riec.tohoku.ac.jp

Graphene has a unique electronic band structure that is linearly dispersed and gapless. As a result, both electrons and holes behave as relativistic charged particles of massless Dirac fermions. The quantum of plasma oscillation of these Dirac electrons is called the graphene Dirac plasmon, which can dramatically enhance the interaction of terahertz (THz) waves with graphene. We have proposed an original current-injection graphene THz laser transistor, demonstrated single-mode THz laser oscillation at low temperatures [1-3], and discovered and demonstrated the THz giant gain enhancement effect by graphene Dirac plasmons (Fig. 1) [4, 5]. However, in order to realize room temperature high intensity THz lasing and ultrafast modulation operation, which are necessary for the next generation wireless communication of 6G and 7G, further breakthroughs are needed. In this work, we introduce completely new physics and principles to simultaneously break through the limits of quantum efficiency and high-speed modulation operation by actively controlling the parity and time-reversal symmetry [6] of graphene Dirac plasmons with nanostructures and applied voltages (Fig. 2). In this talk, we will present new ideas on the operating principle and device structure of graphene plasmonic laser transistors (Figs. 3, 4) with high radiation intensity and ultrafast modulation capability operating at room temperature in the THz frequency band (Figs. 5, 6).

This work was supported by JSPS-KAKENHI No. 21H04546, and No. 20K20349, Japan.

[1] V. Ryzhii, M. Ryzhii, and T. Otsuji, J. Appl. Phys. **101**, 083114 (2007).

[2] T. Otsuji *et al.*, IEEE J. Sel. Top. Quantum Electron. **19**, 8400209 (2013).

[3] D. Yadav *et al.*, Nanophoton. **7**, 741-752 (2018).

[4] T. Watanabe *et al.*, New J. Phys. **15**, 075003 (2013).

[5] S. Boubanga-Tombet *et al.*, Phys. Rev. X **10**, 031004 (2020).

[6] M.-A. Miri, and A. Alu, Science **363**, eaar7709 (2019).

[7] Y. Koseki *et al.*, Phys. Rev. B **93**, 245408 (2016).

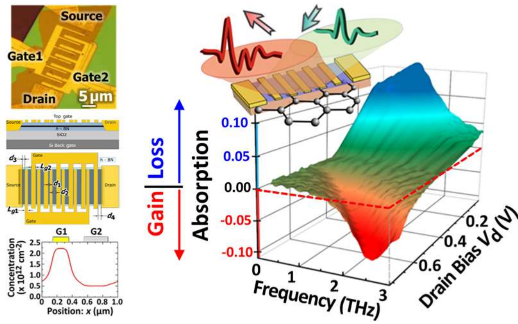

Fig.1: Experimental observation of room-temperature THz amplification in a current-driven graphene Dirac plasmon (GDP) laser transistor featured by a dual-grating-gate (DGG) structure under complementary biasing for the DGG [5].

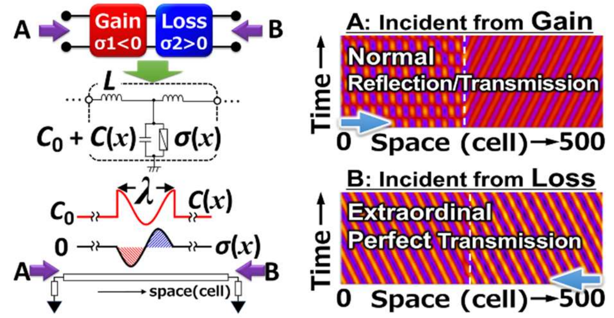

Fig.2: A toy model for a $\mathcal{PT}$ symmetric system in a distributed transmission line circuitry whose central core unit is given by the non-zero sinusoidal complementary gain-loss conductance element demonstrating anisotropic, extraordinary perfect transmission when radiation is incident from the loss port.

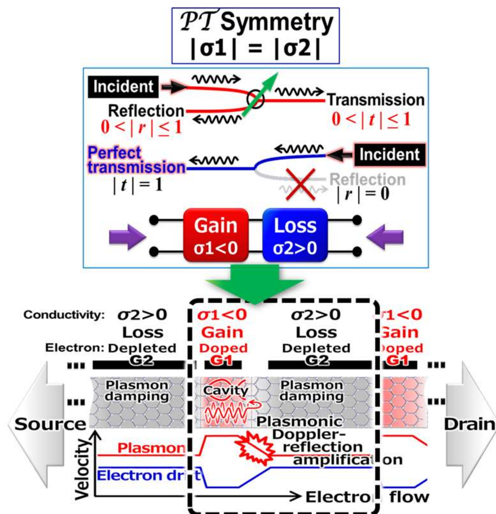

Fig.3: Implementation of the PT symmetry in the DGG-GDP metasurface.

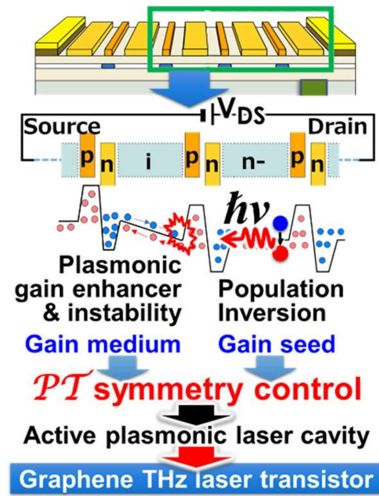

Fig.4: Controlling the PT symmetry of GDPs in a dual-grating-gate (DGG) graphene plasmonic terahertz laser transistor enabling high-speed, intense gain modulation. Conceptual device structure schematic.

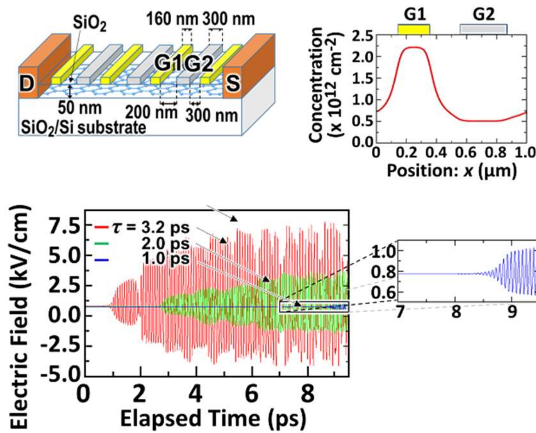

Fig.5: Nnumerically simulated time evolution of GDP field [7] activated by the dc-channel-current-driven PT symmetry turned on at t = 0 ps reaching the self-oscillation at the GDP mode frequency in a picosecond time scale. τ is the momentum relaxation time.

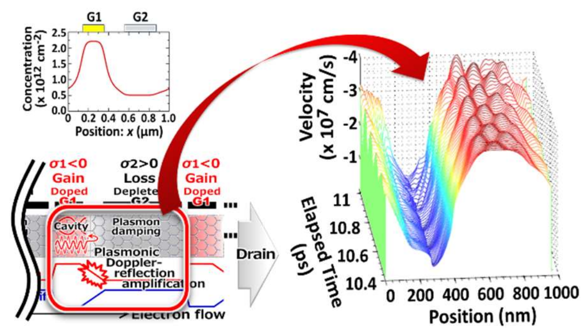

Fig.6: Numerically simulated, temporally evolved special distribution of the carrier velocity in the DGG metasurface under THz self-oscillation promoted by the current-driven GDP instability [7].

Topological defect dynamics in ultrafast energy efficient charge configuration memory devices.

A Mraz[1,4], R Venturini[1,3], M. Diego[1], A. Kranjec[1], D. Svetin[1,2], Y. Gerasimenko[1,2], J. Ravnik[1,5], I. Vaskivskyi[1,2], D. Kazazis[5], Y. Ekinci[5], R. Sobolewski and D. Mihailovic[1,2]

[1] *Jozef Stefan Institute, Dept. of Complex Matter, Jamova 39, SI-1000 Ljubljana, Slovenia*
[2] *CENN Nanocenter, Jamova 39, SI-1000 Ljubljana, Slovenia*
[3]*Faculty for Mathematics and Physics, University of Ljubljana, SI-1000 Ljubljana, Slovenia*
[4]*Faculty for Electrical Engineering, University of Ljubljana, SI-1000 Ljubljana, Slovenia*
[5]*LMN-Paul Scherrer institute, Villigen, Switzerland*
[7]*Department of Electrical and Computer Engineering and Physics and Astronomy, University of Rochester, New York, USA*
[8]*Brimrose Technology Corporation, Sparks, USA*
dragan.mihailovic@ijs.si

Energy efficiency and speed are two of the most important parameters in the search for new memory devices. Magnetic memory devices, which rely on metastability of magnetic domain orientation to store information need to convert information-carrying currents into magnetization, which has some fundamental limitations in this respect. Memristors, ferroelectric memory and phase change memory devices rely on crystal structural rearrangements, which can also be energetically costly. Recently, transition metal dichalcogenide charge-configuration memory (CCM) devices (Fig.1) have emerged as a record-breaking energy-efficient, ultrafast alternative (Fig.2) [1-6]. CCM devices introduce a new memory paradigm which relies on ultrafast and efficient manipulation of charge. However, some fundamental questions on their operation are still unresolved, which inhibits their widespread implementation and extended operational temperature range. Here we investigate the fundamental microscopic mechanisms leading to metastability in such devices. Using 4-probe scanning tunneling microscopy (STM) to control and manipulate charge during device operation (Fig.1) we microscopically follow the dislocation dynamics of the electronic crystal (Fig.3). The relaxation of metastable domain states within a single layer is seen to be hindered by topological defect dynamics, resulting in non-volatile memory switching between different charge configuration states with different intrinsic electrical resistance.

[1] M. Wang. *et al., Nat. Electron.* **1**, 582–588 (2018)

[4] L. Stojchevska, *et al,. Science* **344**, 177–180 (2014)

[5] I. Vaskivskyi, *et al., Nat. Commun.* **7**, 11442 (2016)

[6] D. Mihailovic, *et al*. APL **119**, 013106 (2021)

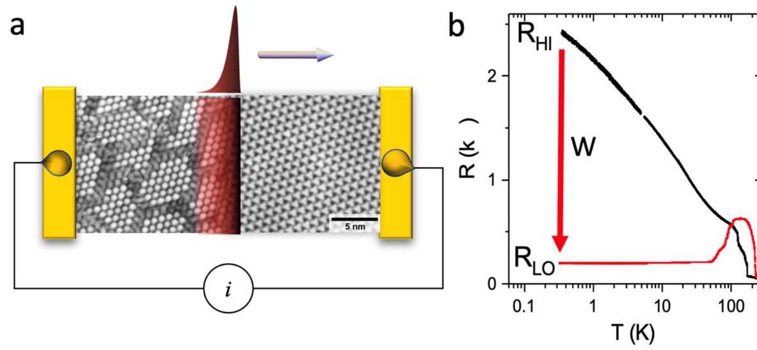

Fig.1: a) Schematic of the CCM device with pulse switching. b) Switching of resistance at low temperature by a single pulse. The graphs shows the cooling (black), switching (arrow) and heating cycles (red).

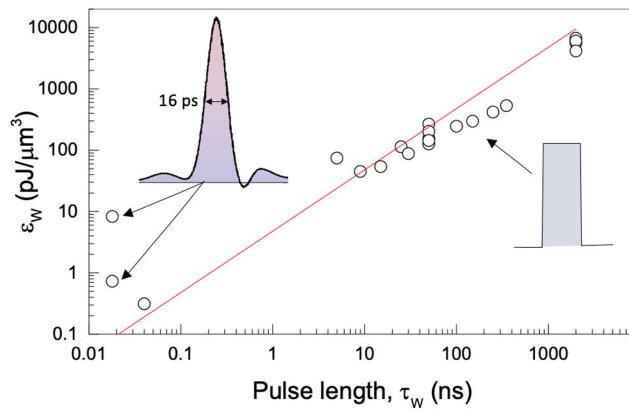

Fig.2: Energy density per bit as a function of pulse length at write (W) threshold for electrical pulse switching. The insert shows the pulse shapes for the short and long pulses.

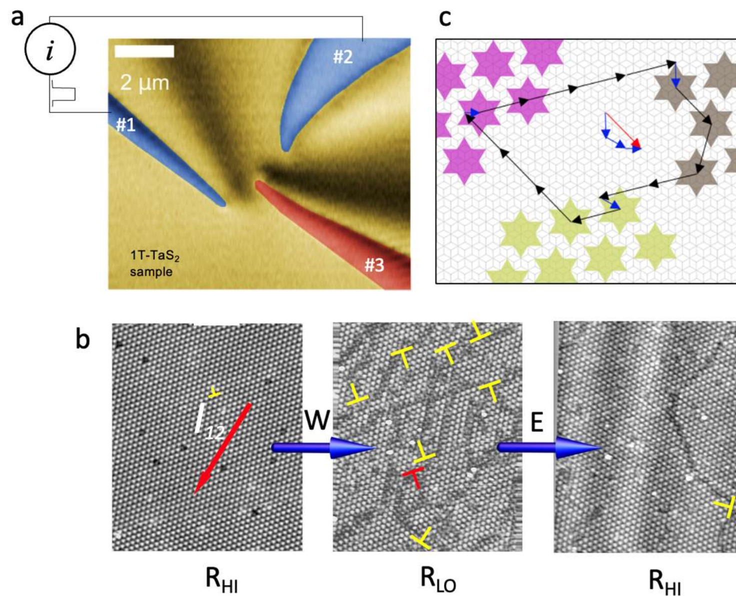

Fig.3: Domain and dislocation dynamics associated with CCM operation. a) three STM tips, b) Domain structure in HI and LO resistance states after W and E operations. Dislocations are indicated. C) the dislocation structure for one of the dislocations shown in the R_{LO} state in b).

Nanocryotron-driven Charge Configuration Memory devices

Anže Mraz[1,4], Rok Venturini[1,3], Damjan Svetin[1,2], Vitomir Sever[1], Ian A. Mihailovic[1], Jan Ravnik[1,5], Igor Vaskivskyi[1,2], Tevž Lotrič[1], Bor Brezec[1], Matic Merljak[1], Maria D'Antuono[6], Daniela Stornaiulo[6], Francesco Tafuri[6], Dimitrios Kazazis[5], Yasin Ekinci[5], Viktor. V. Kabanov[1] and Dragan Mihailovic[1,2]

[1]Jozef Stefan Institute, Dept. of Complex Matter, Jamova 39, SI-1000 Ljubljana, Slovenia

[2]CENN Nanocenter, Jamova 39, SI-1000 Ljubljana, Slovenia

[3]Faculty for Mathematics and Physics, University of Ljubljana, Jadranska 19, SI-1000 Ljubljana, Slovenia

[4]Faculty for Electrical Engineering, University of Ljubljana, Tržaška 25, SI-1000 Ljubljana, Slovenia

[5]LMN-Paul Scherrer institute, Villigen, Switzerland

[6]Dept. of Physics, University of Naples and CNR-SPIN, Naples, Italy

dragan.mihailovic@ijs.si

For some time, cryo-computing has been severely limited by the absence of a suitable fast and energy efficient low-temperature memory[1,2]. Ideally, such memory should be compatible with single-flux quantum (SFQ) logic in terms of speed, switching energy and matching impedance. Here we present an implementation of non-volatile charge configuration memory (CCM)[3,4] in a cryo-computing environment with a hybrid device incorporating a superconducting nanowire cryotron (nTron)[5]. The dynamical response of the device is modeled in terms of the superconducting order parameter in a confined channel of a current-controlled nanowire with a CCM shunt[6]. Analysis of time-dynamics and current-voltage characteristics based on measured device parameters show that single flux quantum (SFQ)-level pulses can drive non-volatile CCM on the picosecond timescale, while allowing the nTron to operate in non-latching mode. The inherent high energy efficiency and ultrahigh speed makes this hybrid device an ideal memory for use in cryo-computing and quantum computing peripheral devices.

[1] Q.-Y. Zhao, *et al.* Superconductor Science and Technology **31**, 035009 (2018).

[2] D.S.Holmes *et al*, IEEE Trans. Appl. Supercond. **23**, 1701610–1701610 (2013).

[3] I. Vaskivskyi *et al. Nat. Comm.* **7**, 11442 (2016).

[4] D. Mihailovic *et al.*, *APL* **119**, 013106 (2021).

[5] A.N. McCaughan, & K.K. Berggren, A *Nano Letters* **14**, 5748–5753 (2014).

[6] M.W.Brenner,*et al*., *Phys. Rev.* B **85**, 224507 (2012).

Sub-2-picosecond, sub-2 fJ/bit resistance switching between charge ordered phases with a single picosecond electrical pulse

R. Venturini[1,3], A. Mraz[1,4], I. Vaskivskyi[1], D. Svetin[1,2], S. B. Trivedi[6], J. Cheng[5], R. Sobolewski[5], and D. Mihailovic[1,2]

[1] Jozef Stefan Institute, Dept. of Complex Matter, Jamova 39, SI-1000 Ljubljana, Slovenia
[2] CENN Nanocenter, Jamova 39, SI-1000 Ljubljana, Slovenia
[3]Faculty for Mathematics and Physics, University of Ljubljana, SI-1000 Ljubljana, Slovenia
[4]Faculty for Electrical Engineering, University of Ljubljana, SI-1000 Ljubljana, Slovenia
[5]Department of Electrical and Computer Engineering and Physics and Astronomy, University of Rochester, New York, USA
[6]Brimrose Technology Corporation, Sparks, USA
dragan.mihailovic@ijs.si

We present measurements of ultrafast switching of charge configuration memory (CCM) devices using optically generated electrical pulses. The CCM device is based on switching between different charge-density wave states with different intrinsic electrical resistance [1-4]. A transmission line circuit, in combination with a $Cd_{0.55}Mn_{0.45}Te$ (CMT) substrate crystal, allows us to measure short pulse propagation through the memory device, with sub-100fs accuracy using electro-optic sampling (Fig. 1). We find that a single 1.9 ps electrical pulse is sufficient to switch the device from a high resistance state to a low resistance state (Fig. 2). As a result of the short pulse length, the switching energy is very small, giving an extremely small switching energy density at threshold of 0.022 pJ/ μm^3. The device switching energy in the presented example is ~8fJ/bit.

[1] L. Stojchevska, *et al. Science* **344**, 177–180 (2014).
[2] I. Vaskivskyi, *et al. Nat. Commun.* **7**, 11442 (2016).
[3] J. Ravnik, *et al., Phys. Rev. B* **97**, 075304 (2018).
[4] D. Mihailovic, *et al*. APL 119, 013106 (2021).

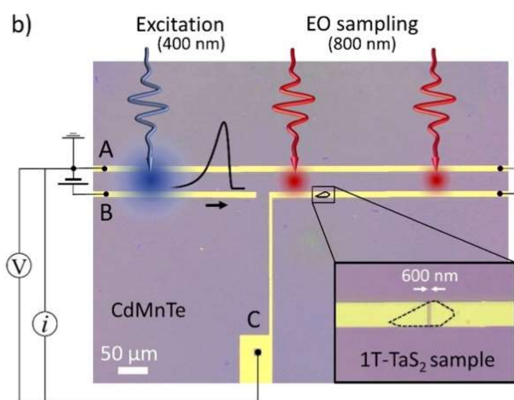

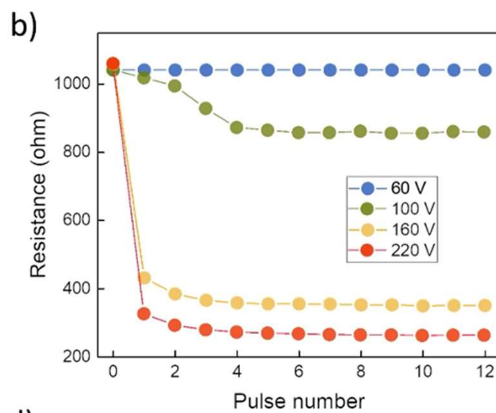

Fig.1: The trap is connected to electrodes with the rates Γ_N and $\Gamma_\pm$. A magnetic field ***B*** *defines the trap spin quantization axis OZ' at an angle Θ to the magnetization orientation OZ in the ferromagnet.*

Fig.2: Current as a function of Θ, for p=1, $\Gamma_N/\Gamma_F = 10$, $\omega_L/\Gamma_F = 1$, $\Gamma_F T_1 = 10$, and several values of T_2/T_1.

Rapid, multianalyte detection of opioid metabolites in wastewater

Narendra Kumar[1], Michael Geiwitz[1], Muhit Rana[2], Niazul Islam Khan[2], Matt Catalano[1], Juan C. Ortiz-Marquez[3], Hikari Kitadai [4], Andrew Weber[2], Badawi Dweik[2], Xi Ling[4,5,6], Tim van Opijnen[3], Avni Argun[2], Kenneth S. Burch[1*]

[1]Department of Physics, [3]Department of Biology, Boston College, Chestnut Hill, MA, USA

[2]Giner Inc., Newton, MA, USA

[4]Department of Chemistry, [5]Division of Materials Science and Engineering, [6]The Photonics Center, Boston University, Boston, MA, USA

[*]Email: ks.burch@bc.edu

By monitoring opioid metabolites, wastewater-based epidemiology (WBE) could be an excellent tool for real-time information on consumption of illicit drugs. [1] A key limitation of WBE is the reliance on costly laboratory-based techniques that require substantial infrastructure and trained personnel, resulting in long turnaround times. In the last decade, graphene field effect transistor (G-FET) based biosensors have emerged as sensors with a large potential due to their rapid detection, high sensitivity, biocompatibility, non-covalent functionalization, and scalable fabrication on various substrates. [2-5] Here, we present an aptamer-based nanoelectronic platform (AptG-FET) for simultaneous detection of three different opioid metabolites (Figure 1). This platform provides a reliable, rapid, and inexpensive method for quantitative analysis of opioid metabolites in wastewater (WW). The platform delivers a limit of detection (LOD) 2-3 orders of magnitude lower than previous reports, but in line with the concentrations range (pg/ml to ng/ml) of these opioid metabolites present in real samples. To enable multianalyte detection we developed a facile, reproducible, and high yield fabrication process producing twenty G-FETs with integrated side gate platinum (Pt) electrodes on a single chip (Figure 1). Our devices achieved the simultaneous and selective multianalyte detection of three different metabolites: Noroxycodone (NX), 2-ethylidene-1,5-dimethyl-3,3-diphenylpyrrolidine (EDDP), and Norfentanyl (NF) in wastewater with their respective LOD values of 126 pM (38 pg/ml), 96 pM (27 pg/ml), and 183 pM (42 pg/ml).

[1] T. Gunnar et. al., Current Opinion in Environmental Science & Health 2019, 9, 49–57.

[2] N. Kumar et.al., Medical Devices and Sensors 2020, 3, 6, e10121.

[3] N. Kumar et.al., *Biosensors and Bioelectronics* **2020**, *156,* 112123.

[4] N. Gao et. al., PNAS **2016**, *113* (51), 14633–14638.

[5] J. Ping et. al., *ACS Nano* **2016**, *10* (9), 8700–8704

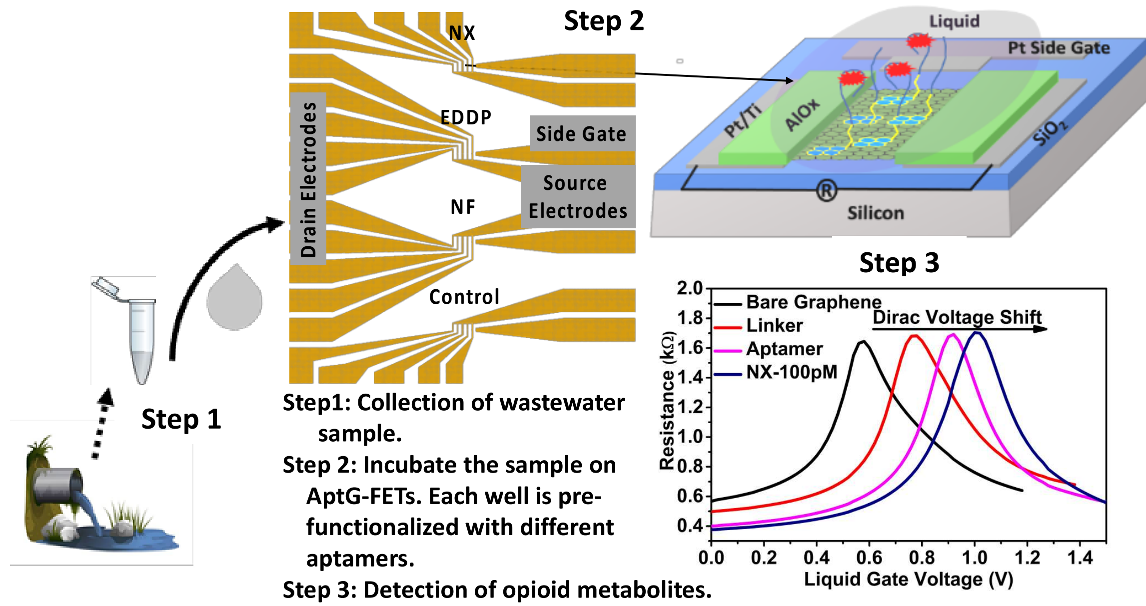

Figure 1. *Schematic illustration of an onsite chip-based rapid detection platform for near real-time monitoring of opioid metabolites in wastewater using AptG-FET sensor technology. Step 1, wastewater collection, filtration, and dilution (as needed); Step 2, on chip sample (10 μL) incubation; Step 3, sensor characterization of the sensor to estimate the concentration of targeted drug metabolites.*

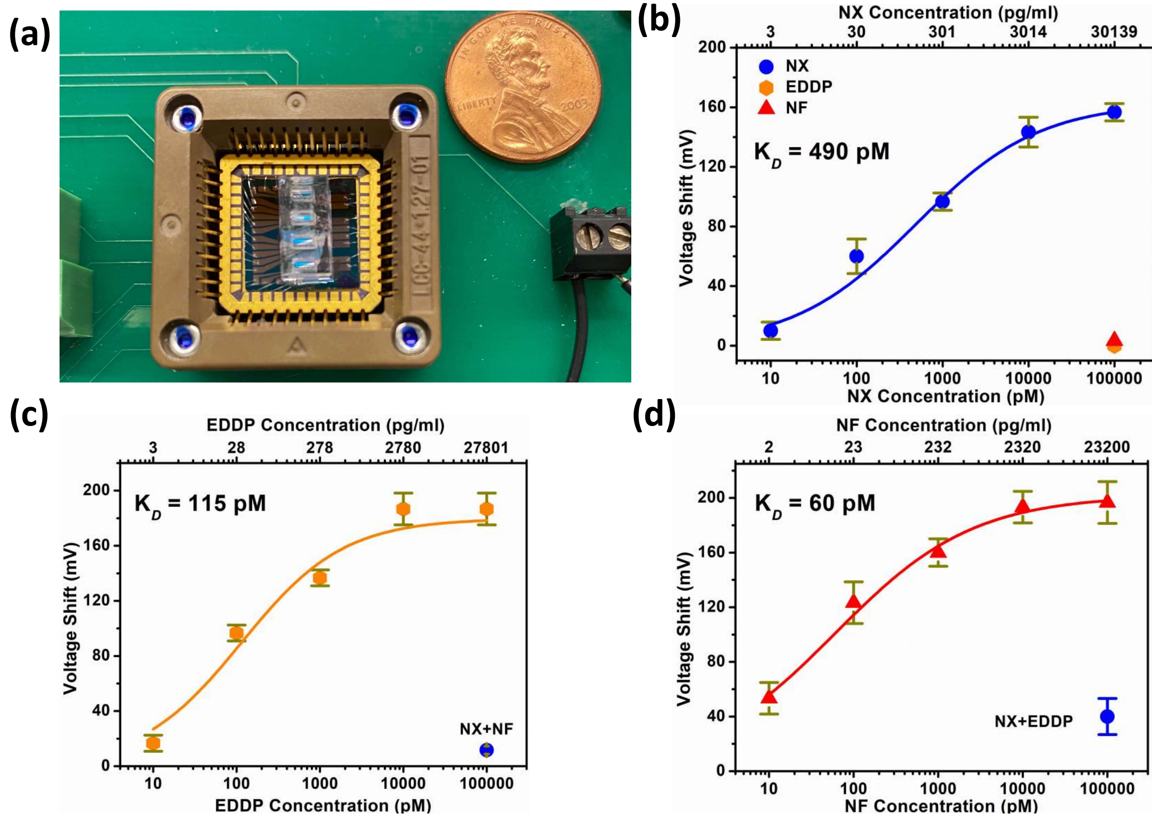

Figure 4 *(a) G-FET chip with 4 PDMS wells (b) Calibration curve for NX in wastewater with negative control of EDDP and NF, K_D value of 490 pM and LOD of 126 pM (c) Calibration curve for EDDP with negative controls of NX and NF, K_D value of 115 pM and LOD of 96 pM (d) Calibration curve for NF with negative controls of NX and EDDP, K_D value of 60 pM and LOD of 183 pM. Error bars were calculated with the data from 5 devices at each concentration.*

NEMS Devices to Enable Adiabatic Reversible Computing

R. Celis-Cordova, A. F. Brown, J. J. Gose, A. O. Orlov, and G. L. Snider
Dept of Electrical Engineering, University of Notre Dame, Notre Dame, USA
rcelisco@nd.edu

As we approach the end of Moore's law, beyond-CMOS devices are needed to implement low power computing, and nano-electromechanical devices (NEMS) can enable ultra-low energy computing in the form of adiabatic reversible computing. Adiabatic reversible computing is a promising approach to energy efficient computing that can dramatically reduce heat dissipation by switching circuits slowly, relative to their RC time constants, introducing a trade-off between energy and speed. However, energy savings using CMOS circuits are ultimately limited by leakage since transistors do not turn completely off. NEMS relays have been explored as alternative devices to eliminate leakage but are limited by the degradation of current-carrying contacts [1]. This work presents an implementation of adiabatic reversible computing using NEMS gap-closing variable capacitors that do not need make and break electrical contacts. The NEMS devices consist of a suspended highly-doped polysilicon cantilever and bottom TiN electrodes that form two separate capacitors, as seen in Fig. 1. The cantilever moves under an applied voltage V_{in}, changing its capacitance C_{SD}, and can be used to create digital gates in conjunction with a static capacitor C_L as shown in Fig. 2, in what is known as adiabatic capacitive logic [2]. The devices were fabricated on silicon wafers coated with silicon nitride as a base insulator as shown in Fig. 3. A sacrificial layer of silicon dioxide was used to separate the capacitor electrodes, and it was removed with a wet HF etch, followed by critical point-drying to prevent stiction problems. The cross section of the suspended cantilever is shown in Fig. 4. SPICE simulations were performed to demonstrate that the NEMS variable capacitors can create a digital inverter as presented in Fig. 5. The results of the SPICE simulations are shown in Fig. 6. Here, a ramping clock V_{CLK} is connected to a variable capacitor C_S that changes from 2.8 fF to 25 fF, and a static 11.2 fF capacitor C_L to form a capacitive divider that can be cascaded to create multiple stages. The output voltage is given by:

$$V_{Out} = \frac{C_S(V_{in})}{C_S(V_{in}) + C_L} V_{CLK}$$

The variable capacitors represent the first experimental demonstration of gap-closing NEMS devices that can enable adiabatic reversible computing not restricted by leakage. This work was supported by the US National Science Foundation under grant NSF ECCS-1914061.

[1] S. Rana *et al.*, Nature Comm **11**, 1181 (2020).
[2] H. Samaali *et al.*, Nano Energy **55**, 277-287 (2019).

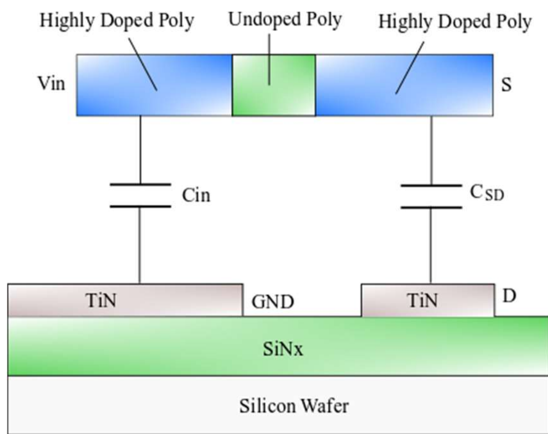

Fig.1: NEM variable capacitor for adiabatic reversible computing using highly doped polysilicon and Titanium Nitride electrodes.

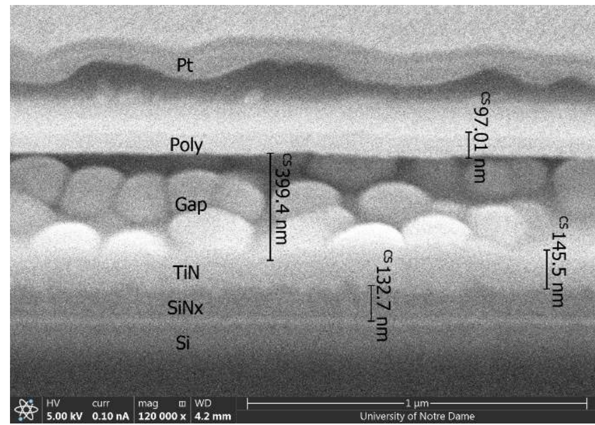

Fig.4: SEM micrograph showing cross section of NEM variable capacitor. The suspended poly cantilever is separated from the bottom TiN electrodes by a 400nm gap.

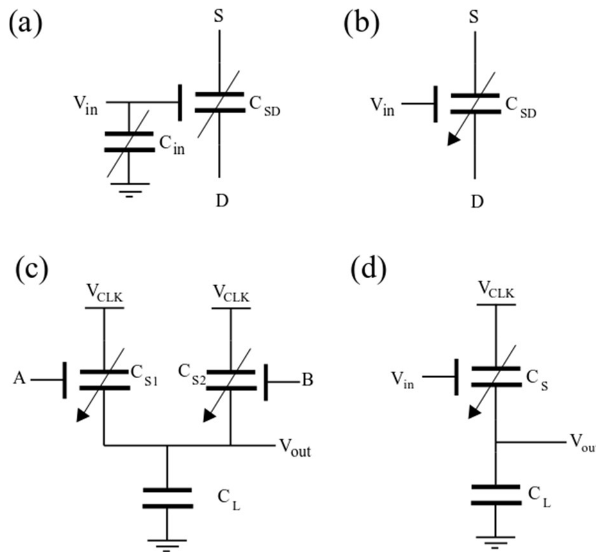

Fig.2: (a) Variable capacitor logic diagram. (b) Simplified diagram for variable capacitor. (c) NAND gate. (d) Inverter gate.

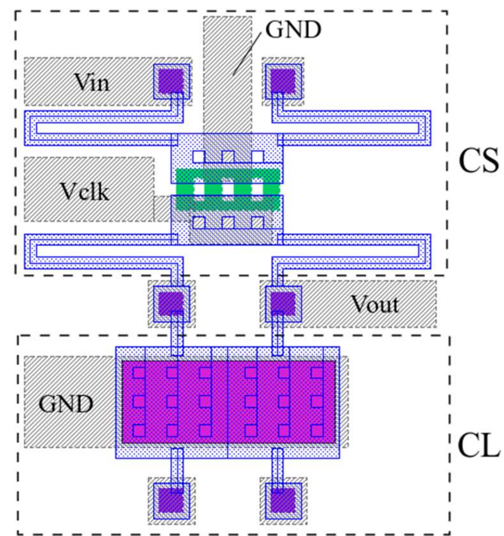

Fig.5 Physical design of inverter gate for adiabatic reversible computing using gap-closing variable capacitors.

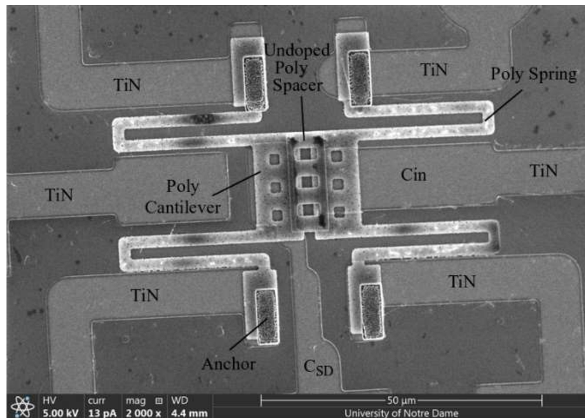

Fig.3: SEM micrograph showing top view of NEM device fabricated on a silicon wafer coated with SiNx. The poly cantilever is suspended using springs and separated by an undoped poly spacer.

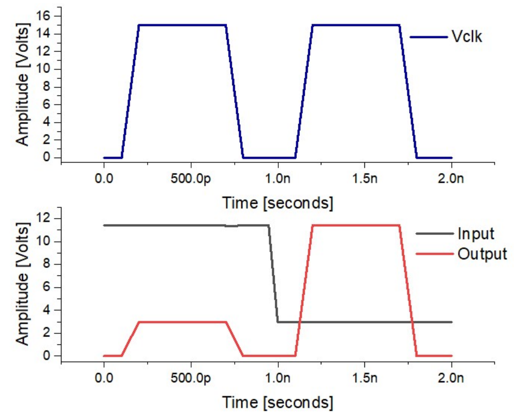

Fig.6: SPICE simulation of inverter gate for reversible computing with a static capacitor of 11.2 fF, and a NEM variable capacitor changing from 2.8 fF to 25 fF.

"Wiring-Up" Atom-Defined Device Elements: Ever Closer to Operational Ultra-Fast, Ultra-Low Power Circuits

R.Wolkow[1,2] , J.Pitters[2], J. Onada[1,2], A.Khademi[1,2], T.Chutora[1], C.Leon[1], F.Altincicek[1], J.Croshaw[1], L.Livadaru[1], M.Salomons[2], M.Cloutier[2], M.Yuan[1], R.Achal[1], S.Yong[1], S.Bukhari[1,2]

[1]*Department of Physics, University of Alberta, Edmonton, Alberta, Canada*

[2]*National Research Council of Canada Nanotechnology Research Centre*

Most all atom-defined structures that have been built to date have been held together by extremely weak bonds and are therefore unstable at room temperature. Moreover, most systems of study have been fabricated on metal substrates that entirely mask any interesting electronic properties of atomic (or molecular) assemblies.

Patterned atomic dangling bonds on an otherwise Hydrogen-terminated silicon surface are robust and unchanging to over 200 C and offer useful electronic properties. This area was pioneered largely by Joseph Lyding more than 2 decades ago.

Many (many!) challenges stood in the way of tests and applications in this area. Over the last 20 years we have doggedly pursued and overcome innumerable fabrication and measurement issues related to dangling bonds and as well have come to greatly advance understanding of the relations among dangling bonds and of those with bulk silicon. Crucially, we recognize and utilize the gap-state character of dangling bond structures to make 2D surface circuits that are isolated from the bulk – or if desired – connected with spatial and temporal control. Operation of binary atomic silicon logic gates and a binary wire have been demonstrated. These are derived from earlier, non-atomic, field-controlled computing ideas developed by Lent, Snider, Porod and others at Notre Dame. Our atomic building blocks retain fast, low power qualities while removing a cryogenic operation requirement and while also providing unprecedented variance-free devices.

In this talk I will show new results including fabrication and multi-spm-probe characterization of nm-scale silicon wires that are intimately bonded to yet electrically isolated from normal bulk Si. Atom-defined wires and their quantized states will be shown. Also atomic lines that can be switched from covalent to ionic bonding will be shown. Distinct ½ and 3/2 spin-orbit coupled angular momentum states existing at Boron dopants will be shown. Atomic wire coupling – perhaps even a "read-out" of atomic dopant will be presented. Qubit, magnetometry, quantum metrology ideas flowing from this might be sketched also.

978-3-9504738-3-4

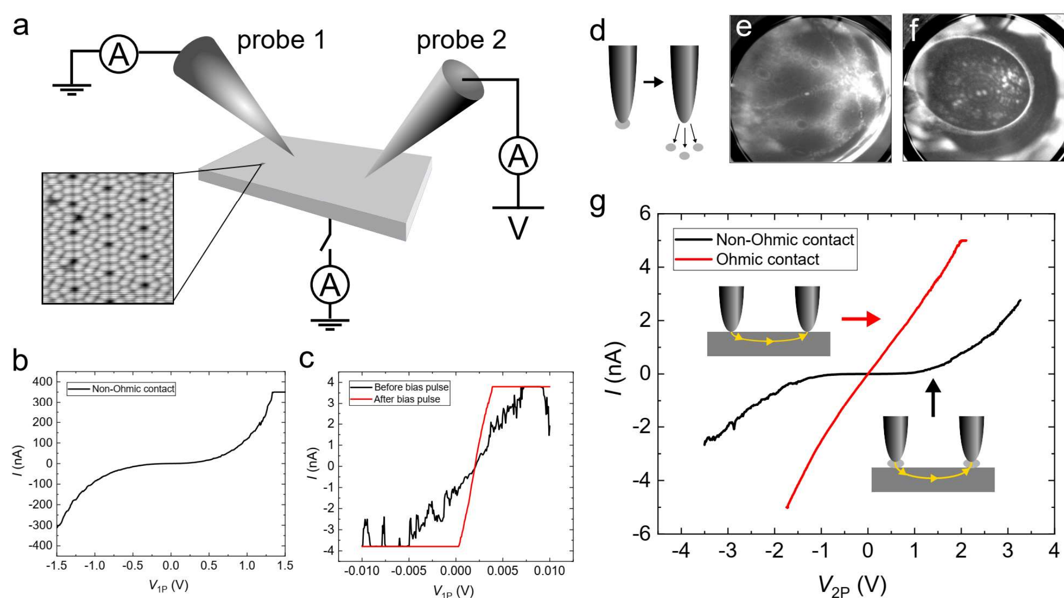

Fig.1: Ohmic and non-Ohmic contacts in conductance measurements. (a) Experimental setup of conductance measurements with 2P-STM. Typical STM image of the Si(111)-(7×7) surface is also shown. (b) I-V curve obtained by 1P-STM with a non-Ohmic contact. (c) I-V curves measured by 1P-STM with a Ohmic contact before and after the controlled bias voltage pulses. (d) Cleaning of a tip apex by field evaporation. (e) FIM image of a W tip after cleaning by field evaporation. Tip bias voltage is 17.0 kV. (f) FIM image of the W tip sharpened by field-assisted O2 etching. Tip bias voltage is 7.8 kV. (g) I-V curves measured by 2P-STM with Ohmic and non-Ohmic contacts..

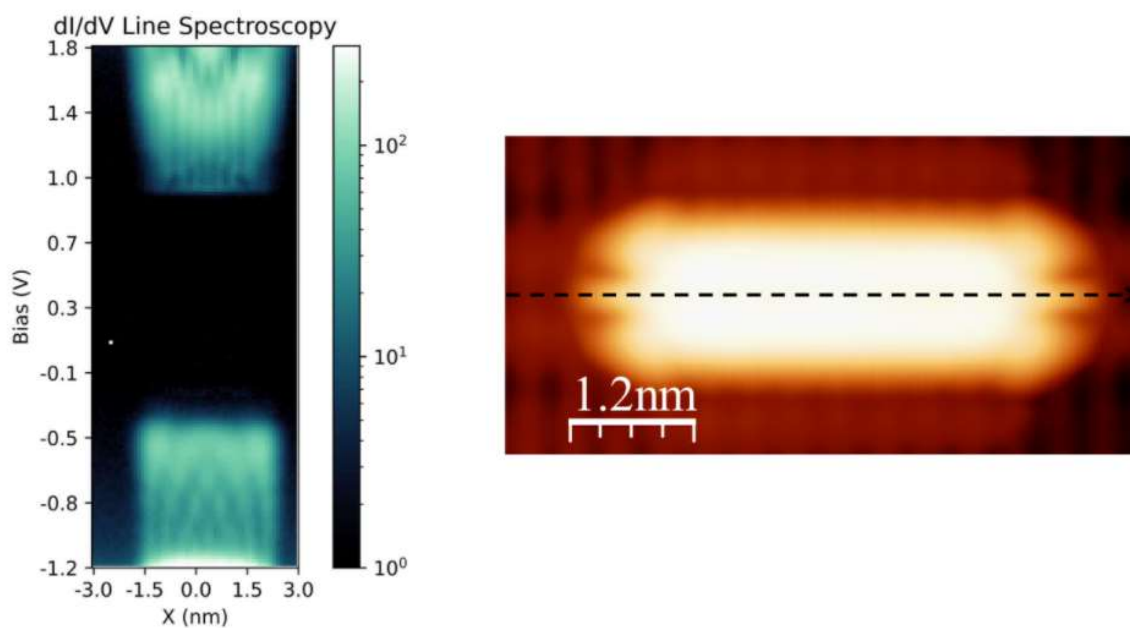

Fig.2: Density of states (actually DI/DV map) of a 12 atom line. Dispersive character of states is evident..

TCAD Simulation of Novel Semiconductor Devices with NESS

A. Asenov[1,2]
[1]*Scholl of Engineering, Glasgow University, Rankine Building, Glasgow*
[2]*Semiwise Ltd.*

T Simulation of conventional and emerging electronic devices using Technology Computer Aided Design (TCAD) tools has been an essential part of the semiconductor industry as well as academic research. Computational efficiency and accuracy of the numerical modeling are the key criteria on which quality and usefulness of a TCAD tool are ascertained. Further, the ability of the tools to incorporate different modeling paradigms and to be applicable to a wide range of device architectures and operating conditions is essential. In this paper, we provide an overview of the new device simulator NESS (Nano-Electronic Software Simulator) developed at the University of Glasgow's Device Modelling Group. It is a fast and modular TCAD tool with flexible architecture and structure generation capabilities, and contains different modules including classical, semi-classical, and quantum transport solvers, mobility calculation, kinetic Monte-Carlo and others. NESS can also take into account various sources of statistical variability in nanodevices and can perform simulations of thousands of microscopically different devices created by the structure generator. This state-of-the-art tool is design to be open source environment and being made available to the device engineering community at large for active collaboration and development.

[1] NESS. [http://web.eng.gla.ac.uk/groups/devmod/index.php/software/]
[2] S. Berrada *et al.*, Proc. *SISPAD*, Sep. 2018, pp. 22–25.
[3] S. Berrada *et al.*, *J. of Comput. Electron.*, vol. 19, pp. 1031–1046, 2020.
[4] C. Medina-Bailon *et al.*, *J. of Microelectronic Manufacturing*, vol. 3, pp. 20030404, 2020.
[5] C. Medina-Bailon *et al.*, *Micromachines*, vol. 12, no. 6, pp. 680, 2021.
[6] O. Badami *et al.*, *Applied Sciences*, vol. 9, no. 9, p. 1895, 2019.
[8] T. Dutta *et al.*, *14th IEEE NMDC conf*, 2019, pp. 1–4.
[10] M. Luisier *et al.*, *Phys. Rev. B*, vol. 80, p. 155430, Oct 2009.
[11] T. Sadi *et al.*, *Materials*, vol. 12, no. 1, p. 124, 2019.
[12] C. Medina-Bailon *et al.*, *IEEE Elect Deve Letters*, vol. 40, no. 10, pp. 1571 – 1574, 2019.
[13] P. Lapham *et al.*, *Proc SISPAD*, 2020, pp. 273–276.
[14] J. Ding *et al.*, "*Semiconductor Science and Technology*, vol. 36, no. 7, pp. 075021, jun 2021.
[15] C. Medina-Bailon *et al.*, *Proc. SISPAD*, 2020, pp. 293–296.

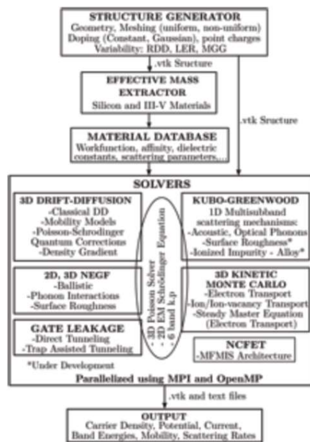

Fig.1: NESS in a nutshell: Flowchart showing different modules and how they are linked.

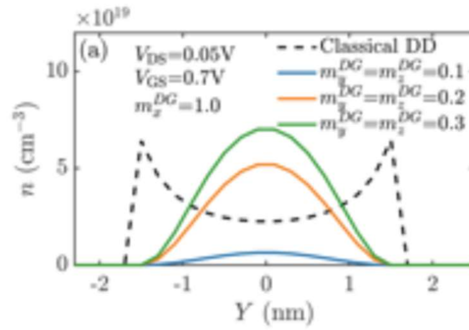

Fig.4: Quantum corrections introduced in the drift/diffusion module of NESS.

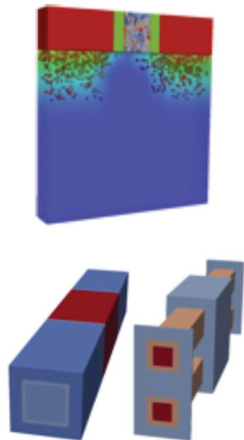

Fig.2: Examples of different device structures generated using the SG module: (a) Bulk MOSFET with variability effects introduced (b) Single NWFET, (c) Stacked NWFET.

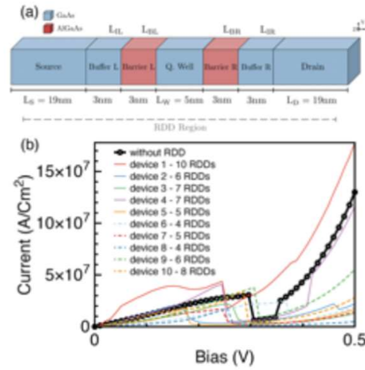

Fig.5 RTD simulation using the NEGF module of NESS

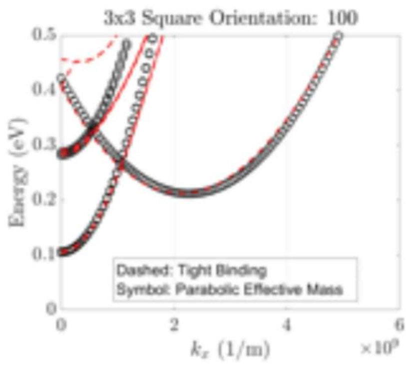

Fig.3: Comparison of the electronic band structure calculated using tight binding and the Parabolic Effective Mass approximation using the EME module in NESS

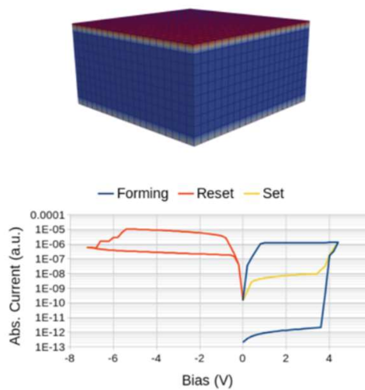

Fig.6:RRAM simulation using the kinetic Monte Carlo Module in NESSt.

978-3-9504738-3-4

Electron Quantum Optics for Quantum Interference Logic Devices

Josef Weinbub[1], Mauro Ballicchia[2], and Mihail Nedjalkov[2]
[1]Christian Doppler Laboratory for High Performance TCAD at the
[2]Institute for Microelectronics, TU Wien, Austria
josef.weinbub@tuwien.ac.at

Electron quantum optics provides the basis for conducting quantum optics-like investigations in a fermionic picture by treating electrons as waves [1-3]. Compared to quantum optics, solid state electron approaches have the advantage in terms of size, scalability, and the ability of the charge degree of freedom to be easily measurable, with the drawback of a much shorter coherence time. By using numerical simulations based on a Wigner function approach [3,4], this work shows how electron quantum optics principles can be used to realize an electron quantum interference logic device (eQILD) [5], Fig. 1. Our design constitutes an alternative for non-magnetic, low-power, and high performance logic devices allowing for co-integration with conventional electronics. An eQILD is based on injecting individual electron waves into a two-dimensional wave guide which, on the output side, provides three channels. The entire wave guide is sandwiched between two insulating layers, where the top insulator contains two controlling gates which, depending on their biases, allow to change the potential profile affecting the subjacent evolving electron waves. The thus changeable potential landscape leads to specific interference maxima in the electron density, Fig. 2-3, leading to different output currents. The emerging current levels enable to define logic gates. In particular, universal NAND and NOR gates can be defined, Fig. 4. The results show that it is only due to the quantum effects in the transport that these distinct current levels materialize: Loosing the coherence would result in reduced current level differences, consequently loosing stable logic gate definitions. The switching performance of an eQILD entirely depends on the injection performance, e.g., a single-electron source (~10 GHz). The here shown eQILD design provides several directions for adaptations, e.g., number and geometry of the output channels and gates, different wave guide materials, and multi-valued or reconfigurable logic.

[1] C. Bäuerle *et al.*, Rep. Prog. Phys. **81**, 056503 (2018).
[2] L.A. Clark *et al.*, New J. Phys. **22**, 103031 (2020).
[3] J. Weinbub *et al.*, J. Phys. Cond. Matt. (2021), under review.
[4] J. Weinbub *et al.*, Appl. Phys. Rev. **5**, 041104 (2018).
[5] J. Weinbub *et al.*, Res. Square (2021), under review.

Acknowledgment. The financial support by the Austrian Science Fund (FWF): P33609, the Austrian Federal Ministry for Digital and Economic Affairs, the National Foundation for Research, Technology and Development and the Christian Doppler Research Association is gratefully acknowledged.

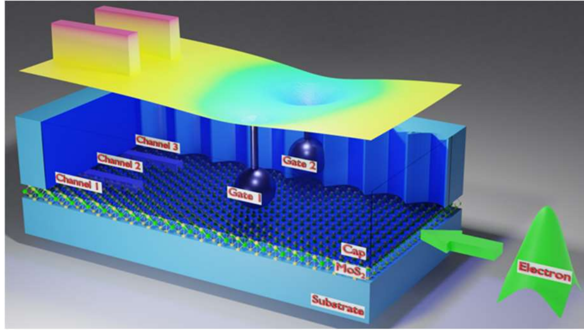

Fig.1: Schematic representation of an eQILD. An exemplary potential energy distribution of the wave guide is shown on top. The blue cap layer is partially made transparent to show the inside of the device.

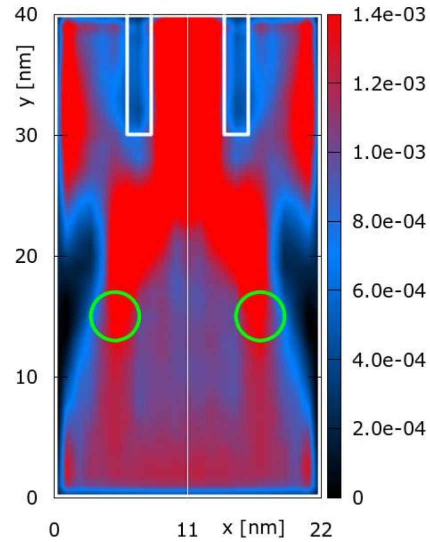

Fig.2: Distribution of quantum electron density [a.u.] for two symmetric, positive gate bias configurations (green circles). The output channel walls are shown in white.

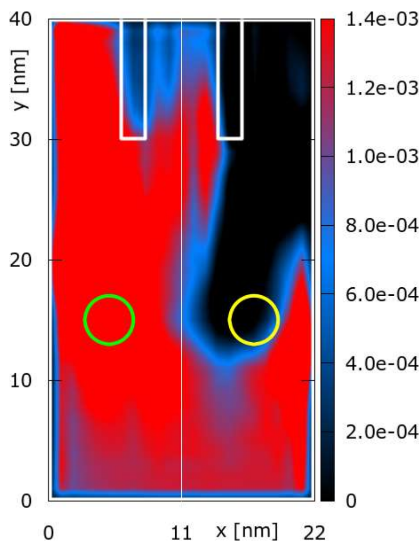

Fig.3: Distribution of quantum electron density [a.u.] for two asymmetric gate bias configurations (green circle positive, yellow circle negative).

ϕ_{G_1}	ϕ_{G_2}	I_{C_1}	I_{C_2}	I_{C_3}	GATE
-0.21	-0.21	9	10	9	NOR: 1 1 → 0
-0.21	-0.105	10	14	28	
-0.21	0	13	15	36	NOR: 1 0 → 0
-0.21	0.105	16	13	37	
-0.21	0.21	15	14	32	
-0.105	-0.21	28	14	10	
-0.105	-0.105	19	31	19	NAND: 0 0 → 1
-0.105	0	17	11	47	
-0.105	0.105	18	13	39	NAND: 0 1 → 1
-0.105	0.21	16	16	24	
0	-0.21	36	15	13	NOR: 0 1 → 0
0	-0.105	47	11	17	
0	0	26	27	26	NOR: 0 0 → 1
0	0.105	17	13	47	
0	0.21	14	20	34	
0.105	-0.21	37	13	16	
0.105	-0.105	39	13	18	NAND: 1 0 → 1
0.105	0	47	13	17	
0.105	0.105	15	46	15	NAND: 1 1 → 0
0.105	0.21	10	20	40	
0.21	-0.21	32	14	15	
0.21	-0.105	24	16	16	
0.21	0	34	20	14	
0.21	0.105	40	20	10	
0.21	0.21	15	41	15	

Fig.4: Output channel currents for different gate bias configurations. The GATE column shows truth table entries for the NAND and NOR gate. Framed current values indicate the utilized channel to realize the logic.

Novel Topological Kink States with Spin-Valley-Momentum Locking

Tong Zhou[1,*], Shuguang Cheng[2], Michael Schleenvoigt[3], Peter Schüffelgen[3], Hua Jiang[4], Zhongqin Yang[5] and Igor Žutić[1]

[1]*Department of Physics, University at Buffalo, State University of New York, Buffalo, USA*

[2]*Department of Physics, Northwest University, China*

[3]*Peter Grünberg Institute 9, Forschungszentrum Jülich, Germany*

[4]*School of Physical Science and Technology, Soochow University, China*

[5]*Department of Physics, Fudan University, China*

**e-mail: tzhou8@buffalo.edu*

2D topological insulators offer a tantalizing prospect that their edge states are spin-momentum locked, supporting the quantum spin Hall (QSH) effect. However, such QSH states are usually fragile or limited to cryogenic temperatures, which can be easily destroyed by magnetic impurities [1]. A similar situation arises in quantum valley Hall (QVH) insulators, where the resulting valley-momentum locking unlocks easily with short-range impurities and the conductance quantization disappears [2]. To overcome these challenges, we propose a planar junction formed by the QSH and QVH insulators, where the QSH and QVH states can simultaneously emerge along their interface, giving a novel quantum spin-valley Hall kink (QSVHK) states [3]. Unlike the single QSH (QVH) states, such QSVHK states are robust against different (magnetic) disturbances and imperfections, showing ballistic spin-valley-momentum locking transport even at room temperature [3]. Based on first-principles results and our fabricated samples, we show how the QSVHK states can be realized by the gate control, alloy engineering, or surface functionalization in bismuthene [3]. We further reveal how the interplay between the QSH (QVH) and quantum anomalous Hall states can generate multiple Hall effects through the electric or magnetic control [4-6], where their band topology can be optically probed [7]. Such multiple Hall effects are highly tunable and feasibly realized, paving an important step towards topological spintronics and valleytronics.

[1] X.-L. Qi and S.-C. Zhang, Rev. Mod. Phys. **83**, 1057 (2011).
[2] J. Li et al., Nat. Nanotechnol. **11**, 1060 (2016).
[3] T. Zhou et al., Phys, Rev. Lett. **127**, 116402 (2021).
[4] T. Zhou et al., npj Quant. Mater. **3**, 39 (2018).
[5] T. Zhou et al., Phys, Rev. B **94**, 235449 (2016).
[6] T. Zhou et al., Nano Lett. **15**, 5149 (2015).
[7] G. Xu, T. Zhou et al., Phys. Rev. Lett. **125**, 157402 (2020).

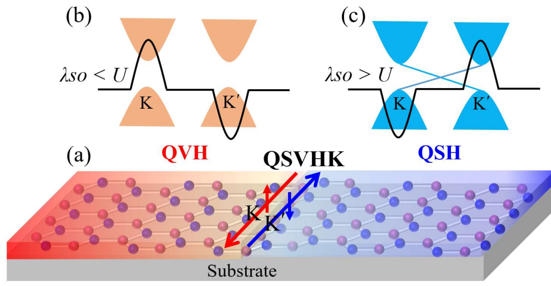

Fig.1: (a) Schematic of the QSVHK states in a junction formed by QVH and QSH insulators. (b), (c) Schematic bands and Berry curvatures (black lines) for QVH and QSH insulators, distinguished by the relative strength of the SOC, λ_{SO}, and staggered potential, U.

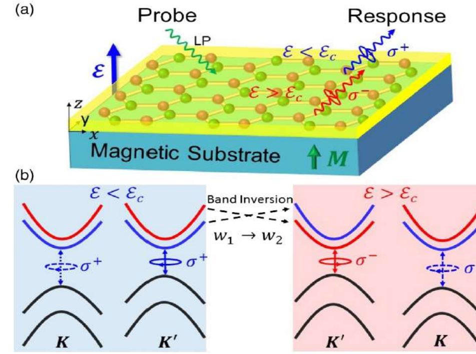

Fig.4: (a) Schematic setup. The linearly polarized (LP) probe light yields a response of definite helicity, $\sigma^{\pm}$, that depends on the electric field, ε. (b) Bands at the K/K' valleys. The K'-valley conduction band ordering and the winding numbers, $w_{1,2}$, change when ε exceeds a critical value, ε_c.

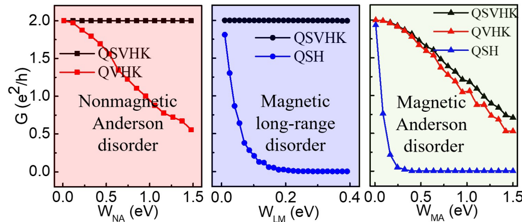

Fig.2: Junction conductance G versus different kinds of disorder strength at the Fermi level for the QSH, QVHK and QSVHK states.

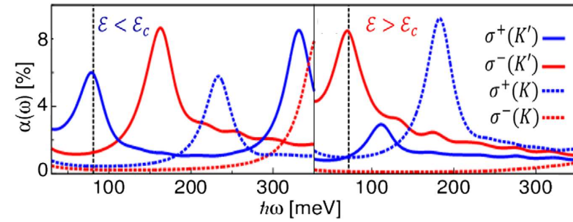

Fig.5: Helicity-resolved absorption spectra for both valleys when the applied electric field, ε, smaller and larger than the critical value, ε_c, where the gate controlled winding number change leads to a change in helicity for the absorption peak.

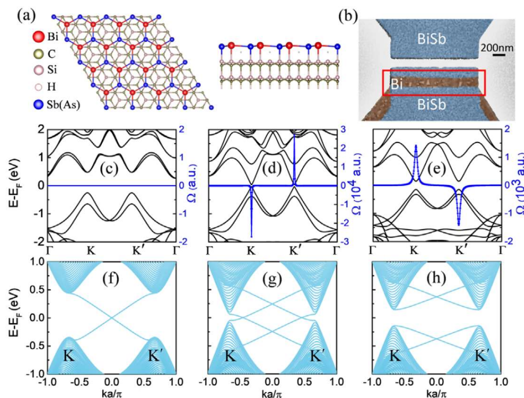

Fig.3: (a) Structures of BiSb or BiAs on a SiC substrate. (b) Scanning electron micrograph image of the planar BiSb-Bi-BiSb junction. Bulk bands (c-e) and edge states (f-h) for the Bi/SiC, BiSb/SiC, and BiAs/SiC, respectively.

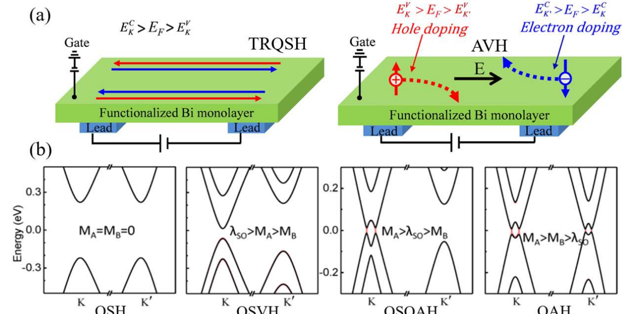

Fig.6: (a) gate controlled time reversal symmetry broken quantum spin Hall (QSH) and Anomalous valley Hall (AVH) states. (b) Magnetic controlled QSH, quantum spin-valley Hall (QSVH), quantum spin-quantum valley hall (QSH) and quantum anomalous Hall (QAH) states.

Designer Topological Magnetic Materials

G.J. de Coster[1] and M.J. Gilbert[2]
[1]Army Research Laboratory, 2800 Powder Mill Rd., Adelphi, MD 20783 USA
[2]University of Illinois at Urbana-Champaign, Urbana, IL, 61801 USA
george.j.decoster.civ@army.mil

Many promising applications of topological insulators (TIs) require imparting magnetism into a TI that: (1) produces a bandgap in the TI and (2) allows for room temperature operation [1]. In this talk, we theoretically examine the magnetic ground state and transport properties of Bi_2Se_3 proximity coupled to ferromagnetic (FM) [Co/Pt] multilayers (Fig. 1), for which FM order in the TI is experimentally observed [2]. The complexity of this FM/TI heterostructure (m-TI/FM) provides useful degrees of configurability to meet the design requirements of potential devices: (1) the final paramagnetic heavy metal Pt layer can be grown to different thicknesses to control how much magnetism from Co reaches the surface of Bi_2Se_3, (2) the metal in the FM multilayer may be changed for other metals to alter density of states, spin-orbit-coupling, etc. [3].

We simulate the magnetic profiles of the m-TI/FM heterostructures by minimizing the free energy of an interacting tight binding model (TBM) to incorporate the physics of both the bulk and interface states of the constituent subsystems (Fig. 2). Additionally, the TBM Hamiltonian fully accounts for the crystalline symmetries in the subsystems [4]. The chemical potential of the TI, μ, is included as a parameter as it may be experimentally tuned with a backgate voltage [5]. In the vein of an extended Hubbard model, we include both intra-layer, M_{intra} (local Coulomb), and inter-layer, M_{inter} (non-local Coulomb), magnetization terms whose coupling strengths are respectively U_{intra} and U_{inter}. U_{intra} is related to the Coulomb interaction in the TI after accounting for screening. U_{inter} arises from coupling of the TI surface state to the spin-polarized conduction electrons in the interfacial metal, consequently generating a greater exchange coupling leads to an enhanced Pauli susceptibility in the TI when compared to insulating TI/FM (i-TI/FM) devices. For a density of states (DOS) of ν in a metal layer of thickness d_{Pt}, and a TI surface state inverse penetration depth of λ, the interlayer Coulomb interaction scales as $U_{inter} \sim e^{-\lambda\, d_{Pt}}/\nu$. On aggregate, we find that the surface bandgap size scales roughly as $\Delta_{\mathrm{gap}} \sim 2(U_{intra} M_z^{intra} + U_{inter} M_z^{inter})$, where M_z^{intra} and M_z^{inter} are the z-directed intra and inter-layer magnetizations respectively.

For room temperature applications, we establish materials parameters and device configurations that generate a bandgap greater than 25 meV in at the Pt/Bi_2Se_3 interface, and a magnetization penetrating several layers into the TI. We determine that while small ~2-10% changes in conductivity of the heterostructure can be realized by varying μ around 75 meV, the Dirac Point (DP) of the surface states, a much larger ~10-20% change occurs concurrently with a switching from out-of-plane to in-plane magnetization along the easy x-axis of Bi_2Se_3 when the TI is gated from charge-neutrality to the valence bands (Fig. 3). The delineation of these key design parameters offers a promising route for experimentally creating and manipulating room temperature magnetism in FM/TI heterostructures for future device technologies.

[1] M.J. Gilbert, Commun Phys 4, 70 (2021) and references therein
[2] X. Zhang, B. Cui, J. Mao, et al, Phys. Status Solidi RRL (2020)
[3] C.D. Spataru and F. Leonard, Phys. Rev. B 90, 085115 (2014)
[4] S. Mao, A. Yamakage and Y. Kuramoto, Phys. Rev. B 84, 115413 (2011)
[5] D. Kim, S. Cho, N. Butch, et al., Nature Phys 8, 459–463 (2012)

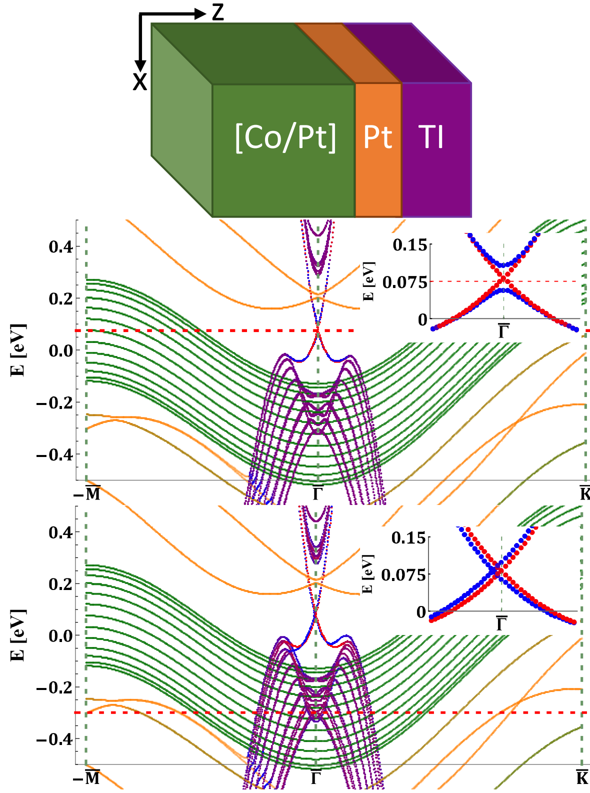

Fig. 1. (Top) Schematic of [Co/Pt]/(Bi2Se3) heterostructure. (Mid/Bot) Post free energy minimization electronic band structures for U_{inter}=1.85 eV, U_{intra} = 0.185 eV, (middle) μ= 75 meV and (bottom) μ = -300 meV (other material parameters outlined in Fig. 2). Bands are colored according to top diagram to indicate their material of origin, the blue/red bands are the top/bottom TI surface states respectively. The insets show the bottom surface state remains gapless for both chemical potentials, while the top surface forms a ~60 meV gap for μ=75 meV and shifts along the y-axis for μ= -300 meV due to the respective M_z and M_x orders that arise at the Pt/Bi_2Se_3 interface.

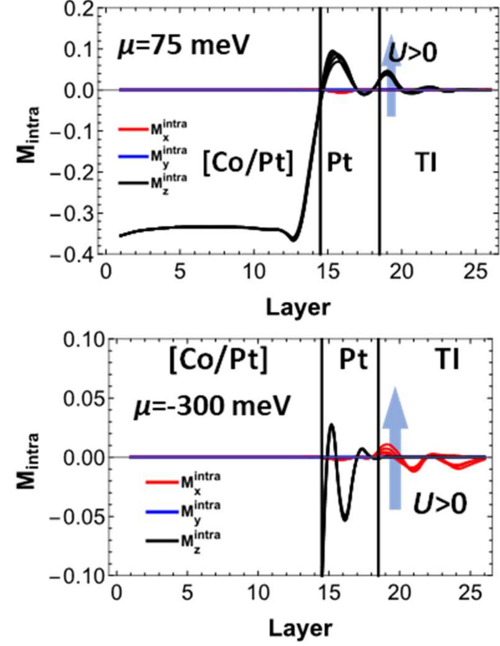

Fig.2: Plots of the intra layer magnetism terms that arise after free energy minimization due to U_{inter} and U_{intra} , discussed in the main text for (top) μ= 75 meV and (bottom) μ = 300 meV . The other simulation parameters are 14 [Co/Pt] FM multilayers, 4 Pt seed layers, 8 TI layers, a Pt SOC value of 0.15 eV Å. For μ= 75 meV, above a critical value $U_{inter,c}$ ~ 1.3 eV, the TI spontaneously magnetizes at the Pt/Bi2Se3¬ interface. We find that a U_{inter} = 1.85 eV confers a room temperature viable surface band gap of ~60 meV. When the chemical potential is in the bulk bands, μ= -300 meV,, the magnetization flips along the easy magnetic x-axis of Bi_2Se_3. The resultant magnetic phase is an itinerant style Stoner transition for conducting ferromagnets, and, thus, as the magnetization increases, so does the conductivity of the system, as seen in Fig. 5.

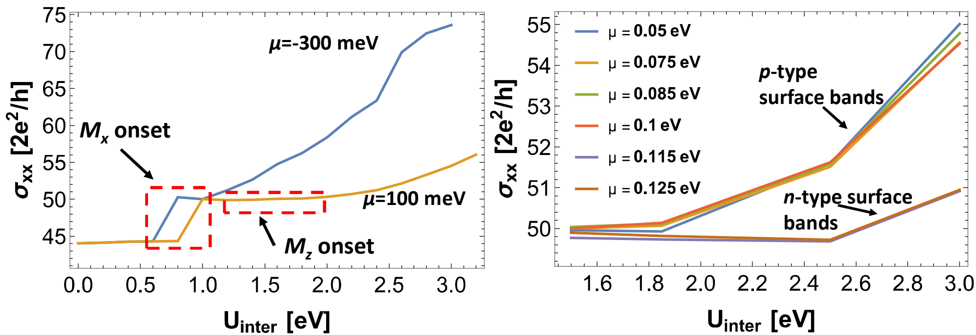

Fig. 3. Kubo formula computed longitudinal conductivity σ_{xx} of m-TI/FM after energy minimization for different gate voltages/chemical potentials as a function of U_{inter}. We see (left) that by driving μ from the valence band (μ = -300 meV) to near the DP (μ = 100 meV), σ_{xx} may be reduced by ~10-20% for modest values of U_{inter}, whereas (right) if one varies the chemical potential from p to n type surface bands ($\mu - E_{Dirac} \lesssim 100$ meV), only a ~2-10% change in conductivity is possible. In all cases the initial conductivity enhancement is due to a spontaneous M_x^{intra} forming along the easy axis of Bi_2Se_3. The large bulk DOS at μ= -300meV causes M_x^{intra} to grow with U_{inter} and U_{intra} and enhances σ_{xx}. For μ~100 meV, the system switches to favoring z-directed magnetization with increasing U_{inter}, and the strength of the surface bandgap depends on μ-E_{Dirac}, and the curvature of the bands above and below the DP.

Towards Non-Abelian Statistics in Topological Planar Josephson Junctions

Tong Zhou[1], Matthieu C. Dartiailh[2], Kasra Sardashti[2], Jong E. Han[1], Alex Matos-Abiague[3], Javad Shabani[2], and Igor Žutić[1,*]

[1]*Department of Physics, University at Buffalo, State University of New York, Buffalo, USA*

[2]*Center for Quantum Phenomena, Department of Physics, New York University, USA*

[3]*Department of Physics and Astronomy Wayne State University Detroit, USA*

**e-mail: zigor@buffalo.edu*

Topological superconductivity supports exotic Majorana bound states (MBS) which are chargeless zero energy emergent quasiparticles. With their non-Abelian statistics and fractionalization of a single electron stored nonlocally as a spatially separated MBS, they are particularly suitable for implementing fault-tolerant topological quantum computing [1]. While the main efforts to realize MBS have focused on one-dimensional (1D) systems, the onset of topological superconductivity requires fine-tuning and geometric constraints pose significant challenges for their demonstration of non-Abelian statistics [1]. Here, building on recent experimental advances in planar Josephson junctions (JJs) [2-4], we reveal how to overcome this obstacle in topological JJs and show non-Abelian statistics using phase or mini-gate control. We propose a novel platform of X-shaped JJs [5], where external flux control of the superconducting phase difference can generate, exchange, and braid MBS. The underlying topological superconductivity exists over a large parameter space, consistent with our fabricated materials. With our experimental control of superconducting properties using five mini-gates in InAs/Al-based JJs, we demonstrate how such mini-gate control demonstrates non-Abelian statistics through MBS fusion, detected by charge sensing using quantum point contacts [6]. We further reveal how spin valves can be used through their fringing fields to implement MBS and their braiding [7,8]. Our proposals to identify elusive non-Abelian statistics, as an important milestone towards topological quantum computing, motivate also further MBS studies in other 2D systems with similar control.

[1] D. Aasen et al., Phys. Rev. X **6**, 031016 (2016).

[2] A. Fornieri, et. al, Nature **569**, 89 (2019).

[3] H. Ren, et. al, Nature **569**, 93 (2019).

[4] M. Dartiailh, et. al, PRL **126**, 036802 (2021).

[5] T. Zhou, et. al, PRL **124**, 137001 (2020).

[6] T. Zhou, et. al, arXiv: 2101.09272 (2021).

[7] T. Zhou et al., Phys. Rev. B **99**, 134505 (2019).

[8] N. Mohanta, T. Zhou et al., Phys. Rev. Appl. **12**, 034048 (2019).

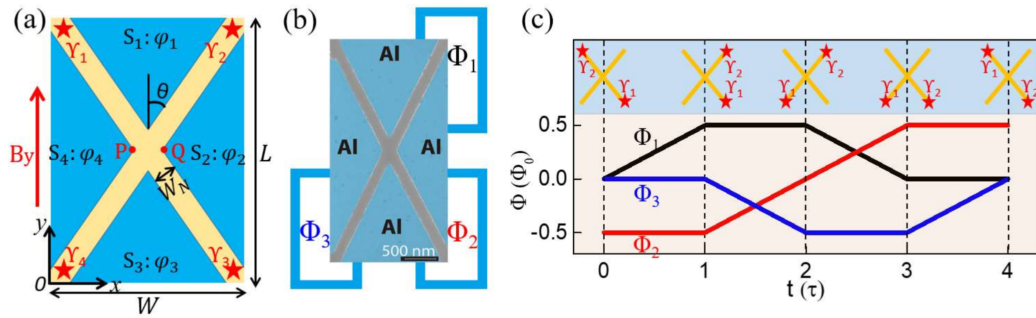

FIG. 1. (a) X-shaped junction (XJ) schematic formed by epitaxial superconducting (S) regions (blue) covering a 2DEG (yellow). MBS $\gamma_{1\text{-}4}$ (stars) are obtained through modulating the phase differences between $\varphi_{1\text{-}4}$. (b) SEM image for the XJ with schematic external fluxes Φ_1, Φ_2, and Φ_3. (c) MBS exchange with fluxes, τ is the switching time, and Φ_0 is the magnetic flux quantum.

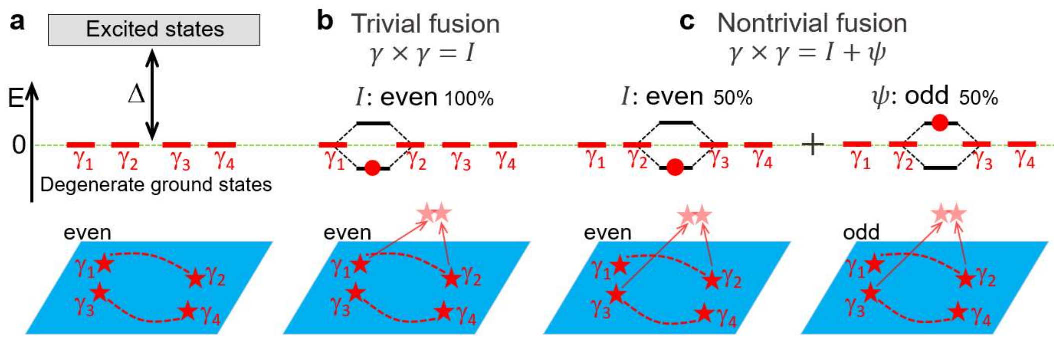

FIG. 2. (a) Topological superconductor (blue) hosting MBS, $\gamma_{1\text{-}4}$. They behave as non-Abelian anyons and lead to the four-fold degeneracy in topological ground states, separated by the energy gap, Δ, from the trivial excited states. (b) and (c) Different fusion outcomes: trivial fusion of γ_1 and γ_2, 100% probability to access vacuum, I (Cooper pair condensate), and nontrivial fusion of γ_2 and γ_3, equal probabilities to access I or an unpaired fermion, ψ. Red dashed lines: paired MBS. In each case bringing closer MBS leads to the level splitting from the initial zero energy modes. Filling the lower level, corresponding to I with even parity, means the absence of a given particle, while filling the upper level refers to ψ with odd parity. We assume initially even parity of the system. The net change in the charge characterizes nontrivial fusion.

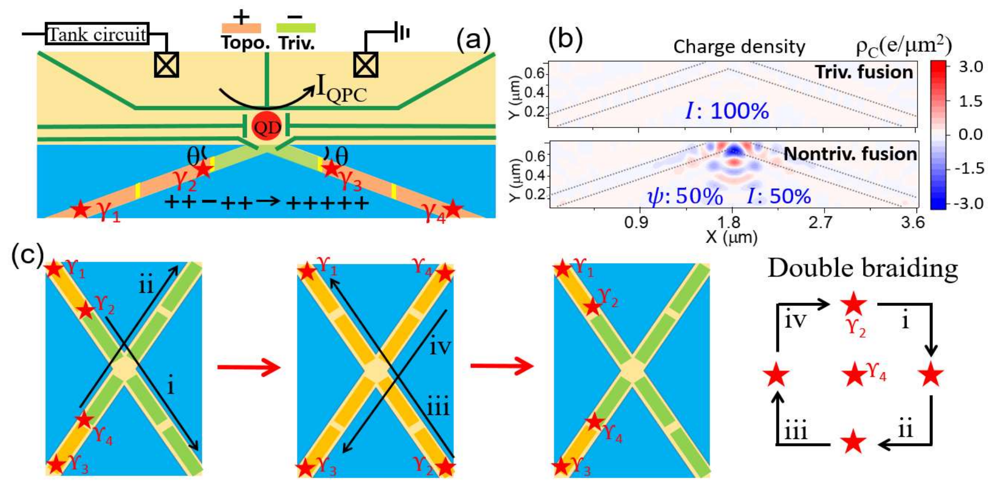

FIG. 3. (a) Schematic of a setup incorporating a quantum dot (QD) and a quantum point contact (QPC) to detect the fusion outcome in a V-shaped junction (VJ) with mini-gates control. The VJ is formed by by superconducting, $S_{1\text{-}3}$, regions (blue), partially covering a 2D electron gas (yellow). The electron density in the uncovered part is locally tuned using mini gates to support topological (orange) and trivial (green) regions, by imposing the mini-gate voltage V_+ and V_-. MBS $\gamma_{1\text{-}4}$ (stars) form at the ends of the topological regions and can be fused at the apex of the VJ. (b) The calculated charge density in the VJ after trivial and nontrivial fusions. (c) Scheme of MBS Braiding with mini-gate control, where the exchange of γ_2 and γ_4 demonstrates the double braiding.

Ultrafast carrier dynamics in β-Ga_2O_3

Saulius Marcinkevičius[1] and James S. Speck[2],
[1]*Department of Applied Physics, KTH Royal Institute of Technology, AlbaNova University Center, 10691 Stockholm, Sweden*
[2]*Materials Department, University of California, Santa Barbara, California 93106, USA*
sm@kth.se

Effects of ultrafast carrier dynamics, such as electron-phonon scattering and hole self-trapping, play an important role in determining electronic and optical properties of semiconducting materials. In that respect monoclinic β-Ga_2O_3, a transparent semiconducting oxide with a large perspective in power electronics and UV photonics, is no exception. So far, electron-polar optical (PO) phonon scattering in β-Ga_2O_3 has been studied by electrical measurements and theoretical modelling; intervalley scattering has not been experimentally assessed. Dynamics of hole self-localization into polaron states, a phenomenon crucial for *p*-type conductivity, remained elusive, and self-localization has often been considered instantaneous. In this work, we use ultrafast differential absorption and reflection spectroscopy with pump and probe pulses at different wavelengths to evaluate these parameters in a direct way.

Most of the experiments were performed on *n*-type Sn-doped β-Ga_2O_3 single crystal of (100) crystallographic orientation. By properly choosing pump and probe wavelengths, different effects could be measured. With pump photon energies in the ultraviolet and probe photon energies in the near infrared (IR), parameters of the hole self-trapping were evaluated [1]. At room temperature, the self-trapping time was found to be 0.5 ps, increasing to 1.1 ps at 10 K. In terms of the configuration coordinate diagram, at low temperature the self-trapping takes place via tunneling. The hole self-trapping coefficient is estimated as 6.4×10^{-8} cm^3/s.

With both pump and probe pulses in the near IR and visible, characteristic times for electron-phonon scattering were assessed [2]. It was found that the electron-PO phonon scattering time is 4.5 fs, and the time for the electron scattering to and from the side valley is 80 fs. Experiments with tunable pulse photon energies allowed determining the energy of the 2nd lowest conduction band valley. The intervalley energy was found to be 2.6 eV.

[1] S. Marcinkevičius and J. S. Speck, Appl. Phys. Lett. **116**, 132101 (2020).
[2] S. Marcinkevičius and J. S. Speck, Appl. Phys. Lett. **118**, 242107 (2021).

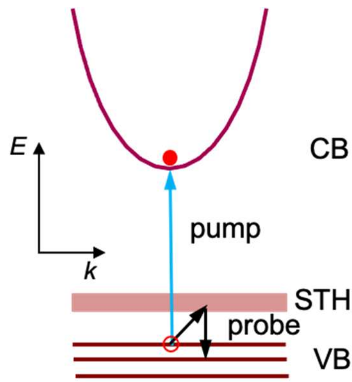

Fig.1: Schematics of the pump-probe experiment to study hole self-trapping. Abbreviations: CB – conduction band, VB – valence bands, STH – self-trapped hole states. Blue vertical arrow – pump transition, black vertical arrow – probe transition.

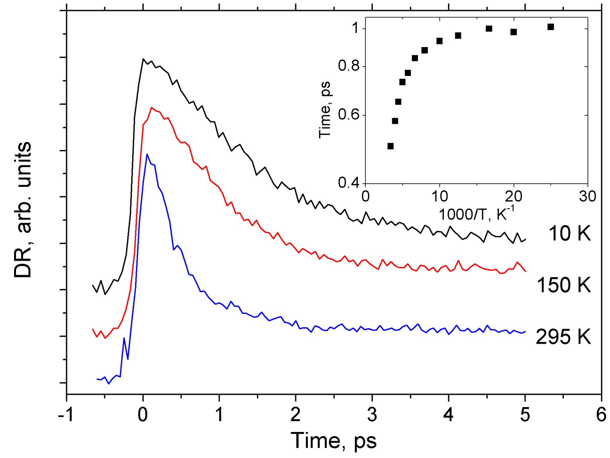

Fig.2: Normalized differential reflection transients for 4.59 eV pump and 1.53 eV probe pulse energies at different temperatures. The transient decay reflects hole self-trapping. The inset shows the decay time dependence on the inverse temperature.

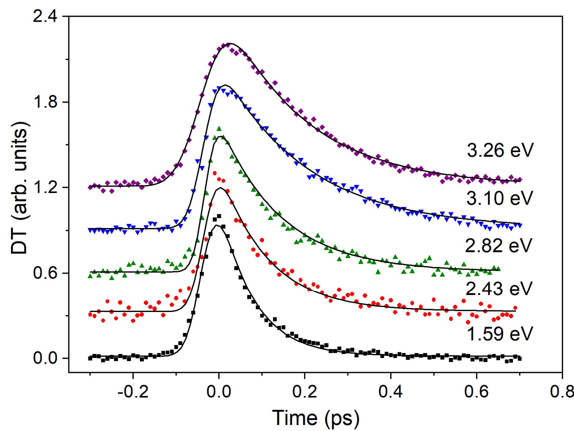

Fig.3: Differential transmission transients for pump and probe photon energies in the infrared and visible. Transient decay reflects electron relaxation to the bottom of the conduction band.

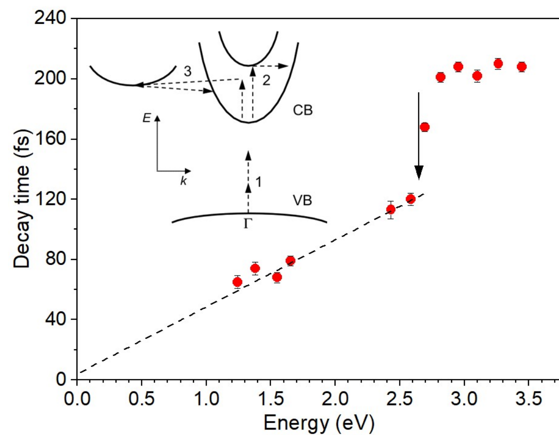

Fig.4: Spectral dependence of the differential transmission decay times. Dots – experimental points, dashed line – linear fit of the decay times in the low energy region. The arrow indicates the threshold energy for the intervalley scattering. The inset shows schematics of the band structure including the top valence band (VB), and two lowest conduction bands (CB) at the Γ point and the side valley. The process 1 indicates two photon absorption, process 2 – free electron absorption to the 2nd conduction band at the Γ point and scattering back to the 1st band, and process 3 – free electron absorption with scattering to and from the side valley.

Influence of microstructure on electrical properties of titanium dioxide thin films

K. Kulinowski[1], M. Radecka[2], and B. J. Spisak[1]
[1]Faculty of Physics and Applied Computer Science, AGH University of Science and Technology, Al. A. Mickiewicza 30, 30-059 Kraków, Poland
[2]Faculty of Materials Science and Ceramics, AGH University of Science and Technology, Al. A. Mickiewicza 30, 30-059 Kraków, Poland
kulinowski@agh.edu.pl

Titanium dioxide belongs to the class of the wide-bandgap semiconductors, with the bandgap changing between 3.0 eV and 3.2 eV for the rutile and anatase forms, respectively [1]. The conduction band of TiO_2 is predominately composed from Ti 3d states that lead to profound consequences for the electron-effective mass and the mobility of the carriers. The electrical and optical properties of these two polymorphic forms differ significantly between each other. The occurrence of anatase and rutile forms in thin films depends on the conditions of the deposition processes. Additionally, the sputtering of the titanium target in the reactive Ar + O_2 gas atmosphere influences a degree of non-stoichiometry, and with increasing oxygen content in the atmosphere, an increase in the amount of anatase is observed.

In performed experiments, TiO_2 thin films were deposited by the RF reactive magnetron sputtering from titanium target in O_2 + Ar atmosphere with different oxygen content. The electrical properties of thin films with varying deviation from stoichiometry and rutile phase weight percentage were analyzed. The impact of these factors on the electrical properties of TiO_2 thin films was determined by conductivity measurements as a function of temperature. In turn, the resistance of these samples was calculated as an inverse of a slope of I-V characteristics for temperatures ranging from 150 K to 300 K. Results were analyzed through the grain boundary model [2], which was proven to be an accurate model describing transport properties of titanium dioxide [3, 4]. According to this, the existence of trapping states near the grain boundary forms the energy barriers. Their parameters can be estimated by the fitting procedure of the Arrhenius-like equation to the conductivity plot. It was shown the barrier heights E_b for samples with oxygen content from 10% up to 20% are monotonically rising with a sudden drop between samples with O_2 content equal to 20% and 25%. Applying the presented model, several parameters characterizing considered thin films were calculated, like donor concentration N_D, hopping energy W and the Debye screening length L_D. For all samples, the boundary grain model condition ($L > L_D/2$) is fulfilled.

K.K. is supported by the EU Project POWR.03.02.00-00-I004/16. M.R., and B.J.S. are supported by Polish Minister of Science and Higher Eduction within the framework of subvention for science in 2021.

[1] R. G. Breckenridge and W. R. Hosler, Phys. Rev. **91**, 793 (1953)
[2] J. Y. W. Seto, J. Appl. Phys. **46**, 5247 (1975).
[3] A. Yildiz et al., J. All. Comp. **493**, 227-232 (2010).
[4] A. Yildiz et al., J. Mat. Sci. **21,** 692–697 (2010).

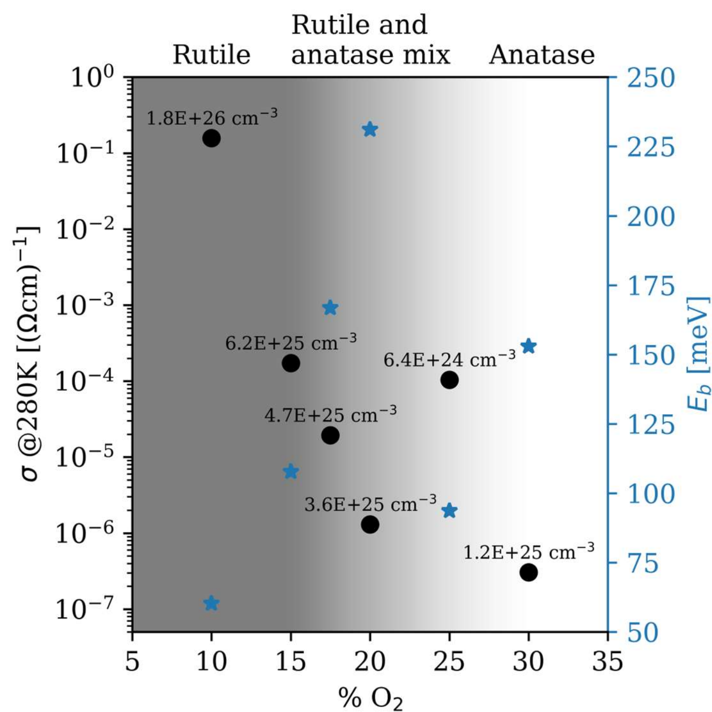

Figure 1: Electrical conductivity at 280 K, donor concentration N_D (numeric values) and barrier height E_b as a function of an oxygen content.

(a) (b)

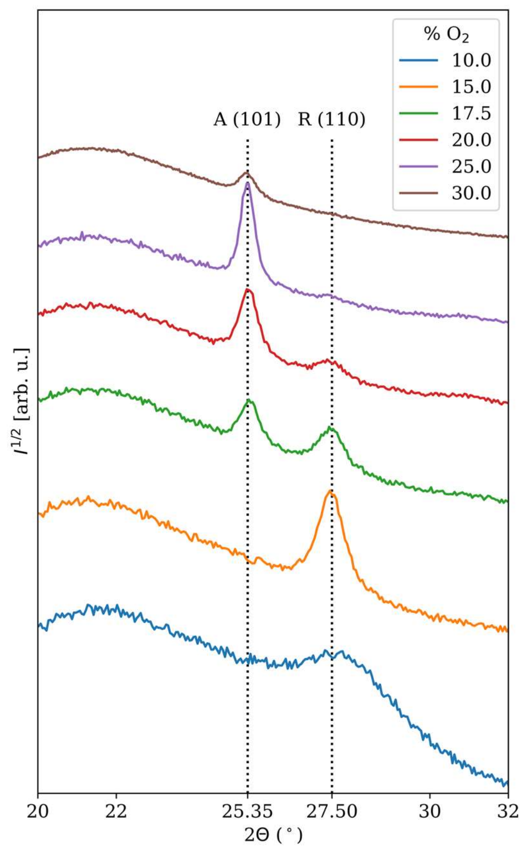

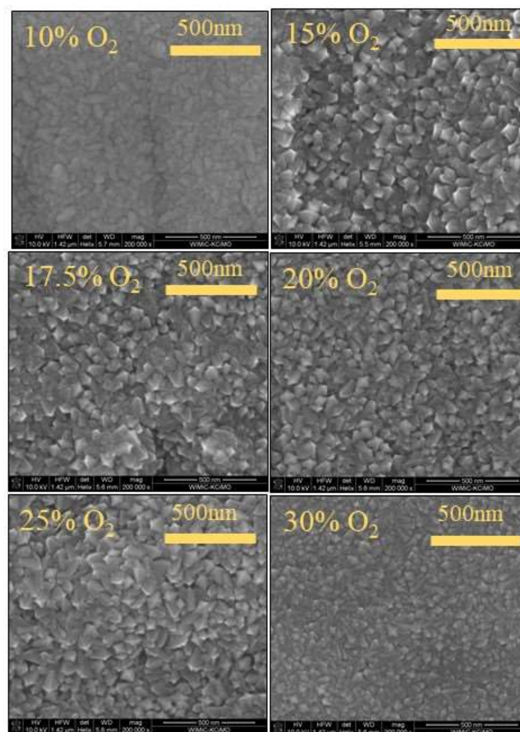

Figure 2: (a) XRD patterns of TiO_2 thin films- A stands for anatase and R for rutile; (b) SEM images of the surface of TiO_2 thin films

Ultrathin MoO_3 (010) films grown by MBE on stepped *c*-plane sapphire

P. Novotný, A. J. Pedersen, and H. H. Lamb

Department of Chemical and Biomolecular Engineering, North Carolina State University, Raleigh, NC 27695-7905, USA
lamb@ncsu.edu

Ultrathin α-MoO_3 (010) films were grown on stepped *c*-plane sapphire substrates by molecular beam epitaxy (MBE) using MoO_3 vapor from a conventional Knudsen cell [1]. Stepped sapphire (0001) substrates were prepared by *ex situ* annealing at 1100-1300°C in dry air. Under these conditions, step bunching resulted in multi-stepped surfaces with wide atomically smooth terraces. *In situ* annealing at 700°C in 5×10^{-6} Torr O_2 provided clean substrates for growth, as evidenced by reflection high-energy electron diffraction (RHEED) and x-ray photoelectron spectroscopy (XPS). Ultrathin films were grown at 450°C via a self-limiting process representing a balance between the incident flux and MoO_3 desorption. Atomic force microscopy (AFM) images revealed elongated MoO_3 (010) bilayer islands (0.7-nm thick) on sapphire (0001) terraces. The Mo 3d XP spectral envelope of the films was fit using a single spin-orbit doublet with a 233.0-eV Mo $3d_{5/2}$ binding energy consistent with MoO_3. A film thickness of 0.48 nm was estimated from the Mo 3d/Al 2p XPS intensity ratio. Thicker monocrystalline α-MoO_3 (010) films $[(010)_{\alpha\text{-}MoO3} \| (0001)_{sapphire}]$ were grown at 450°C using a higher incident MoO_3 flux and characterized by AFM, XPS, x-ray diffraction, and cross-sectional transmission electron microscopy. The step-terrace surface morphology of these films strongly suggests multilayer growth.

[1] P. Novotný and H. H. Lamb, J. Vac. Sci. Technol. A **39**, 043406 (2021).

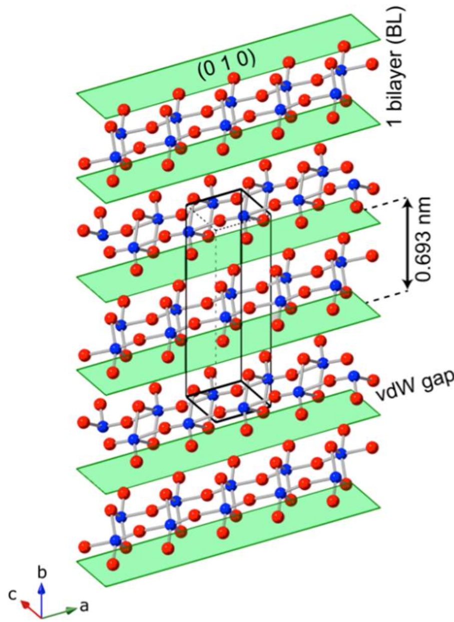

Fig.1: Crystal structure of α-MoO_3. The orthorhombic unit cell (outlined in black), van der Waals (vdW) gaps (green), and bilayer (BL) thickness are shown. Molybdenum and oxygen atoms are shown in blue and red, respectively.

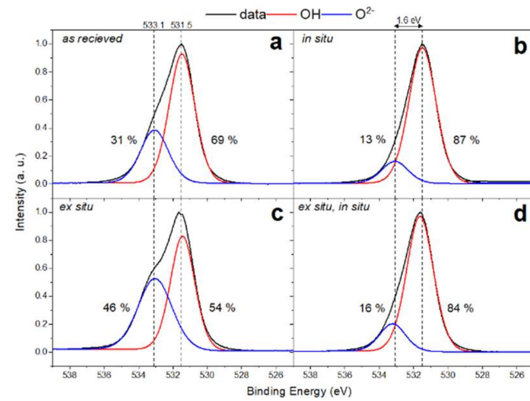

Fig.3: O 1s XP spectra of sapphire substrates: (a) as-received, (b) sample after heating to 700°C in 5 x 10^{-6} Torr O_2 for 30 min, (c) sample annealed ex situ at 1100°C, 24 h in dry air, (d) ex situ annealed sample after heating to 700°C in 5 x 10^{-6} Torr O_2 for 30 min.

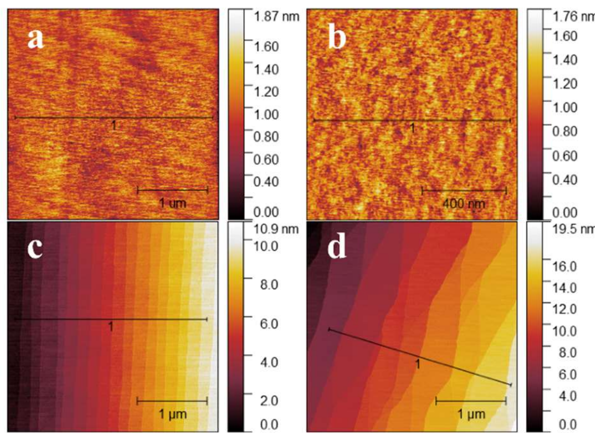

Fig.2: AFM images of sapphire (0001) substrates: (a) as-received; (b) annealed in air at 900°C, 4 h; (c) annealed in air at 1100°C, 24 h; (d) annealed in air at 1300°C, 24 h.

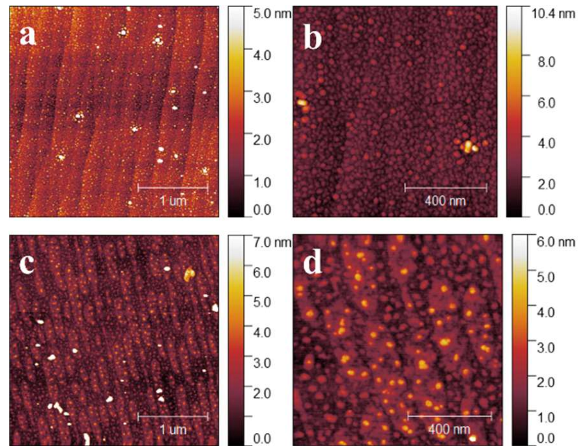

Fig.4 AFM images of MoO_3 deposited on sapphire (0001) with parallel steps and terraces at 450°C: (a) 5 min deposition (3x3) μm^2 scan, (b) 5 min deposition (1x1) μm^2 scan, (c) 15 min deposition (3x3) μm^2 scan, (d) 15 min deposition (1x1) μm^2 scan.

Dynamically tunable single-layer VO_2/metasurface based THz cross-polarization converter

R. Yahiaoui[1], Z.A. Chase[1], C. Kyaw[2], E. Seabron[3], J. Mathews[4], and T.A. Searles[1]

[1] *Department of Electrical and Computer Engineering, University of Illinois at Chicago, Chicago, IL 60607, USA* (*tsearles@uic.edu*)
[2] *Department of Physics, Morehouse College, Atlanta, GA 30314, USA*
[3] *Department of Electrical Engineering, Howard University, Washington, DC 20059*, USA
[4] *Department of Physics, University of Dayton, Dayton, OH 45469*, USA

Cross polarization transmission, a key factor to achieve optical activity, is demonstrated in a single-layer THz metadevice comprised of a two dimensional array of split ring resonators, each with a vanadium oxide (VO_2) pad, integrated into one of the two capacitive gaps of the unit cell (Fig. 1a). Numerical investigations show that as the conductivity of VO_2 increases the amplitude of the cross-polarization intensity decreases but maintains a wider broadband range than previously reported for single layered hybrid metamaterial (MM) devices as the VO_2 transforms from the insulator to metallic phase (Fig. 1b). Concurrently, the asymmetric transmission, optically modulated by the device, is higher than that of multi-layered MM devices. The material properties of VO_2, introduce a promising method that allows for an active sub-cycle dynamic tunability for THz polarization conversion with multiple modalities using optical, electrical or thermal switching which allows for an important step forward in developing compact, integrated, passive and active metadevices for polarization and wavefront control application in the THz regime [1].

[1] R. Yahiaoui et al., J. Phys. D Appl. Phys. ***54****, 235101 (2021).*
Research supported by the Office of Naval Research.

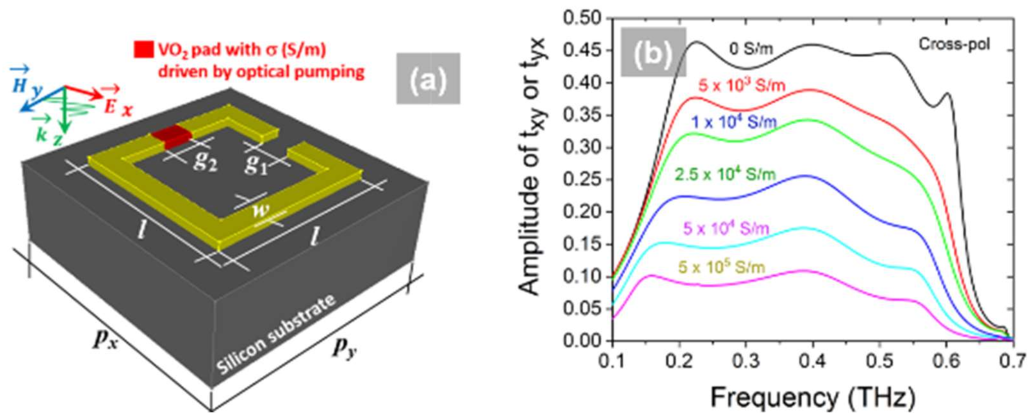

Fig.1: Phase-change MM for Polarization Conversion. (a) Unit cell of the investigated active hybrid metadevice with the corresponding electromagnetic excitation configuration (the red is the PCM, in this case VO_2). The relevant geometrical dimensions are: $P_x = P_y = 300$ µm, $l_x = l_y = 250$ µm, $w = 35$ µm and $g_1 = g_2 = 35$µm. (b) Simulated cross-polarized transmission coefficients.

Relaxation and darkening of excitonic complexes in electrostatically-doped monolayer semiconductors

M. Yang[1], L. Ren[2], C. Robert[2], D. Van Tuan[1], L. Lombez[2], B. Urbaszek[2], X. Marie[2], and H. Dery[1]

[1]Department of Electrical and Computer Engineering, University of Rochester, Rochester, New York 14627, USA

[1]Universite de Toulouse, INSA-CNRS-UPS, LPCNO, 135 Av. Rangueil, 31077 Toulouse, France

hanan.dery@rochester.edu

Photoluminescence measurements in monolayer WSe_2 point to the importance of the interaction between charged particles and excitonic complexes [1]. A key role of this interaction is governed by exchange scattering, referring to cases wherein the particle composition of the complex changes after the interaction. For example, exchange scattering renders bright excitonic complexes dark in monolayer WSe2 on accounts of the unique valley-spin configuration in this material. In addition to the ultrafast energy relaxation of hot excitonic complexes following their interaction with electrons or holes, our analysis sheds light on several key features that are commonly seen in the photoluminescence of this monolayer semiconductor. In particular, we can understand why the photoluminescence intensity of the neutral bright exciton is strongest when the monolayer is hole-doped rather than charge neutral or electron-doped [2-7]. Or the reason for the dramatic increase of the photoluminescence intensity of negatively charged excitons (trions) as soon as electrons are added to the monolayer [2-7]. To self-consistently explain the findings, we further study the photoluminescence spectra at different excitation energies and analyze the behavior of the elusive indirect exciton [8].

[1] C. Robert *et al.,* Nat. Commun. **12**, 5455 (2021).

[2] S.-Y. Chen *et al.,* Nat. Commun. **9**, 3717 (2018).

[3] Z. Ye *et al.,* Nat. Commun. **9**, 3718 (2018).

[4] Z. Li *et al.,* Nat. Commun. **9**, 3719 (2018).

[5] M. Barbone *et al.,* Nat. Commun. **9**, 3721 (2018).

[6] E. Liu *et al.,* Phys. Rev. Lett. **124**, 196802 (2020).

[7] Z. Li *et al.,* ACS Nano **13**, 14107 (2019).

[8] M. He *et al.,* Nat. Commun. **11**, 618 (2020).

978-3-9504738-3-4

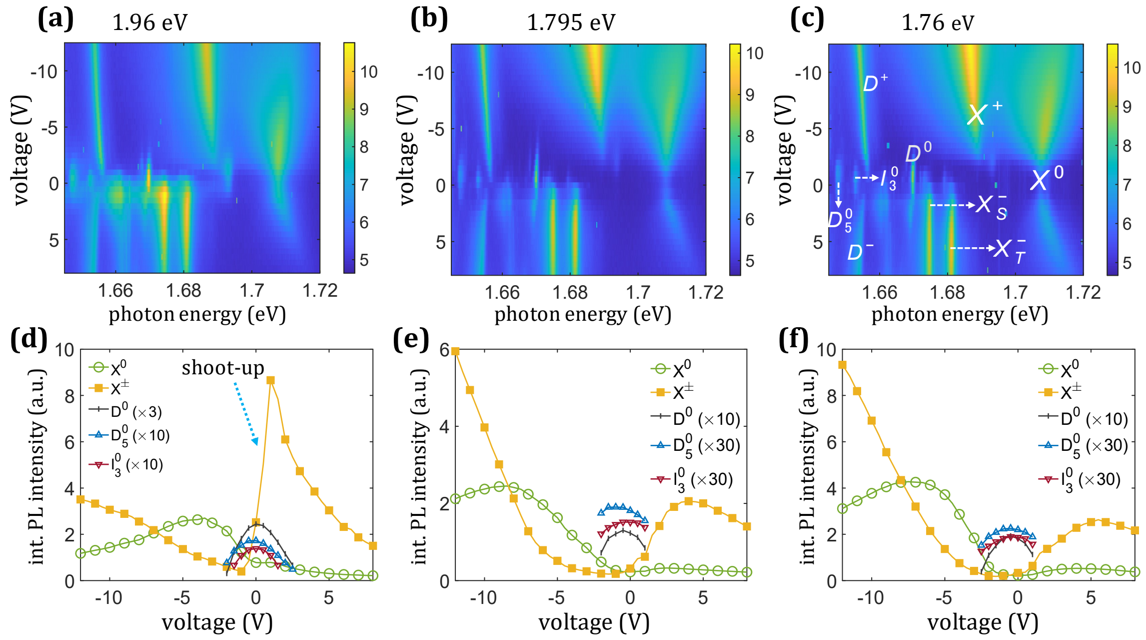

Fig1. (a)-(c) Colormaps of the total PL intensities (log scale) in a second ML-WSe$_2$ charge-tunable device, following linearly polarized photoexcitation. The temperature is 4K and the laser power is 10 μW. The laser photon energies are indicated in each case, where ħω=1.96 eV in (a) corresponds to excitation of free electron-hole pairs in the continuum. The other two laser energies in (b) and (c) fall in the spectral range between the ground state of the bright exciton and excited-state of bright trions (i.e., between 1s and 2s). (d)-(f) The integrated PL intensities of various peaks, calculated from the respective PL spectra in (a)-(c). Results are shown for the bright exciton (open circles), bright trions (filled squares), dark exciton, its Γ_5 phonon replica (triangles), and the K_3 phonon replica of the indirect exciton (flipped triangles).

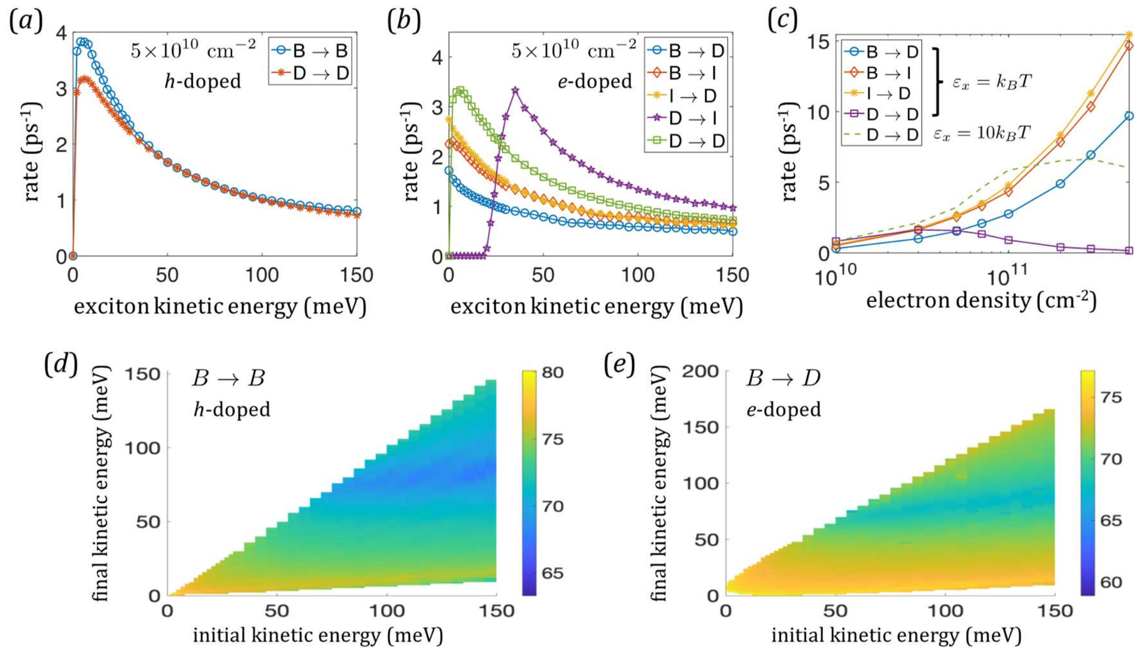

Fig. 2. Calculated transition rates between various exciton species in ML-WSe$_2$ at 5K when the free-charge density is 5x10^{10} cm^{-2}. (a)/(b) The rates as a function of the exciton kinetic energy in the initial state for hole/electron doped MLs. Transition rates between indirect excitons, I → I, are not shown in these plots but they are similar to the those between dark excitons, D → D. (c) The rates as a function of electron density for thermal excitons. (d) and (e) Log-scale colormaps of the kernel functions for the transitions B → B and B → D in hole-doped and electron-doped MLs, respectively. The units of the kernel function are (J s)$^{-1}$. Yellow/blue colors mean exponentially larger/smaller scattering probability between certain initial (x-axis) and final (y-axis) kinetic energies.

Modulation Doping in 2D Materials

K.S. Burch[1]
[1]*Department of Physics, Boston College, Chestnut Hill, Massachusetts 02467-3804, USA*
ks.burch@bc.edu

Two-dimensional (2d) nano-electronics, plasmonics, spintronics and emergent phases require clean and local charge control, calling for layered, crystalline acceptors or donors. Here I will describe how the Relativistic Mott Insulating state of $RuCl_3$, a 2D antiferromagnet, provides a new opportunity to introduce modulation doping into 2D materials. Specifically, we demonstrate and optimize this charge transfer with extensive Raman, photovoltage, and electrical conductance measurements combined with ab initio calculations. Also, we find the doping is exceptionally local, can occur through hBN, works with various exfoliated, CVD, and MBE materials.

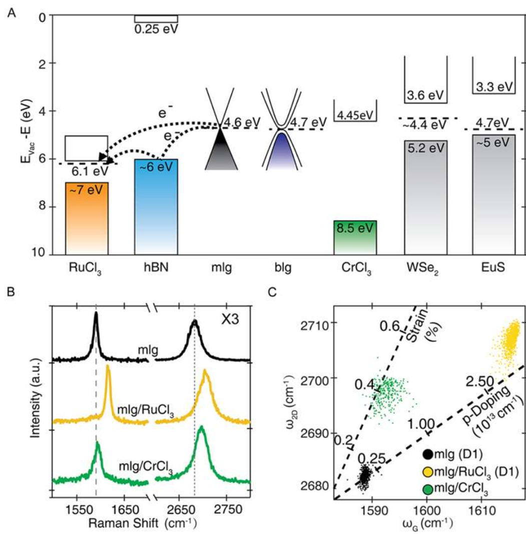

Fig.1Charge transfer in α-RuCl3 heterostructures. (A) Band alignment schematic; the work function difference between α-RuCl3 and other compounds yields charge transfer. (B) Representative Raman spectra for mlg (black trace), mlg/RuCl3 (yellow trace), and mlg/CrCl3 (green trace) samples. (C) Correlation between the graphene G and 2D Raman mode for different mlg-based heterostructures, result of only strain or doping indicated with dashed lines.

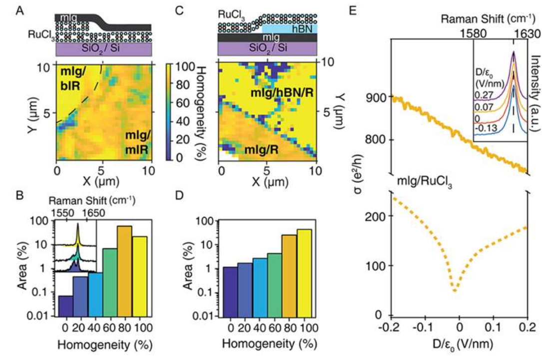

Fig.3: Homogeneity of charge transfer. (A,C) Spatially resolved homogeneity maps for D1 and D3, respectively, with stacking schematics depicted above. (B,D) Histograms of the homogeneity values for each map. (B, inset) Three representative Raman spectra from D1 with varying weights of shifted and unshifted peaks, showing the different homogeneity. (E) Comparison of conductivity versus displacement field for a RuCl3/mlg/SiO2 device with surface contacts between the mlg and α-RuCl3 (dashed) and a fully encapsulated, edge-contacted hBN/mlg/RuCl3 device (solid) device. Inset, Ddependence of mlg/RuCl3 Raman G peak.

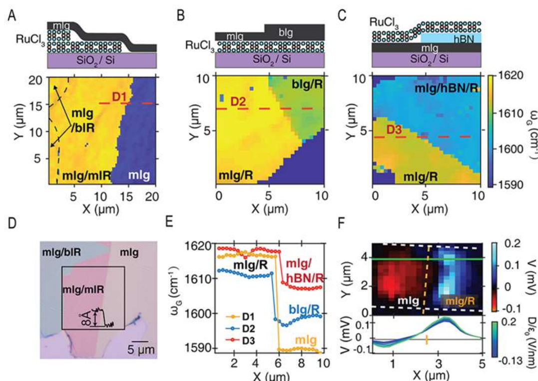

Fig.2: (A-C) Raman maps of the graphene G peak frequency for $RuCl_3$ heterostructures with schematics of each above. (D) False-color optical micrograph of D1, mlR is monolayer $RuCl_3$, blR is bilayer $RuCl_3$, and R means $RuCl_3$. AFM of monolayer $RuCl_3$ step height (inset). The black square marks the area scanned in (A). (E) Horizontal linecuts of the G peak frequency across the lines in (A−C), revealing the sharp doping change. (F) (Top) Scanning photovoltage map of mlg/ $RuCl_3$ heterostructure acquired with a 532 nm laser. mlg is between the white dashed lines, while right of the orange dashed line is covered by $RuCl_3$. (Bottom) Gate voltage dependence of the photovoltage along the green linecut in the scanned photovoltage map, consistent with a p−p′ lateral junction.

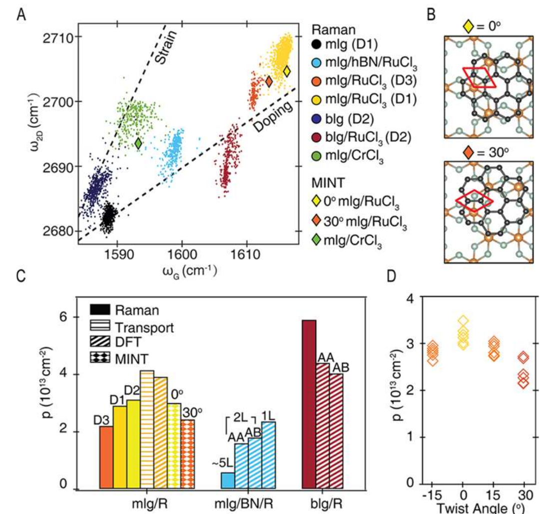

Fig.4: Summary of charge transfer from α-RuCl3. (A) Correlation between the graphene G and 2D Raman mode for all samples discussed in the text (dots), as well as converted MINT results (diamonds) for different twist angles. (B) Representative MINT supercell alignments for 0° (top) and 30° (bottom) mlg/RuCl3 twist angles. (C) Doping levels calculated from Raman spectroscopy (filled bars), transport (horizontally striped bars), DFT (diagonally striped bars), and MINT (diamond-checkered bars). (D) MINT-calculated mlg doping levels for six graphene supercell positions at different relative twist angles.

Controlling interfacial charge transfer in two-dimensional van der Waals heterostructures

H. Zhao
Department of Physics and Astronomy, The University of Kansas,
Lawrence, Kansas 66045, United States of America
huizhao@ku.edu

Two-dimensional (2D) materials have drawn considerable attention as new forms of nanomaterials. One intriguing aspect of these materials is that they provide a new route to fabricating multilayer heterostructures. Efficient and controllable interfacial charge transfer is a key element harnessing emergent electronic and optoelectronic properties of such 2D heterostructures. Previous time-resolved studies have shown universal, ultrafast, and highly efficient charge transfer in several van der Waals heterostructures [1-4]. However, effective control of this process has been less developed. I will present our latest efforts to identify and demonstrate the control of interfacial charge transfer process in van der Waals heterostructures. Energy band alignment engineering is found to be feasible to control the charge transfer and achieve desirable interlayer carrier population [5-7]. All-optical and ultrafast control of interfacial charge transfer and behavior of interlayer excitons by a laser pulse is demonstrated [8]. A built-in dipole moment in the Janus structures [9] can regulate directional interfacial charge transfer. These progresses suggest the feasibility of controlling interfacial charge transfer in van der Waals heterostructures, which is important for their electronic and optoelectronic applications.

[1] X. Hong et al., Nat. Nanotechnol. **9**, 682 (2014).
[2] J. He et al., Nat. Commun. **5**, 5622 (2014).
[3] F. Ceballos et al., ACS Nano **8**, 12717 (2014).
[4] F. Ceballos et al., Nano Lett. **17**, 1623 (2017).
[5] S. Pan et al., Appl. Phys. Lett. **118**, 253106 (2021).
[6] T. R. Kafle et al., J. Am. Chem. Soc. 141, 11328 (2019).
[7] F. Ceballos et al., Phys. Rev. Mater. **1**, 044001 (2017).
[8] P. Zereshki et al., Phys. Rev. B **103**, 165416 (2021).
[9] T. Zheng et al., Nano Lett. **21**, 931 (2021).

Ab-initio Calculations of Edge States in Topological 1T′ MoS_2 Nanoribbons

Al-Moatasem El-Sayed[2], Heribert Seiler[1,2], Hans Kosina[2], Siegfried Selberherr[2], and Viktor Sverdlov[1]

[1] *Christian Doppler Laboratory for Nonvolatile Magnetoresistive Memory and Logic at the*
[2] *Institute for Microelectronics, TU Wien, Gußhausstraße 27-29/E360, 1040 Vienna, Austria*
e-mail: {el-sayed|seiler|kosina|selberherr|sverdlov}@iue.tuwien.ac.at

Well known two-dimensional (2D) materials, including MoS_2, possessing high potential for future ultrascaled microelectronic devices develop unusual properties in a so called 1T′ phase (Fig.1). Namely, the 1T′ phase is a 2D topological insulator (TI). The phase is characterized by an inverted band structure with the hole band lying above the conduction band (Fig.2). At intersections of the bands the fundamental band gap is opened by the spin-orbit interaction. Metallic highly conductive edge states protected against backscattering by nonmagnetic impurities exist within the gap. The existence of these edge states can be controlled by a normal electric field. The field induces a phase transition between the topological and normal state in the 1T′ phase [1]. In contrast to the TI phase, the edge states are forbidden in the bandgap of a normal insulator. The electric field induced phase transition between the TI phase with the current-carrying states and the normal phase can be used to build TI-based transistors. To enhance the on-current, more edges are required. This can be achieved by using multiple nanoribbons stacked both vertically and horizontally. The edge states in nanoribbons were recently studied by using a **k·p** theory [2,3]. Due to an interaction of the edge states, a small gap in their linear dispersion opens at small momentum [2] in a TI phase, while the transition to a normal phase happens at lower values of the normal electric fields [3]. However, it is not clear whether the **k·p** theory accurately describes the edge states.

In this work, we calculated the edge states' dispersions in nanoribbons with realistic terminations (Fig.3) with a density-functional theory (DFT) *ab initio* approach. Exchange and correlations were described using the generalized gradient Perdew-Burke-Ernzerhof (PBE) functional. The system's *k*-space was sampled on a Monkhorst pack grid of $8\times1\times1$ for geometry optimizations and $12\times1\times1$ for band structure calculations of the nanoribbons. The dispersion of the edge states is gapless for wider nanoribbons (Fig.4), while a small gap opens at intermediate widths (Fig.5). The dispersion is clearly independent of the particular edges terminations, implying that the **k·p** theory may be sufficiently accurate. For extremely narrow nanoribbons (Fig.6) a clear distinction between symmetric and asymmetric terminations becomes visible.

[1] X. Quan *et al.*, Science **346**, 1344 (2014).

[2] B. Das *et al.*, Sci. Rep. **10**, 1 (2020).

[3] V. Sverdlov *et al.*, Solid-State Electronics **184**, 108081, (2021).

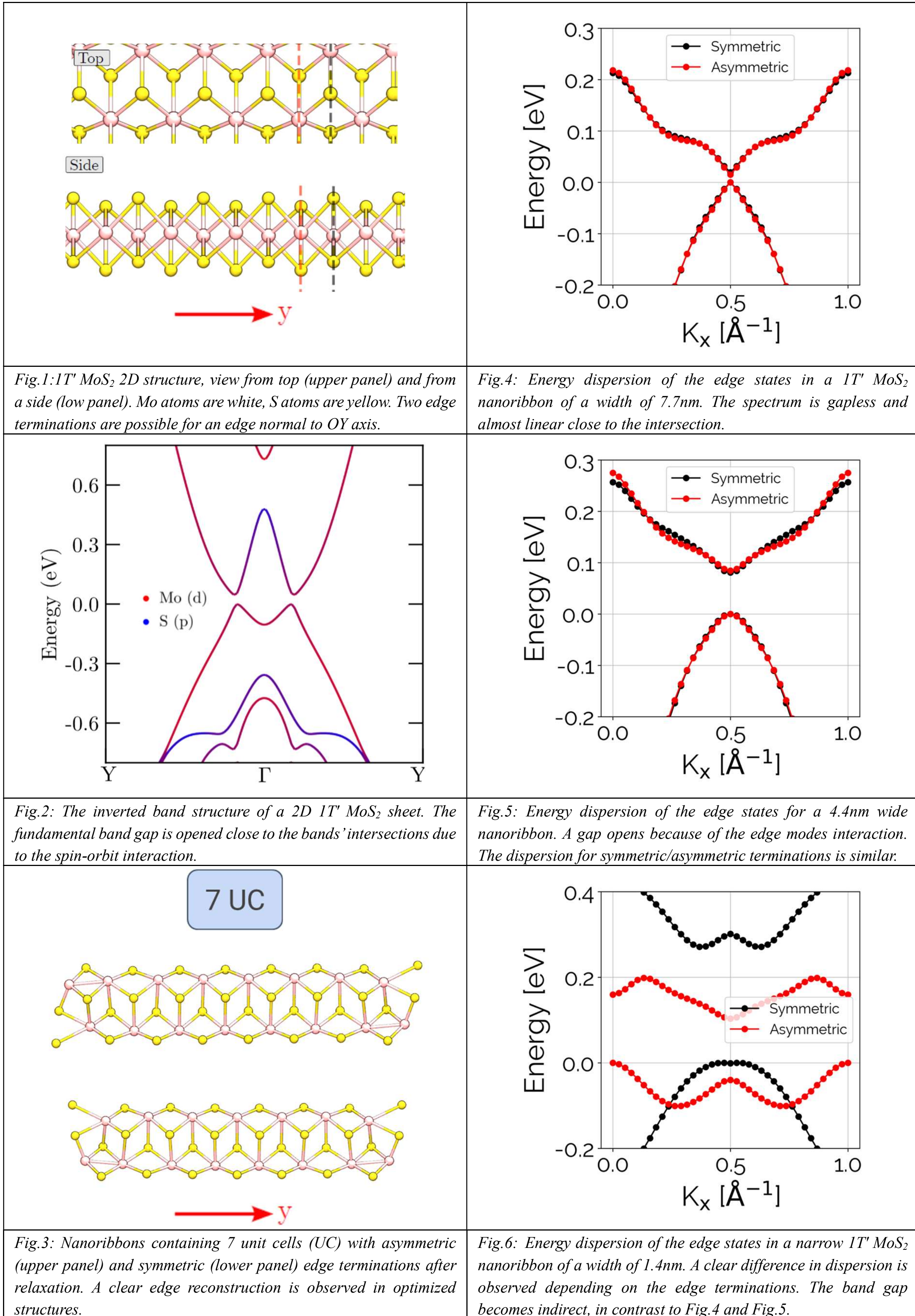

Fig.1:1T' MoS_2 2D structure, view from top (upper panel) and from a side (low panel). Mo atoms are white, S atoms are yellow. Two edge terminations are possible for an edge normal to OY axis.

Fig.2: The inverted band structure of a 2D 1T' MoS_2 sheet. The fundamental band gap is opened close to the bands' intersections due to the spin-orbit interaction.

Fig.3: Nanoribbons containing 7 unit cells (UC) with asymmetric (upper panel) and symmetric (lower panel) edge terminations after relaxation. A clear edge reconstruction is observed in optimized structures.

Fig.4: Energy dispersion of the edge states in a 1T' MoS_2 nanoribbon of a width of 7.7nm. The spectrum is gapless and almost linear close to the intersection.

Fig.5: Energy dispersion of the edge states for a 4.4nm wide nanoribbon. A gap opens because of the edge modes interaction. The dispersion for symmetric/asymmetric terminations is similar.

Fig.6: Energy dispersion of the edge states in a narrow 1T' MoS_2 nanoribbon of a width of 1.4nm. A clear difference in dispersion is observed depending on the edge terminations. The band gap becomes indirect, in contrast to Fig.4 and Fig.5.

Chiral spin textures and chiral spin-orbit torques for spintronic memories

Stuart S.P. Parkin

Max Planck Institute for Microstructure Physics, Halle (Saale) 06120, Germany

Atomically engineered magnetic heterostructures and their manipulation by current are key to several spintronic memory-storage technologies [1]. One of these is Racetrack Memory in which chiral domain walls can be moved very efficiently with current via spin-orbit torques in synthetic antiferromagnetic (SAF) racetracks [2]. The domain walls act as memory bits and are moved to read and write elements integrated into or adjacent to the racetracks. Using atomically thin “dusting” layers we have recently shown that the critical current density needed to move the domain walls can be reduced several-fold, while increasing the domain wall velocity by more than a factor of five for otherwise the same current density [3]. Racetrack Memory is non-volatile and has the potential, on the one hand, to replace the density memories today, namely hard-disk and solid-state drives and, on the other hand, the fastest, namely SRAM. The latter would be composed of a single domain wall racetrack that can be very fast (~100 ps).

Recently a zoology of complex spin textures stabilized by volume or interface Dzyaloshinskii-Moriya interactions have been discovered including, in our work, anti-skyrmions [4], elliptical Bloch skyrmions [5], two-dimensional Néel skyrmions [6] and fractional antiskyrmions [7]. We discuss our recent observation of Néel skyrmions and conventional magnetic bubbles in two distinct but closely related 2D van der Waal’s ferromagnetic compounds. SAF structures are highly promising for spintronics especially since this allows for magnetic structures that have zero net magnetization and, consequently, very small fringing magnetic fields, while, at the same time, these structures have magnetic surfaces that aid the detection of their magnetic state. Antiferromagnetic structures can have nearly zero net magnetization but are much more difficult to detect than SAFs. Highly interesting antiferromagnetic materials are those that are chiral and topological such as the family of Mn_3X (X=Ge, Sn, Sb) that have a Kagome structure. We discuss our recent work on the current induced manipulation of the antiferromagnetic order in thin epitaxial films of Mn_3Sn. In particular, we introduce the concept of seeded spin orbit torque (SSOT) that allows for the manipulation of the antiferromagnetic order, even in layers that are more than 100 nm thick. The triangular antiferromagnetic structure of Mn_3X [8] leads to highly interesting properties including an anomalous Hall effect derived from an intrinsic Berry curvature even though the magnetization is zero. Zero-moment chiral spin textures ranging from domain walls to anti-skyrmions have great promise for highly interesting spintronic technologies for Racetrack Memories and beyond.

[1] S.-H. Yang, R. Naaman, Y. Paltiel, S.S.P. Parkin, Chiral spintronics, Nat. Rev. Phys., 3 (2021) 328–343

[2] S.S.P. Parkin, S.-H. Yang, Memory on the Racetrack, Nat. Nanotechnol., 10 (2015) 195-198.
[3] Y. Guan, X. Zhou, T. Ma, R. Bläsing, H. Deniz, S.-H. Yang, S.S.P. Parkin, Increased Efficiency of Current-Induced Motion of Chiral Domain Walls by Interface Engineering, Adv. Mater., 33 (2021) 2007991.
[4] A.K. Nayak, V. Kumar, T. Ma, P. Werner, E. Pippel, R. Sahoo, F. Damay, U.K. Rößler, C. Felser, S.S.P. Parkin, Magnetic antiskyrmions above room temperature in tetragonal Heusler materials, Nature, 548 (2017) 561-566.
[5] J. Jena, B. Göbel, T. Ma, V. Kumar, R. Saha, I. Mertig, C. Felser, S.S.P. Parkin, Elliptical Bloch skyrmion chiral twins in an antiskyrmion system, Nat. Commun., 11 (2020) 1115.
[6] A.K. Srivastava, P. Devi, A.K. Sharma, T. Ma, H. Deniz, H.L. Meyerheim, C. Felser, S.S.P. Parkin, Observation of Robust Néel Skyrmions in Metallic PtMnGa, Adv. Mater., 32 (2020) 1904327.
[7] J. Jena, B. Göbel, T. Hirosawa, S.A. Díaz, T. Hinokihara, V. Kumar, I. Mertig, C. Felser, D. Loss, S. Parkin, Observation of fractional spin textures and bulk-boundary correspondence, submitted, DOI (2021).
[8] A.K. Nayak, J.E. Fischer, Y. Sun, B. Yan, J. Karel, A.C. Komarek, C. Shekhar, N. Kumar, W. Schnelle, J. Kübler, C. Felser, S.S.P. Parkin, Large anomalous Hall effect driven by non-vanishing Berry curvature in non-collinear antiferromagnet Mn_3Ge Sci. Adv., 2 (2016) e1501870.

Topology and Chirality

Claudia Felser

[1]*Max Planck Institute Chemical Physics of Solids, Dresden, Germany*
(e-mail: felser@cpfs.mpg.de)

Topology, a mathematical concept, recently became a hot and truly transdisciplinary topic in condensed matter physics, solid state chemistry and materials science. All 200 000 inorganic materials were recently classified into trivial and topological materials: topological insulators, Dirac, Weyl and nodal-line semimetals, and topological metals [1]. The direct connection between real space: atoms, valence electrons, bonds and orbitals, and reciprocal space: bands and Fermi surfaces allows for a simple classification of topological materials in a single particle picture. More than 25% of all inorganic compounds host topological bands, which opens also an infinitive play-ground for chemistry [1,2]. Beyond Weyl and Dirac, new fermions can be identified in compounds that have linear and quadratic 3-, 6- and 8- band crossings that are stabilized by space group symmetries [3]. Crystals of chiral topological materials CoSi, AlPt and RhSi were investigated by angle resolved photoemission and show giant unusual helicoid Fermi arcs with topological charges (Chern numbers) of ±2 [4]. In agreement with the chiral crystal structure two different chiral surface states are observed. A quantized circular photogalvanic effect is theoretically possible in Weyl semimetals. However, in the multifold fermions with opposite chiralities where Weyl points can stay at different energies, a net topological charge can be generated. [5]. However, chirality is also of interest for chemists [6], especially because of the excellent catalytic performance of the new chiral Fermions AlPt and PdGa [7]. The open question is the interplay between Berry curvature, chirality, orbital moment and surface states.

1. Bradlyn et al., Nature 547 298, (2017), Vergniory, et al., Nature 566 480 (2019), Xu et al. Nature 586 (2020) 702.
2. Nitesh Kumar, Satya N. Guin, Kaustuv Manna, Chandra Shekhar, and Claudia Felser, doi.org/10.1021/acs.chemrev.0c00732
3. Bradlyn, et al., Science 353, aaf5037A (2016)
4. Sanchez et al., Nature 567 (2019) 500, Schröter et al., Nature Physics 15 (2019) 759, Schröter Science 369 (2020) 179, Sessi et al, Nature Communications 11 (2020) 3507, Yao et al., Nature Communications 11 (2020) 2033
5. Dylan Rees, et al., Science Advances 6 (2020) eaba0509, Congcong Le, Yang Zhang, Claudia Felser, Yan Sun, Physical Review B 102 (2020) 121111(R), Zhuoliang Ni, et al., npj Quantum Materials volume 5 (2020) 96, Zhuoliang Ni, et al.,, Nature Communications 12 (2021) 154
6. B. Yan, et al., Nature Com. 6 (2015) 10167, Guowei Li and Claudia Felser, APL 116 (2020) 070501.
7. Qun Yang, et al., Advanced Materials 32 (2020) 1908518, Guowei Li, to be published

Depinning and Phase Transitions in 2D Charge-Density-Wave Quantum Materials – Prospects for Applications in Beyond-CMOS Electronics

A. Mohammadzadeh[1], A. Rehman[2], F. Kargar[1], S. Rumyantsev[2]and A.A. Balandin[1]

[1]Department of Electrical and Computer Engineering, Materials Science and Engineering Program, University of California, Riverside, California 92521 USA

[2]CENTERA Laboratories, Institute of High-Pressure Physics, Polish Academy of Sciences, Warsaw 01-142 Poland

E-mail: balandin@ece.ucr.edu https://balandingroup.ucr.edu

The charge-density-wave (CDW) phase is a quantum state consisting of a periodic modulation of the electronic charge density accompanied by a periodic distortion of the atomic lattice in quasi-one-dimensional (1D) or quasi-two-dimensional (2D) metallic van der Waals (vdW) crystals. Several vdW materials exhibit unusually high transition temperatures to different CDW phases, opening possibility for practical device applications. One of them, 2D 1T-TaS_2, has the CDW transition between the nearly-commensurate (NC-CDW) and the incommensurate (IC-CDW) phases at 350 K. In this talk, I will describe our recent experimental results on controlling the CDW phase transitions and transport in 2D materials [1-7]. The physical nature of the CDW switching in such devices and potential speed of the CDW devices will be discussed [6-7]. I will describe the depinning of NC-CDWs in 1T-TaS_2 thin-films at room temperature. The depinning process in 1T-TaS_2 is not accompanied by an abrupt increase in electric current – in striking contrast to depinning in the conventional CDW materials with quasi-1D crystal structure. It is explained by the fact that the current density from CDWs in 1T-TaS_2 devices is orders of magnitude smaller than the current density of the free carriers available in the discommensuration network surrounding the commensurate CDW islands. Obtained results are important for the proposed applications of the CDW devices in the beyond-CMOS electronics.

The work at UCR was supported by the U.S. Department of Energy under the contract No. DE-SC0021020 "Control of Phase Transitions in Quasi-2D CDW Quantum Materials." The work at CENTERA was supported by the European Regional Development Fund No. MAB/2018/9.

[1] G. Liu, *et al.,* Nature Nanotechnology, **11**, 845 (2016).

[2] A. K. Geremew, *et al.*, Nanoscale, **11**, 8380 (2019).

[3] A. K. Geremew, *et al.*, ACS Nano, **13**, 7231 (2019).

[4] R. Salgado, *et al.*, Appl. Phys. Express, **12**, 037001 (2019).

[5] A. K. Geremew, *et al.*, Appl. Phys. Lett., **116**, 163101 (2020).

[6] A. Mohammadzadeh, *et al.*, Appl. Phys. Lett., **118**, 093102 (2021).

[7] A. Mohammadzadeh, *et al.*, Appl. Phys. Lett., **118**, 223101 (2021).

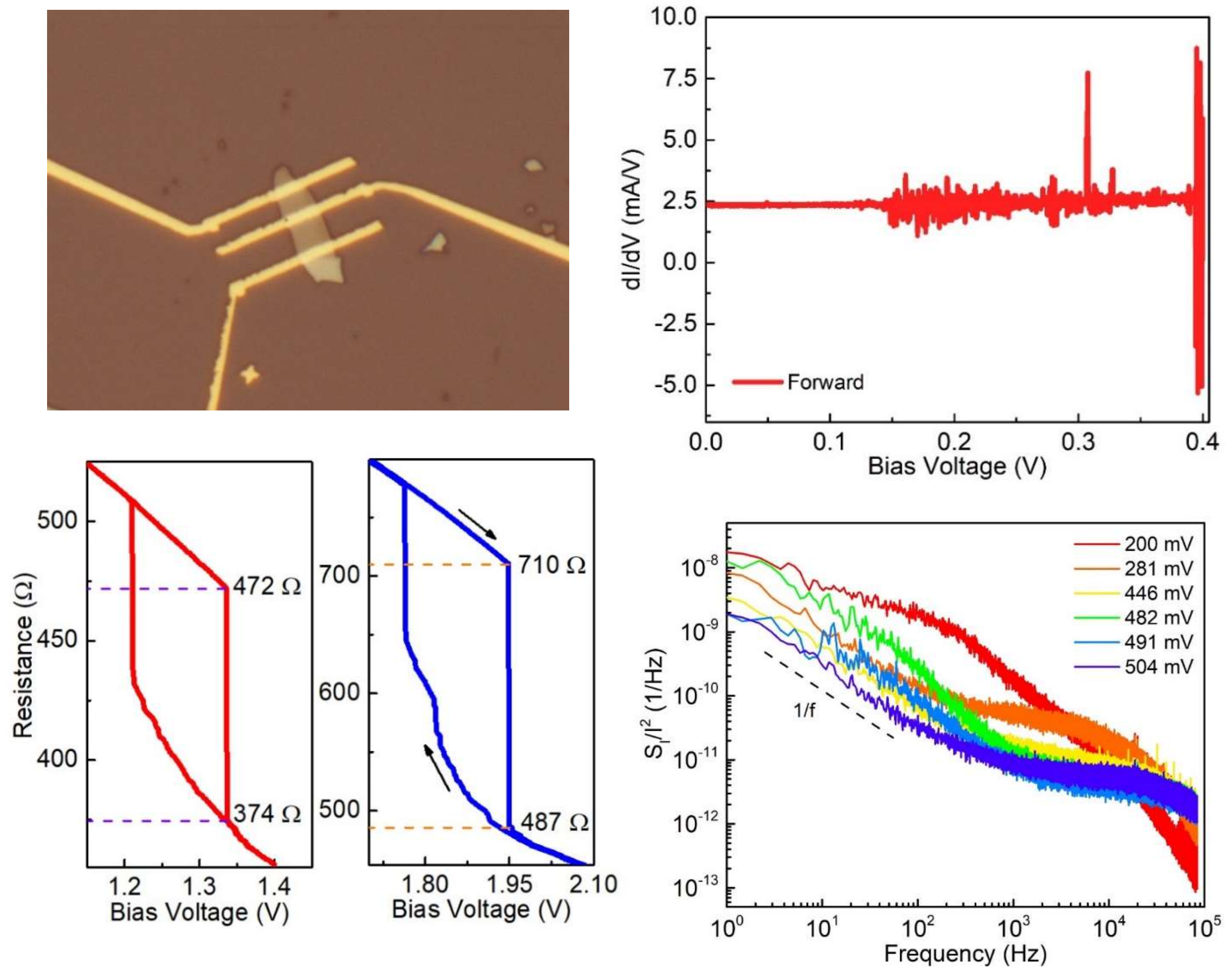

Figure: *(upper left) Optical microscopy image of the 1T-TaS_2 device (film thickness < 10 nm). The image shows two channel that constitute two devices (A and B) with the channel length of ~1.5 µm, and ~2.5 µm respectively. The width of these devices is ~3.4 µm. (lower left) The hysteresis with the abrupt change of resistance as a result of the NC-CDW to I-CDW phase transition in the 1T-TaS_2 thin film device, shown for the devices A and B. For the device A (red curve), the resistance drops from 472 Ω to 374 Ω as the voltage passes the threshold voltage. For the device B (blue curve), the threshold voltage is higher and the resistance changes from 710 Ω to 487 Ω. The CDW device operation is based on emergence of hysteresis rather than the resistance change. (upper right) The first derivative of the I-V characteristics for a representative CDW device. The depinning for this device in the forward sweeping occurs around ~0.14 V. The width of this device is ~4.0 µm. (lower right) The normalized noise spectral density as a function of frequency for different applied bias voltages near the depinning point in the log scale. Note the Lorentzian bulges, which were attributed to depinning and sliding of CDW in this quasi-2D material. A combination of the noise spectroscopy and differential I-V characteristics allow one to accurately establish the depinning point. See more details in A. Mohammadzadeh, et al., "Room-temperature depinning of the charge-density waves in quasi-2D 1T-TaS_2 devices", Appl. Phys. Lett., **118**, 223101 (2021).*

Room Temperature Higgs mode Quantum Pathway Interference in 2D Charge Density Wave materials

Yiping Wang[1], Shiming Lei[2], Leslie M. Schoop[2], Kenneth S. Burch[1]
[1]Department, Boston College, Boston, MA 02135, USA
[2]Department of Chemistry, Princeton University, Princeton, NJ 08544, USA
ks.burch@bc.edu

Quantum pathway interference is an elegant demonstration of the wave-particle duality and power of quantum mechanics to control mater. Indeed, the control of collective excitations has become a cornerstone of efforts to create new non-equilibrium states, especially in two-dimensional limit. However, the measurement and tuning of collective mode quantum properties typically requires extreme experimental conditions: low temperatures, ultrafast lasers, high magnetic and/or electric fields. Here a simple optical scheme enables interference of excitation quantum pathways of charge density wave (CDW) collective mode at room temperature. In RTe_3 (R=La, Gd), a Van der Waals combined CDW system, the Higg's (amplitude) mode can be excited via two distinct nesting vectors, that are degenerate but connect bands of similar or different angular momenta. As such, constructive or destructive interference of these pathways results from the choice of the incident and Raman scattered light polarization. Specifically, the Higgs mode is observed for incident polarization along a crystal axis with perpendicular scattered polarization but disappears upon just swapping the polarizations, while all phonons modes remain. Surprisingly we find the quantum interference is robust, existing in two different materials, at room temperature and is insensitive to the Higgs mode mixing with nearby phonons. Our results provide a straightforward means for measuring and controlling the quantum pathways of collective modes towards novel phases and quantum devices.

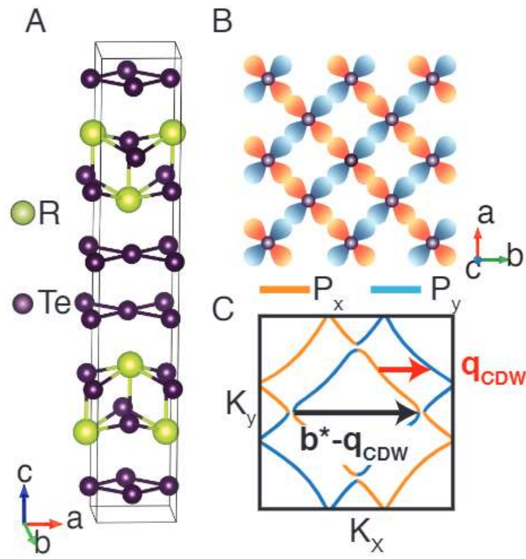

Fig.1: (A) RTe_3 crystal structure and unit cell (black line). (B) Px(orange) and Py(blue) orbitals in the Te layer. (C) Fermi surface with orbital content labeled by the same colors as in (B). The red arrow indicates the CDW vector (q_{CDW}) with the black arrow indicating the second nesting condition with the reciprocal lattice vector (b^*-q_{CDW}).

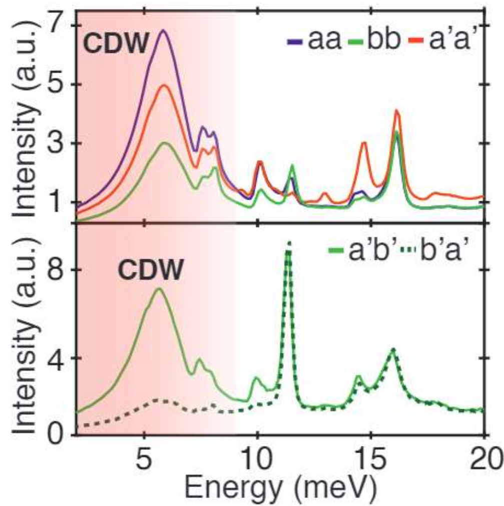

Fig.2: 300K Raman spectra of $GdTe_3$ Top plot is taken in parallel linear polarization, with incident and scattered light aligned with different crystal axis. The Higg's mode is shaded. The bottom plot is taken in cross linear polarization, for incident light aligned with a' direction and scattered light along b' direction (green solid line). Upon swapping the incident and scattered polarization (dashed line), the response of all phonons modes is identical, while the amplitude mode is suppressed.

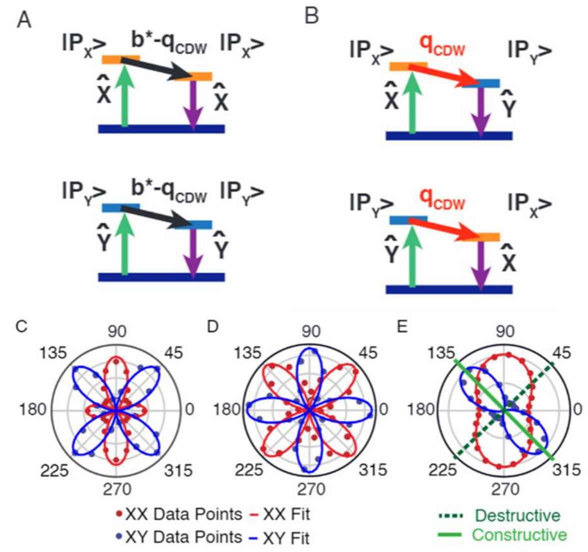

Fig.3: Interference of CDW Raman scattering quantum pathways (A) CDW involved symmetric Raman scattering process, where the CDW vector connects orbitals with the same angular momenta. (B) CDW involved anti-symmetric Raman scattering process, where the CDW vector connects different orbitals. (C-E) Angular dependence of the amplitudes of the Raman modes extracted from Voigt fits of the spectra in parallel (red dots) and cross (blue dots) linear polarization. (C) Ag mode of $GdTe_3$. (D) Bg mode of $GdTe_3$. (E) CDW mode of $GdTe_3$ revealing the constructive (green a'b') versus destructive (dashed green b'a') interference.

Two-Dimensional Semiconductors and Heterostructures for Advanced Logic, Memory and Photonics

Deep Jariwala[1]

[1]*Department of Electrical and Systems Engineering and Materials Science and Engineering, University of Pennsylvania, Philadelphia, PA-19104, U.S.A.*

e-mail: dmj@seas.upenn.edu

The isolation of a growing number of two-dimensional (2D) materials has inspired worldwide efforts to integrate distinct 2D materials into van der Waals (vdW) heterostructures. While a tremendous amount of research activity has occurred in assembling disparate 2D materials into "all-2D" van der Waals heterostructures and making outstanding progress on fundamental studies, practical applications of 2D materials will require a broader integration strategy. I will present our ongoing and recent work on integration of 2D materials with 3D electronic materials to realize logic switches and memory devices with novel functionality that can potentially augment the performance and functionality of Silicon technology. First, I will present our recent work on gate-tunable diode[1] and tunnel junction devices based on integration of 2D chalcogenides with Si and GaN. Following this I will present our recent work on non-volatile memories based on Ferroelectric Field Effect Transistors (FE-FETs) made using a heterostructure of MoS_2/AlScN[2] and I also will present our work on Ferroelectric Diode devices[3] also based on thin AlScN.

Finally, I will also provide a brief overview of our recent efforts/works in the area of photonic devices.[4-6] In particular, I will focus on our recent efforts on looking at self-hybridized exciton-polariton systems in 2D semiconductors[4,7-9] placed on plasmonic metal substrates as well as superlattices[8] made using them. I will end by giving a broad perspective on future opportunities of 2D and other low-dimensional materials in basic science and applied microelectronics technology.

References:

1. Miao, J.; Liu, X.; Jo, K.; He, K.; Saxena, R.; Song, B.; Zhang, H.; He, J.; Han, M.-G.; Hu, W.; Jariwala, D. Nano Letters 2020, 20, (4), 2907-2915.

2. Liu, X.; Wang, D.; Zheng, J.; Musavigharavi, P.; Miao, J.; Stach, E. A.; Olsson III, R. H.; Jariwala, D. Nano Letters 2021, 21, 3753–3761.

3. Liu, X.; Zheng, J.; Wang, D.; Musavigharavi, P.; Stach, E. A.; Olsson III, R.; Jariwala, D. Applied Physics Letters 2021, 118, 202901

4. hang, H.; Abhiraman, B.; Zhang, Q.; Miao, J.; Jo, K.; Roccasecca, S.; Knight, M. W.; Davoyan, A. R.; Jariwala, D. Nature Communications 2020, 11, (1), 3552.

5. Song, B.; Hou, J.; Wang, H.; Sidhik, S.; Miao, J.; Gu, H.; Zhang, H.; Liu, S.; Fakhraai, Z.; Even, J.;

Blancon, J.-C.; Mohite, A. D.; Jariwala, D. ACS Materials Letters 2021, 3, (1), 148-159.
6. Song, B.; Liu, F.; Wang, H.; Miao, J.; Chen, Y.; Kumar, P.; Zhang, H.; Liu, X.; Gu, H.; Stach, E. A.; Liang, X.; Liu, S.; Fakhraai, Z.; Jariwala, D. ACS Photonics 2020, 7, (10), 2896-2905.
7. Anantharaman, S. B.; Jo, K.; Jariwala, D., Exciton-Photonics: From Fundamental Science to Applications. ACS Nano 2021. 15, 12628–12654
8. Kumar, P.; Lynch, J.; Song, B.; Ling, H.; Barrera, F.; ‖ Zhang, H.; Kisslinger, K.; Anantharaman, S. B.; Digani, J.; Zhu, H.; Choudhury, T. H.; McAleese, C.; Wang, X.; Conran, B. R.; Whear, O.; Motala, M.; Snure, M.; Muratore, C.; Redwing, J. M.; Glavin, N.; Stach, E. A.; Davoyan, A. R.; Jariwala, D. Light-Matter Coupling in Scalable Van der Waals Superlattices. arXiv:2103.14028 Nature Nanotechnology (accepted)
9. Anantharaman, S. B.; Stevens, C. E.; Lynch, J.; Song, B.; Hou, J.; Zhang, H.; Jo, K.; Kumar, P.; Blancon, J.-C.; Mohite, A. D.; Hendrickson, J. R.; Jariwala, D. Self-Hybridized Polaritonic Emission from Layered Perovskites. Nano Letters 2021, 21, 6245-6252

Electronic Transport in Strain-Engineered Graphene

Nadya Mason
Department of Physics and Materials Research Laboratory, University of Illinois at Urbana-Champaign, Urbana IL
nadya@illinois.edu

There is wide interest in using strain-engineering to modify the physical properties of 2D materials, for both basic science and applications. Deformations of graphene, for example, can lead to the opening of band gaps, as well as the generation of pseudo-magnetic fields and novel electronic states. We demonstrate how controllable, device-compatible strain patterns in graphene can be engineered by depositing graphene on corrugated substrates. We discuss several techniques for creating corrugated substrates [1,2], focusing on periodic spherical curvature patterns in the form of closely packed nanospheres [3]. We show how the smaller nanospheres induce larger tensile strain in graphene, and explain the microscopic mechanism of this [3]. We also present experimental results demonstrating how a nearly periodic array of underlying nanospheres creates a strain superlattice in graphene[4,5], which exhibits mini-band conductance dips and magnetic field effects that depend on the magnitude of induced strain. This control of the strain degree of freedom provides a novel platform both for fundamental studies of 2D electron correlations and for prospective applications in 2D electronic devices. Work supported by NSF under *DMR-1720633* (MRSEC) and *ENG-1434147*, the ARO under *W911NF-19-1-0346,* and the UIUC Materials Research Lab.

[1] S.T. Gill *et al*, *ACS Nano* **9**, 5799 (2015).
[2] J. H. Hinnefeld *et al*, *Appl. Phys. Lett.* **112**, 173504 (2018).
[3] Y. Zhang *et al, Nano Letters* **18**, 2098 (2018).
[4] Y. Zhang *et al, njp:2D Materials and Applications* **2**, 31 (2018).
[5] Y. Zhang *et al*, *App. Phys. Lett.* **115**, 143508 (2019).

Novel Multilayer Architectures Based on Epitaxial Graphene

B. Pielić[1], C. Busse[2], K. Watanabe[3], and M. Kralj[1]
[1]*Institute of Physics, 10000 Zagreb, Croatia*
[2]*Department Physik, Universität Siegen, 57068 Siegen, Germany*
[3]*Graduate School of Science, Kyoto University, Kyoto 606-8502, Japan*
mkralj@ifs.hr

The synthesis of epitaxial graphene on silicon carbide or on transition metals, enabled insights into various fundamental properties of graphene and a development of wafer- and large-scale applications [1]. Furthermore, a quest for new materials based on lateral and vertical heterostructures (HSs) of atomically thin layers, promoted epitaxial graphene as a platform to form complex architectures and new functionalities.

In the following, we explore subsequent growth of MoS_2 and WS_2 on epitaxial graphene on Ir(111). This results in a successful heteroepitaxial formation of both lateral and vertical transition metal dichalcogenides HSs (Fig. 1). We perform an extensive analysis of the electronic structure by scanning tunneling spectroscopy (STS). In particular, we find sharp 1D interfaces with narrow depletion region exhibiting strong built-in electric fields [2].

Another example is use of epitaxial graphene (or hBN) to form special architecture of alkali metal bilayers, where intercalation and adsorption enable formation of a structure in which 2D material is sandwiched between the two alkali layers. Such structure ensures efficient electronic decoupling of the outermost layer of alkali atoms, which together with 2D material support a multipole plasmon with a dipole charge density profile, ensuring a pronounced effect of light absorption in the visible region [3]. The extreme system downsizing significantly alters the ultrafast plasmonic response, where generation of high-energy hot carries results in transient response within several tens of femtoseconds that is much faster than a typical hot-electron decay observed in other plasmonic systems [4]. In addition, the localized excitation non-thermally launches coherent surface phonons of the composite, exhibiting the plasmon band modulation in the THz frequency range. These new findings pave the way for tailoring plasmon-induced processes by the atomic scale fabrication.

[1] C. Backes, *et al.*, 2D Mater. **7**, 022001 (2020).
[2] B. Pielić, *et al.*, submitted (2021).
[3] S. Tanaka, *et al.*, Phys. Rev. Lett. **125**, 126802 (2020).
[4] S. Tanaka, *et al.*, submitted (2021).

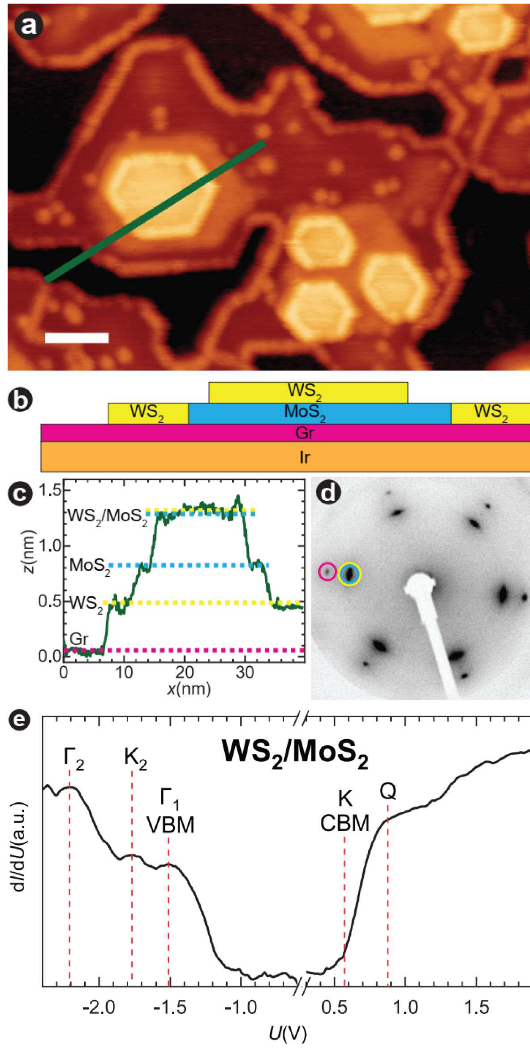

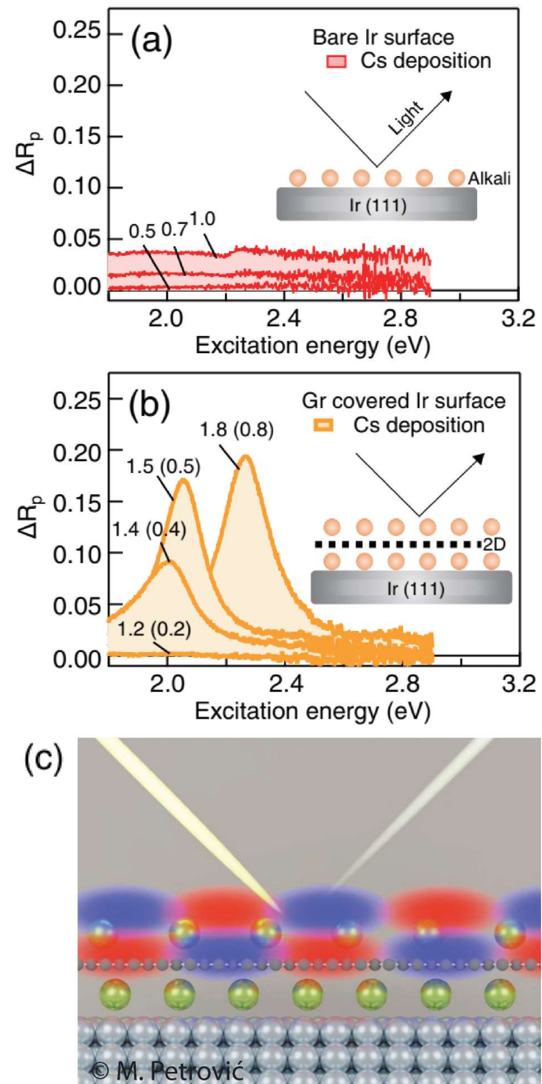

Fig.1: (a) STM topography showing WS_2/MoS_2/Gr heterostructure sample. (b) A schematic sectional view along the green line in (a). (c) STM line profile along the green line in (a) shows the apparent height difference among four characteristic areas. (d) Averaged STS spectrum of vertical heterostructure. Vertical dashed lines mark the critical energy points and band edges.

Fig.2: (a) and (b) Reflectivity changes of p-polarized light as a function of alkali coverage on clean Ir(111) surface and graphene covered Ir(111) surface. (c) A schematic visualization of multipole plasmon, which is localized on the topmost alkali and graphene layer and exhibits dipole character.

One-Dimensional van der Waals Quantum Materials as Efficient Fillers for Multifunctional Composites – Applications in Electromagnetic Shielding

Z. Barani[1], F. Kargar[1], Y. Ghafouri[2], S. Rumyantsev[3], K. Godziszewski[4], G. Cywiński[3], Y. Yashchyshyn[3,4], T.T. Salguero[2] and A.A. Balandin[1]

[1]*Department of Electrical and Computer Engineering, University of California, Riverside, California 92521 USA*

[2]*Department of Chemistry, University of Georgia, Athens, Georgia 30602 USA*

[3]*CENTERA Laboratories, Institute of High-Pressure Physics, Polish Academy of Sciences, Warsaw 01-142 Poland*

[4]*Institute of Radioelectronics and Multimedia Technology, Warsaw University of Technology, Warsaw 00-665 Poland*

E-mail: balandin@ece.ucr.edu https://balandingroup.ucr.edu

Transition metal trichalcogenides have quasi-1D crystalline structures characterized by strong covalent bonds in one dimension and weaker interactions in other dimensions. Such van der Waals materials exfoliate into needle-like structures, *i.e.,* bundles of atomic chains [1-4]. Electrical measurements established that the quasi-1D atomic chains have a breakdown current density approaching 100 MA/cm^2 [1-2]. Here, we report on the use of the chemically exfoliated quasi-1D $TaSe_3$ van der Waals metallic nanostructures as the fillers in polymer composites. These quasi-1D nanostructures are characterized by extremely large aspect ratios of up to ~10^6. The polymer composite films with low loadings of quasi-1D $TaSe_3$ fillers (<3 vol. %) revealed excellent electromagnetic (EM) interference (EMI) shielding in the X-band GHz and EHF sub-THz frequency ranges while remaining *electrically insulating*. The unique EM properties of these films are attributed to the effective coupling of the EM waves to the high-aspect-ratio electrically-conductive $TaSe_3$ fillers even at loading below the percolation threshold [3]. These novel films are promising for high-frequency communication technologies, which require flexible, lightweight, and electrically insulating EMI shielding films. We also show that such quasi-1D van der Waals materials can be used for polarization selective EMI shielding [4].

The work at UC Riverside was supported, in part, by the National Science Foundation (NSF) program Designing Materials to Revolutionize and Engineer our Future (DMREF) *via* UCR–Stanford collaborative project DMR-1921958: Data Driven Discovery of 1D van der Waals Solids. The work at CENTERA was supported by the European Regional Development Fund No. MAB/2018/9. A.A.B. also acknowledges the Vannevar Bush Faculty Fellowship (VBFF).

[1] M.A. Stolyarov, et al., Nanoscale, 8, 15774 (2016).

[2] A. Geremew, et al., IEEE Electron Device Lett., 39, 735 (2018).

[3] Z. Barani, et al., Adv. Mater., 33, 2007286 (2021).

[4] Z. Barani, et al., ACS Appl. Mater. Interfaces, 13, 21527 (2021).

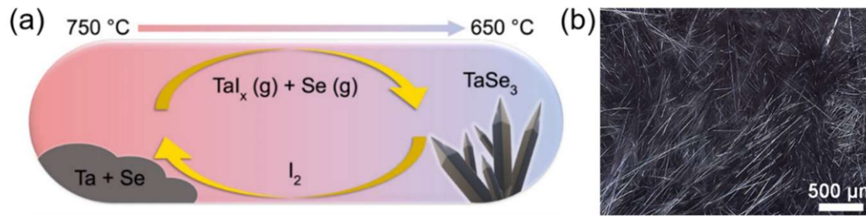

Figure 1: *(a) A schematic illustrating the iodine-mediated CVT used in this study to prepare bulk crystalline $TaSe_3$. (b) Optical image of as-synthesized $TaSe_3$ crystals.*

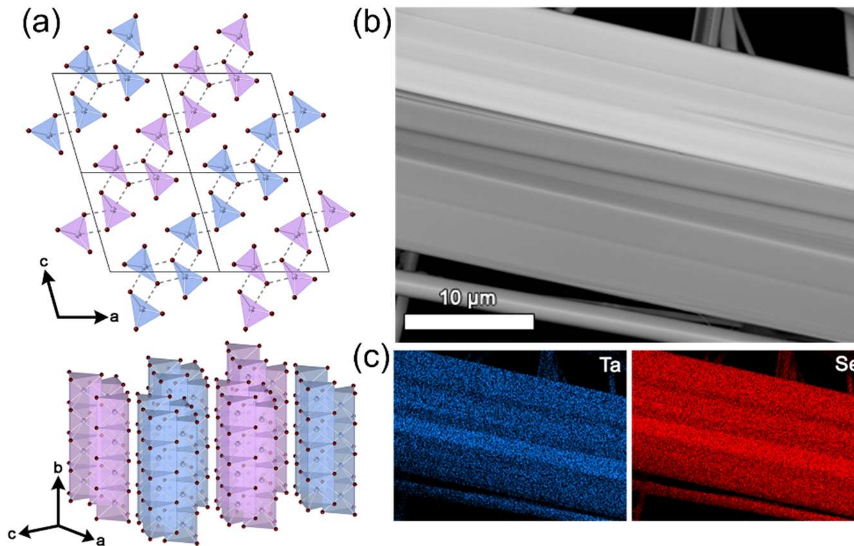

Figure 2: Structure and composition of as-synthesized $TaSe_3$. *(a) Crystal structure of $TaSe_3$; red spheres represent Se, and blue/purple spheres represent Ta. The parallelograms in the top panel outline unit cells viewed along the b-axis, perpendicular to the $TaSe_3$ chains. The side view in the bottom panel shows the quasi-1D nature of trigonal prismatic [$TaSe_6$] units extending along the b-axis. The corrugated bilayer nature of this structure is emphasized with the Ta⋯Se interchain interactions and the purple/blue coloring; bilayers are separated from their neighbors by van der Waals gaps. (b) SEM image of a mechanically-exfoliated $TaSe_3$ crystal. (c) Corresponding EDS mapping showing uniform overlap of Ta and Se along the length of the crystal.*

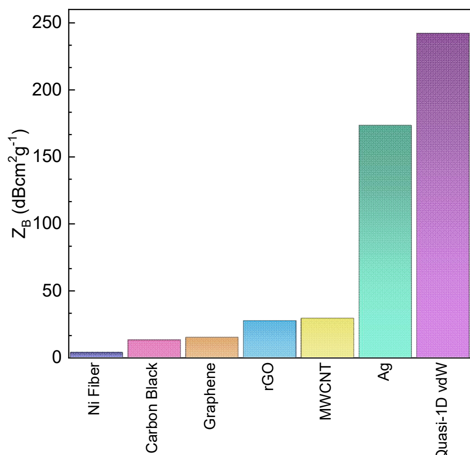

Figure 3: Comparison of EMI shielding characteristics of polymeric composites with different fillers. *The specific EMI shielding efficiency normalized by the thickness and by the filler weight loading fraction, Z_B, indicates composite's shielding effectiveness per aerial density of the filler. The lower the thickness, density, and filler weight loading fraction and higher the total shielding effectiveness, the higher the Z_B.*

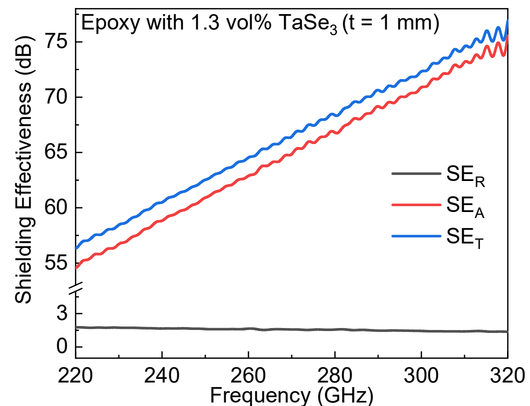

Figure 4: Electromagnetic shielding characteristics of the films with a low concentration of quasi-1D $TaSe_3$ fillers in the EHF band. *The gray, red, and blue curves are the reflection, absorption, and total shielding effectiveness of the epoxy composite with 1.3 vol% of $TaSe_3$ filler. Note that absorption is the dominant mechanism in blocking the EM waves in the EHF band.*

Observation of the Kondo screening cloud

M. Yamamoto[1] and I. V. Borzenets[2, 3]
[1]*RIKEN Center for Emergent Matter Science, Wako, Saitama 351-0198, Japan*
[2]*Department of Physics and Astronomy, Texas A&M University, Texas, USA*
[3]*Department of Physics, City University of Hong Kong, Kowloon, Hong Kong*
michihisa.yamamoto@riken.jp

When a magnetic impurity exists in a metal, conduction electrons form a spin cloud that screens the impurity spin. This basic phenomenon is called the Kondo effect. Contrary to electric charge screening, the spin screening cloud occurs quantum coherently, forming spin-singlet entanglement with the impurity. This quantum mechanical entanglement extends over the distance much longer than the charge screening length. The spatial extension of the Kondo cloud had never been observed, and its existence, a fundamental aspect of the Kondo effect, had remained as a long-standing controversial issue.

We present experimental evidence of a Kondo cloud extending over a length of micrometers comparable to the theoretical length ξ_K [1]. Our experiment was designed based on a previous theoretical proposal [2]. In our device, Kondo impurity is formed in a quantum dot (QD), one-sided coupling to a quasi-one-dimensional channel that houses a Fabry-Perot (FP) interferometer of various gate-defined lengths $L > 1$ μm. When we sweep a voltage on the interferometer end gate separated from the QD by the length L to induce FP oscillations in conductance, we observe oscillations in measured Kondo temperature T_K, a sign of the cloud at distance L. For $L < \xi_K$ the T_K oscillation amplitude becomes larger for the smaller L, obeying a scaling function of a single parameter L/ξ_K, while for $L > \xi_K$ the oscillation is much weaker. The result implies that ξ_K is the only length parameter associated with the Kondo effect, and that the cloud has the universal shape irrespective of the parameters associated with the QD. The cloud lies mostly inside the length ξ_K which reaches microns, with a long tail extending beyond ξ_K.

This work was done in collaboration with J. Shim, H.-S. Sim, J. C. H. Chen, A. Ludwig, A. D. Wieck, and S. Tarucha.

[1] I. V. Borzenets, J. Shim, J. C. H. Chen, A. Ludwig, A. D. Wieck, S. Tarucha, H.-S. Sim, and M. Yamamoto, "Observation of the Kondo screening cloud", *Nature* **579**, 210 (2020).
[2] J. Park, S.-S. B. Lee, Y. Oreg, and H.-S. Sim, "How to directly measure a Kondo cloud's length", *Phys. Rev. Lett.* **110**, 246603 (2013).

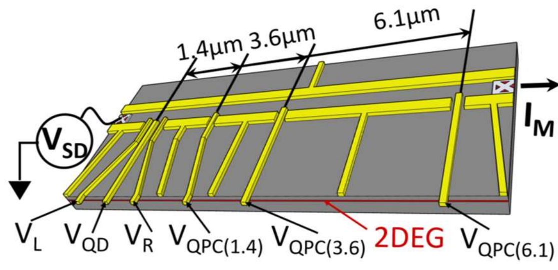

Fig.1: Schematic description of the interferometer device used to detect the Kondo cloud.

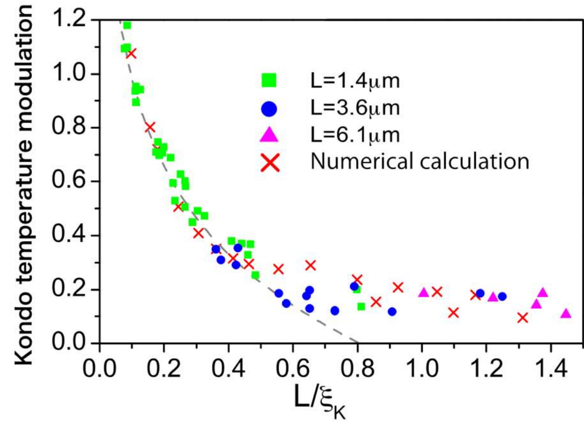

Fig.2: Shape of the Kondo cloud normalized by its size ξ_K. The cloud shape was obtained by quantitative analysis of the Kondo temperature modulation by the gate voltage V_{QPC} applied to tune the electrostatic potential at quantum point contacts.

Transport in helical Luttinger liquids in the fractional quantum Hall regime

Ying Wang[1], Vadim Ponomarenko[1,2], Zhong Wan[1], Kenneth W. West[3], Kirk W. Baldwin[3], Loren N. Pfeiffer[3], Yuli Lyanda-Geller[1], and Leonid P. Rokhinson[1,4]

[1]Depertmernt of Physics and Astronomy, Purdue University, West Lafayette, Indiana, USA

[2]Ioffe Physico-Technical Institute, Saint-Petersburg, Russia

[3]Department of Electrical Engineering, Princeton University, Princeton, New Jersey, USA

[4]Department of Electrical and Computer Engineering, Purdue University, West Lafayette, Indiana, USA

leonid@purdue.edu

Domain walls in fractional quantum Hall ferromagnets are gapless helical one-dimensional channels formed at the boundaries of topologically distinct quantum Hall (QH) liquids. Naïvely, these helical domain walls (hDWs) constitute two counter-propagating chiral states with opposite spins. Coupled to an s-wave superconductor, helical channels are expected to lead to topological superconductivity with high order non-Abelian excitations. Experimental investigation of a transport through a *single* hDWs in the $\nu = 2/3$ fractional QH regime is found to be substantially smaller than the prediction of the naïve model. Luttinger liquid theory of the system reveals redistribution of currents between quasiparticle charge, spin and neutral modes, and predicts the reduction of the hDW current. Inclusion of spin-non-conserving tunneling processes reconciles theory with experiment. The theory confirms emergence of spin modes required for the formation of fractional topological superconductivity.

Y. Wang *et al.*, Nature Communications (accepted) (2021)

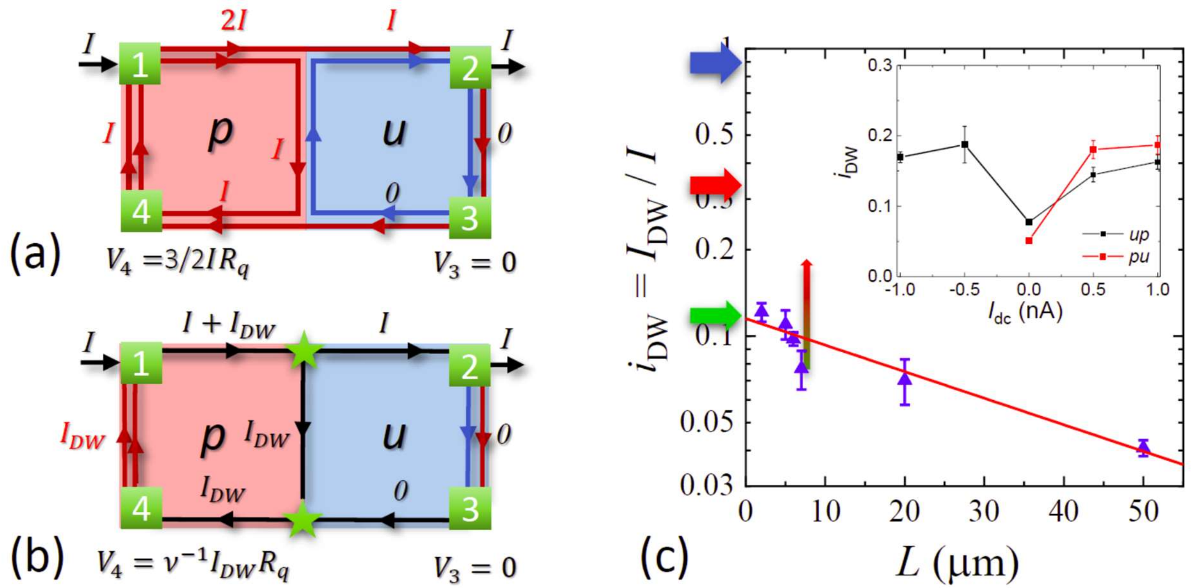

Fig. 1. **Conductance of a helical domain wall**. (a) A simplified picture of non-interacting chiral edge modes at $\nu = 2/3$. An inner spin-up edge (red) in polarized (p) state carries current I while a spin-down edge (blue) in unpolarized (u) state carries no current. (b) Charge conservation and chirality of edge states set the potential $V_4 = \nu^{-1} I_{DW} R_q$ to be proportional to the current I_{DW} diverted via the helical domain wall. (c) Scaling of the domain wall current$i_{DW} = I_{DW}/I$ with hDWs length L. Red line is a fit to an exponential decay with the $L = 0$ value $i_{DW}^0 = 0.115$ and the decay length $L_0 = 47\ \mu m$. Arrows indicate i_{DW}^0 values expected for naive non-interacting edge model (blue) and Luttinger liquid model in the absence of spin flip (red) and at spin-flip probability $r = 3/4$ (green). Vertical arrow marks i_{DW} shift when $I_{dc} = 1$ nA is applied. In the inset i_{DW} dependence on large external dc current is plotted for a $7\ \mu m$ hDW right after the dc current is applied and before a measurable build-up of nuclear polarization occurs.

Biased distributions of random quantum states for high-performance quantum state reconstruction

Sanjaya Lohani,[1,2,†] Joseph M. Lukens,[3] Daniel E. Jones,[4]
Thomas A. Searles,[1,5] Ryan T. Glasser,[2] and Brian T. Kirby[2,4]

[1]IBM-HBCU Quantum Center, Howard University, Washington, DC 20059, USA
[2]Tulane University, New Orleans, LA 70118, USA
[3]Quantum Information Science Group, Oak Ridge National Laboratory, Oak Ridge, Tennessee 37831, USA
[4]United States Army Research Laboratory, Adelphi, MD 20783, USA
[5]Massachusetts Institute of Technology, Cambridge, MA 02139, USA
† sanjaya.lohani@Howard.edu

We consider the properties of a specific distribution of mixed quantum states of arbitrary dimension that can be biased towards a specific mean purity. In particular, we analyze mixtures of Haar-random pure states with Dirichlet-distributed coefficients. We analytically derive the concentration parameters required to match the mean purity of the Bures and Hilbert--Schmidt distributions in any dimension. Numerical simulations suggest that this value recovers the Hilbert--Schmidt distribution exactly, offering an alternative and intuitive physical interpretation for ensembles of Hilbert--Schmidt-distributed random quantum states. We then demonstrate how substituting these Dirichlet-weighted Haar mixtures in place of the Bures and Hilbert--Schmidt distributions results in measurable performance advantages in machine-learning-based quantum state tomography systems and Bayesian quantum state reconstruction. Finally, we experimentally characterize the distribution of quantum states generated by both a cloud-accessed IBM quantum computer and an in-house source of polarization-entangled photons. In each case, our method can more closely match the underlying distribution than either Bures or Hilbert--Schmidt distributed states for various experimental conditions.

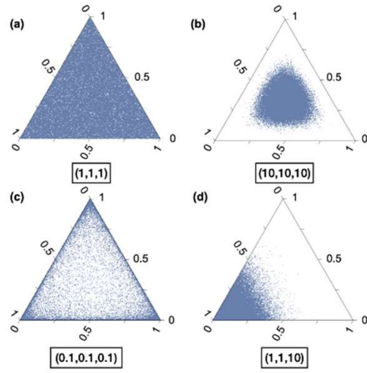

FIG. 1. Ternary plots of 10^5 Dirichlet vectors $\mathbf{x} = (x_1, x_2, x_3)$. Each plot is sampled from a distribution with a different set of concentration parameters, with (a)–(c) symmetric.

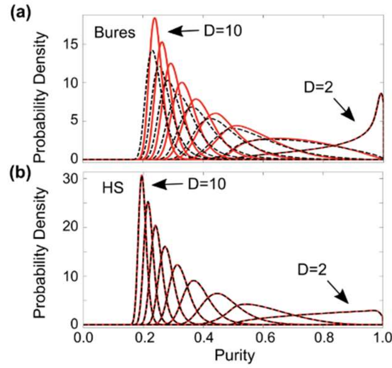

FIG. 3. Comparison of the numerically sampled probability distribution of purity for MA, Bures, and HS distributed random quantum states. Both plots show $D = K = \{2, ..., 10\}$, and each curve was created using 10^6 samples. (a) The Bures distribution is plotted with solid (red) lines, and the corresponding MA distribution with $\alpha = \alpha_B$ is plotted with dashed (black) lines. (b) The HS distribution is plotted with solid (red) line, with the corresponding MA distribution with $\alpha = \alpha_{HS}$ plotted with dashed (black) lines. We see complete overlap between the HS and MA distributions when $\alpha = \alpha_{HS}$.

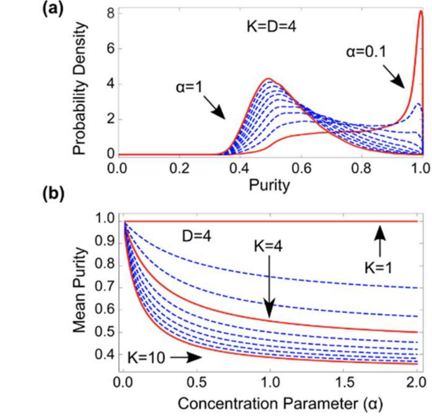

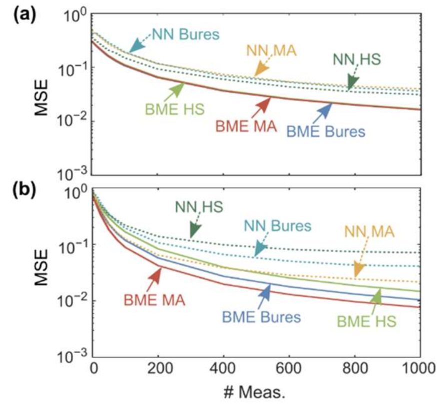

FIG. 9. Mean-squared Frobenius error $\langle D_F^2(\tilde{\rho}, \rho_g)\rangle$ for each estimation procedure. Simulated datasets from (a) Bures-drawn states and (b) Haar-random pure states. BME (neural network) results corresponding to either the Bures or MA priors (training sets) are plotted.

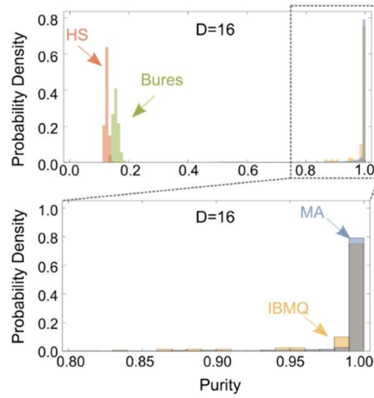

FIG. 11. Histograms comparing the Bures, HS, and MA distributions to the measured distribution of purity from the IBM Q for four-qubit quantum circuits initialized at $|0\rangle$ with no gates before tomography. The MA distribution has $D = K = 16$ and α is tuned so that the mean of the distribution matches that of the measured IBM Q distribution.

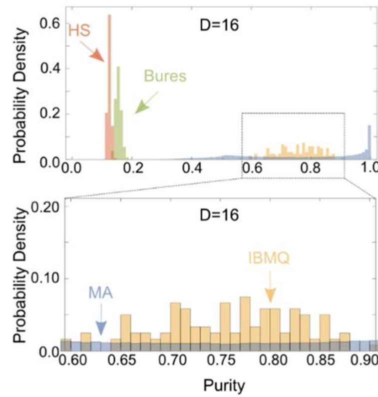

FIG. 12. Histograms comparing the Bures, HS, and MA distributions to the measured distribution of purity from the IBM Q for states resulting from random instances of the circuit shown in Fig. 10. The MA distribution has $D = K = 16$ and α is tuned so that the mean of the distribution matches that of the measured IBM Q distribution.

https://arxiv.org/abs/2107.07642

Inverse AC Josephson Effect in Ballistic Multiterminal Graphene Josephson Junctions

Ethan Arnault[1], Trevyn Larson[1], Lingfei Zhao[1], Andrew Seredinski[1], Anne Draelos[1], Takashi Taniguchi[2], Kenji Watanabe[2], Ivan V. Borzenets[3], François Amet[4], & Gleb Finkelstein[1]

[1]*Department of Physics, Duke University, Durham, NC 27708, U.S.A.*

[2]*Advanced Materials Laboratory, NIMS, Tsukuba 305-0044, Japan*

[3]*Department of Physics and Astronomy, TAMU, College Station, TX 77843, U.S.A.*

[4]*Department of Physics, Appalachian State University, Boone, NC 28607, U.S.A.*

e-mail:gleb@phy.duke.edu

In multi-terminal Josephson junctions, the superconducting coupling is established between each pair of contacts across a common normal channel. The state of such junction is described by N-1 independent phase differences between pairs of contacts, where N is the number of terminals. The added complexity makes multi-terminal junctions an ideal medium for engineering novel quantum phenomena. For example, the energy spectrum of multi-terminal Josephson junction has been predicted to effectively emulate the band structure of topologically non-trivial materials. This exciting prospect led to renewed interest toward experimental realizations of multi-terminal Josephson junctions.

Figure 1a shows a scanning electron microscope image of a three-terminal junction, in which the normal region is made of ballistic graphene encapsulated in hexagonal boron nitride. Biasing the individual junctions, we observe three superconducting branches, corresponding to pair-wise coupling between pairs of junctions (Figure 1d). We further explore the phase dynamics of these junctions when exposed to microwave radiation. The microwave drive causes inverse AC Josephson effect, which has been explored in detail in conventional Josephson junctions. In this phenomenon, the phase of the junction locks to the drive frequency, and the I−V curves acquire "Shapiro steps" of quantized voltage $V=nhf/2e$ with integer n. If the junction has three or more superconducting contacts, coupling between different pairs of terminals must be taken into account, resulting in a complicated energy landscape (Figure 1c).

Experimentally, we observe robust Shapiro steps with fractional n (Figure 2). We demonstrate that these steps cannot be attributed to non-sinusoidal current-phase characteristics of the junctions. Instead, they can be explained by considering the device as a completely connected Josephson network. We explore the stability of these steps and related phenomena, such as correlated switching events between different junctions. We successfully simulate the observed behaviors using a modified two-dimensional resistively and capacitively shunted junction model (Figure 1b). Our results suggest that multi-terminal Josephson junctions may be a highly-tunable playground for possible applications in quantum information processing.

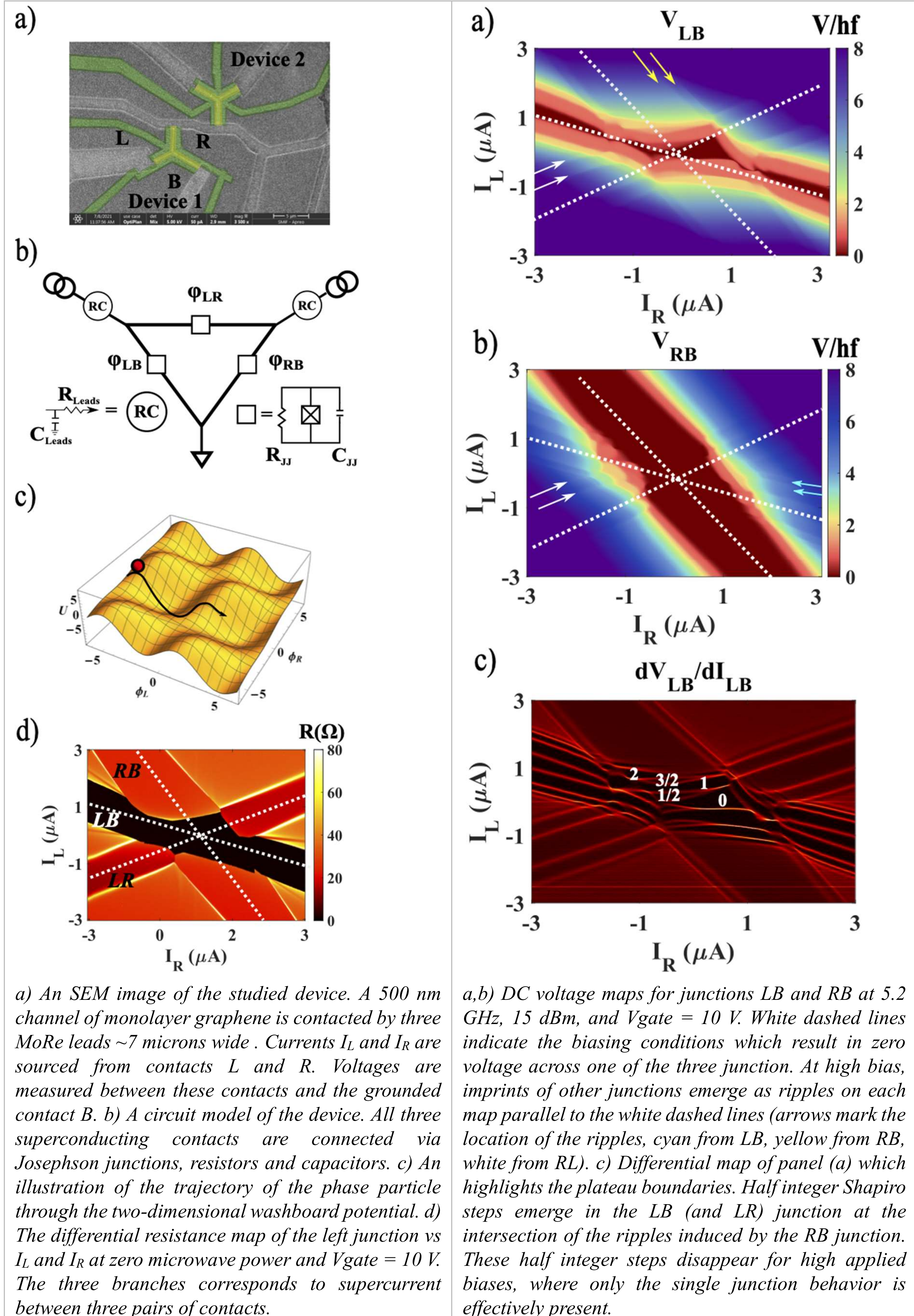

a) An SEM image of the studied device. A 500 nm channel of monolayer graphene is contacted by three MoRe leads ~7 microns wide . Currents I_L and I_R are sourced from contacts L and R. Voltages are measured between these contacts and the grounded contact B. b) A circuit model of the device. All three superconducting contacts are connected via Josephson junctions, resistors and capacitors. c) An illustration of the trajectory of the phase particle through the two-dimensional washboard potential. d) The differential resistance map of the left junction vs I_L and I_R at zero microwave power and Vgate = 10 V. The three branches corresponds to supercurrent between three pairs of contacts.

a,b) DC voltage maps for junctions LB and RB at 5.2 GHz, 15 dBm, and Vgate = 10 V. White dashed lines indicate the biasing conditions which result in zero voltage across one of the three junction. At high bias, imprints of other junctions emerge as ripples on each map parallel to the white dashed lines (arrows mark the location of the ripples, cyan from LB, yellow from RB, white from RL). c) Differential map of panel (a) which highlights the plateau boundaries. Half integer Shapiro steps emerge in the LB (and LR) junction at the intersection of the ripples induced by the RB junction. These half integer steps disappear for high applied biases, where only the single junction behavior is effectively present.

Overdamped Phase Diffusion in hBN Encapsulated Graphene Josephson Junctions

I. V. Borzenets[1,2], J. Tang[2] , M.T. Wei[3] , A. Sharma[2] , E. G. Arnault[4] , A. Seredinski[5] , Y. Mehta[5] , K. Watanabe[7] , T. Taniguchi[7] , F. Amet[6], G. Finkelstein[4]

[1]*Department of Physics and Astronomy, Texas A&M University, College Station, TX 77843, USA.*

[2]*Department of Physics, City University of Hong Kong, Kowloon, Hong Kong SAR.*

[3]*Joint Quantum Institute, University of Maryland, MD 20742, USA.*

[4]*Department of Physics, Duke University, Durham, NC 27708, USA.*

[5]*Department of Sciences, Wentworth Institute of Technology, Boston, MA 02115, USA.*

[6] *Dept. of Physics and Astronomy, Appalachian State University, Boone, NC 28607, USA.*

[7]*Advanced Materials Laboratory, National Institute for Materials Science, Tsukuba, 305-0044, Japan*

We investigate the zero-bias behavior of Josephson junctions made of encapsulated graphene boron nitride heterostructures in the long ballistic junction regime[1,2]. For temperatures down to 2.7K, the junctions appear non-hysteretic with respect to the switching and retrapping currents I_C and I_R. A small non-zero resistance is observed even around zero bias current, and scales with temperature as dictated by the phase diffusion mechanism[3]. By varying the graphene carrier concentration we are able to confirm that the observed phase diffusion mechanism follows the trend for an overdamped Josephson junction[1]. This is in contrast with the majority of graphene-based junctions which are underdamped and shorted by the environment at high frequencies[3]. This is the first conclusive confirmation of overdamped behavior in graphene-based Josephson junctions.

[1] J. Tang *et al.*, arXiv:2011.04142 (2020).
[2] I. V. Borzenets *et al.*, Phys. Rev. Lett. **117**, 237002 (2016).
[3] I. V. Borzenets *et al.*, Phys. Rev. Lett. **111**, 027001 (2013).

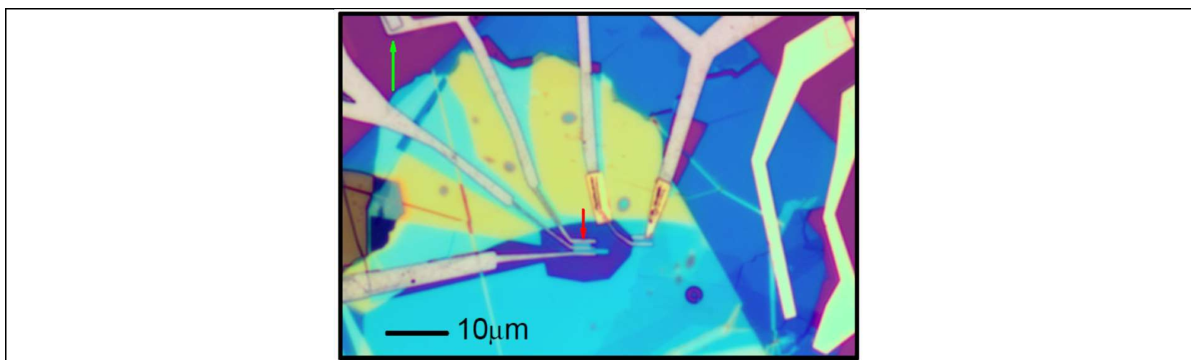

Fig.1: Optical image of the a overdamped graphene Josephson junctions device. (Scale bar presented for reference). Graphene encapsulated in hexagonal boron-nitride (hBN) acts as the normal metal portion of the device. The superconductor is made from MoRe alloy, with the superconducting leads dening a junction of 500nm length. The MoRe leads terminate about 50 microns past the active area of the device. (The bonding pads and leads connecting to the MoRe region are made of Cr/Au, thickness 5nm/110nm). An example of the transition between MoRe and Cr/Au is highlighted by the green arrow. The red arrow highlights the graphene portion of the device.

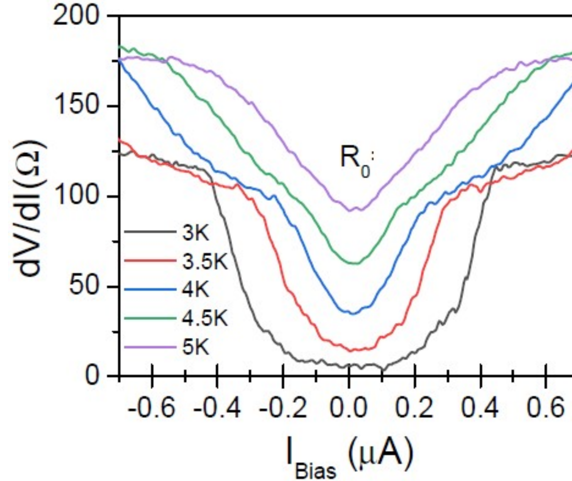

Fig.2: Differential resistance dV=dI as function of DC bias current I_{Bias}. The current is swept from negative to positive. The gate voltage here is set to 35V. All curves feature a measurable resistance even at zero bias current. This zero-bias resistance R_0 arises from the phase diffusion mechanism.

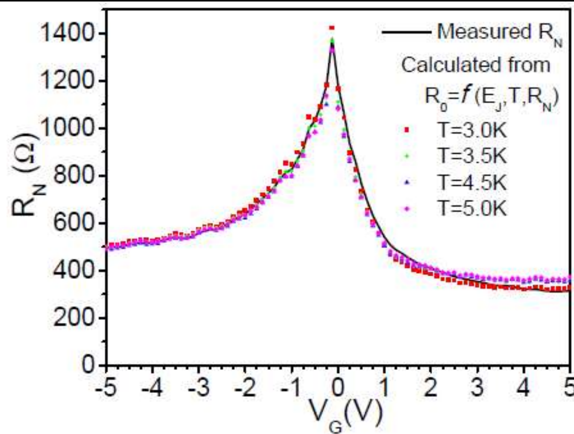

Fig.3: Gate voltage dependence of measured normal resistance R_N (black line) compared to the resistance calculated from the theoretically predicted relationship between R_N and R_0 for overdamped junctions

Substitutional or Charge Transfer Doping of Diamond for High Current PIN Diodes and Dielectric Diamond Channel Structures

Robert J. Nemanich[1*], Harshad Surdi[3], Mohamadali Malakoutian[2,4], Yu Yang[1], Yichen Yao[1], Xingye Wang[1], Franz A. Koeck[1], Srabanti Chowdhury[4], Stephen Goodnick[3],

[1]Department of Physics, Arizona State University, Tempe, AZ 85287-1504,
[2]Department of Electrical and Computer Engineering, Univ. of California, Davis, CA 95616,
[3]School of Electrical, Computer and Energy Eng., Arizona State Univ., Tempe, AZ 85287-9309,
[4]Department of Electrical Engineering, Stanford University, Stanford CA 94305

*Email: robert.nemanich@asu.edu

Diamond is a semiconductor with extreme and unique properties, which enable applications for high power and high frequency electronics. The availability of high-quality diamond substrates and the development of plasma CVD of epitaxial doped and undoped diamond have enabled fabrication of PIN diodes with high breakdown field. Substitutional doping with boron and phosphorus can achieve p-type and n-type character, respectively. Highly doped layers > 10^{19} cm^{-3} demonstrate low resistance through hopping conduction.

Epitaxial diamond PIN diodes show high current density injection mode transport described as space charge limited current. The unipolar hole current density through a Schottky diode intrinsic drift layer shows a V^2 dependence (Fig. 1) as described by the Mott-Gurney expression where the differential resistance decreases as the voltage increases. Similarly, the differential resistance of a p-i-n diode shows a greater decrease of on-resistance with V indicative of bipolar conductivity modulation.

Interface transfer doping has been used to achieve a hole accumulation layer at dielectric-diamond interfaces. Low sheet resistances between 2 and 20 kOhm/sq have been reported, and high voltage and high frequency lateral field effect transistors (FET) have been demonstrated using transfer doping at the dielectric-diamond interfaces. In this study Al_2O_3 interlayers of 2 and 4 nm thickness are employed between the charge transfer dielectric MoO_3 and diamond. The band alignment (Fig. 2) is determined using *in situ* XPS, and the charge transfer to the Al_2O_3 and the MoO_3 layers is deduced. Hall measurements establish the charge density and Hall mobility (Fig. 3). The results establish that the Al_2O_3 layer can affect the hole mobility.

The results presented here suggest a strategy for further improvement of the diamond dielectric interface for high power, high frequency FETs. Displacement of the negative charge away from the diamond interface has the potential to reduce the interface scattering. This implies using a high quality interlayer with a lower trapped charge density than Al_2O_3. However, to maintain a high density hole accumulation layer it will be necessary to maximize the charge transferred to the dielectic and a high electron affinity material would be appropriate since the charge transfer is projected to depend on the position of the transfer states below the diamond valence band. In addition, a high dielectric constant of the interlayer will also lead to increased charge density

Acknowledgement: financial support by DOE through the ULTRA EFRC (space charge limited transport) and the NSF (dielectric-diamond interfaces).

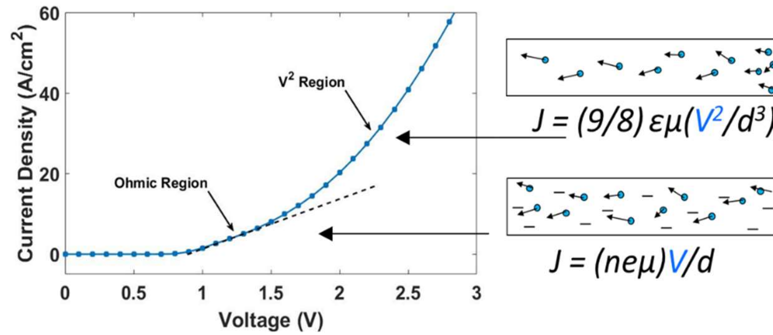

Figure 1. The forward current density-voltage (J/V) characteristics of a diamond p+/ i /metal diode. The figures indicate hole transport in the ohmic and injection regime. The exponential turn-on due to the Schottky barrier occurs below 0.6 V and is not visible in this plot. The upper equation is the Mott-Gurney expression and the lower expression is ohmic conduction where ε the permittivity, μ the carrier mobility, n the carrier density, d the intrinsic thickness.

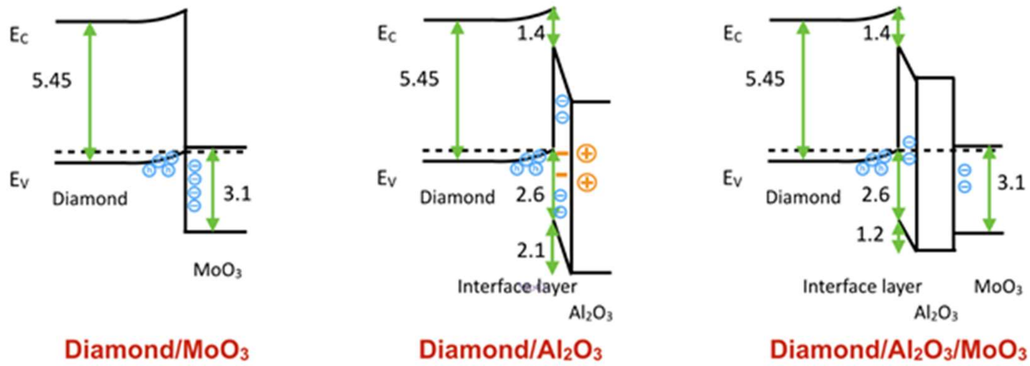

Figure 2. Band diagrams deduced from XPS measurements for MoO_3 on diamond (no interface layer), Al_2O_3 on diamond after H-plasma treatment, and MoO_3 on diamond with a 4 nm Al_2O_3 interlayer. In all three cases the bands bend upward characteristic of surface conductivity and a hole accumulation layer.

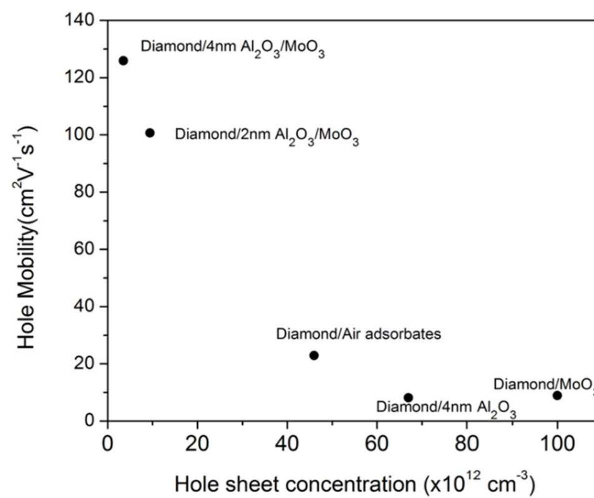

Figure 3. Hall mobility and sheet concentration for the diamond/MoO_3 and diamond/Al_2O_3/MoO_3 configurations.

High-Power Diamond Schottky P-I-N Diodes for Non-Linear RF Applications

V. Jha[1], H. Surdi[1], F. A. Koeck[2], R. J. Nemanich[2], S. M. Goodnick[1], and T. J. Thornton[1]

[1] *School of ECEE, Arizona State University, Tempe, Arizona 85287, USA*

[2] *Department of Physics, Arizona State University, Tempe, Arizona 85287, USA*

With the highest thermal conductivity of any known material, diamond is a promising ultra-wide bandgap (UWBG) material for high power electronic systems that require efficient heat dissipation. An early insertion point for diamond electronics will be non-linear RF passive systems such as high-power receiver protectors and mixers. Our previous work has shown that receiver protectors based on diamond Schottky p-i-n diodes can provide 14 dB of input power attenuation and an off-state insertion loss of 0.3 dB [1], with the potential for input protection up to >100 W of RF power [2]. Here we present, for the first time, measurements and simulations of Schottky p-i-n diodes for high-power mixer applications. Fig 1 shows a schematic cross-section of the diode with the diamond layers grown by plasma enhanced chemical deposition [2]. Figures 2 and 3 show the measured current-voltage characteristics along with the simulated results using a compact sub-circuit SPICE model [2]. With the diode configured as a shunt impedance across 50 Ohm transmission lines the model reproduces the measured small-signal S-parameters from 45 MHz to 25 GHz across a wide range of applied bias as shown in Fig. 4. A large-signal, single-tone was applied to the diode shunt to characterize the non-linear behavior. Fig. 5 shows the harmonics that appear at the 50 Ω load for increasing input power levels. It is evident that as the input power increases beyond +20dBm, the second, third and fourth harmonics start to grow significantly in the output signal. Application of a two-tone input comprising a local oscillator (LO) signal at 1.05 GHz and an RF signal at 0.95 GHz produces a down-converted intermediate frequency (IF) signal of 100 MHz. For an LO power level of +27 dBm and RF level of -2 dBm, the achieved conversion loss for this single ended diode mixer is approximately 14 dB, see Fig. 6. The IIP3 was found to be 35dBm, comparing well to 31 dBm for a SiC Schottky diode mixer [3]. The underlying physics required to maximize the diamond p-i-n diode performance will be discussed, along with pathways to minimize their specific contact resistance, and optimize other parameters that impact RF power device figures of merit.

[1] H. Surdi, *et al.*, IEEE Micro. and Wireless Compt. Letts, vol. 30, pp. 1141-1144, 2020.

[2] V. Jha, *et al.* Solid-State Electronics, vol. 186, article 108154, 2021.

[3] J. Eriksson, *et al.*, Electronics Letts, vol. 37, pp. 54-55, 2001

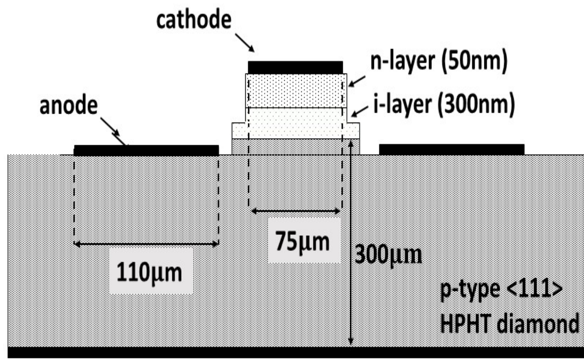

Fig.1: Schematic cross-section of the diamond Schottky p-i-n diode. The devices are electrically isolated by a partial etch that finishes within the high resistance i-layer. A second, deeper etch is used to make contact to the p-type substrate from the top surface.

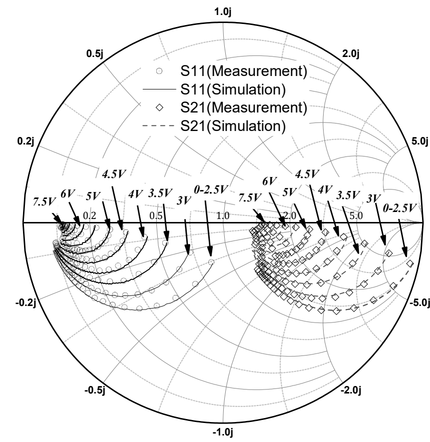

Fig.4: Measured and simulated S-parameters from 0.1 to 25 GHz for different bias voltages. The Smith chart is normalized to 50Ω.

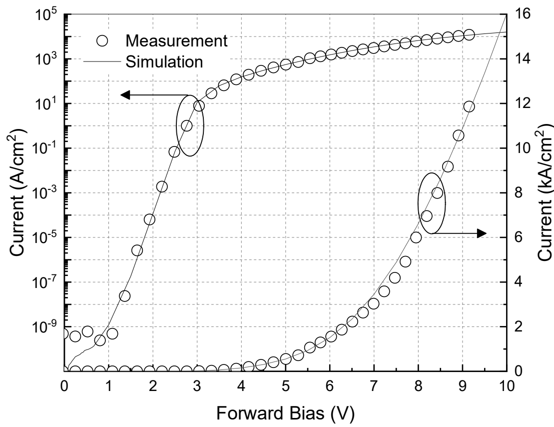

Fig.2: Forward bias I-V characteristics on logarithmic and linear scales. The solid lines represent the simulated SPICE model fit [2].

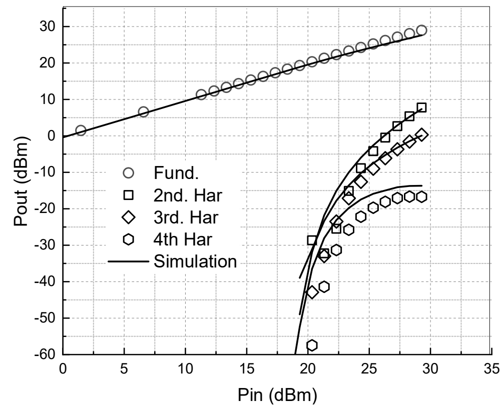

Fig.5 Measured harmonic frequencies for a single tone input at 1 GHz. The SPICE model described in [2] reproduces the output harmonics with reasonable agreement - solid lines.

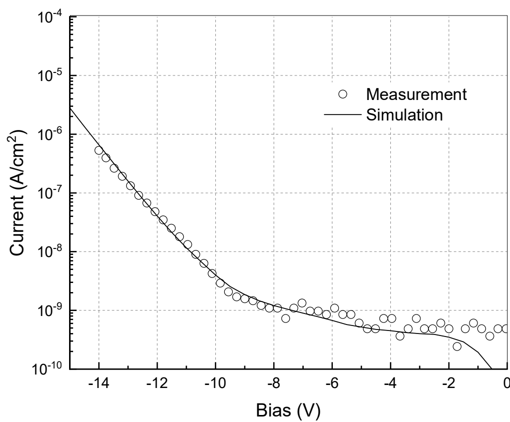

Fig.3: Reverse bias I-V characteristics. The solid lines represent the simulated SPICE model fit [2].

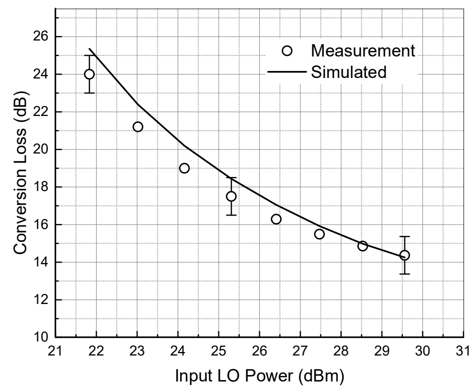

Fig.6: Conversion loss of the 100 MHz IF signal vs. input LO power. The RF power was fixed at +14 dBm. The solid lines represent the simulated SPICE model fit [2].

Low-Field Electron Mobility in AlGaN/GaN Nano-FinFETs

Viswanathan Naveen Kumar[1], Dragica Vasileska[1] and Michael Povolotskyi[2]
[1]*School of ECEE, Arizona State University, Tempe, AZ, USA*
[2]*Jacobs Corporation, Hanover, MD, USA*

Recent advances in material processing, high aspect ratio epitaxial growth and etching methods [1] have led to an increased interest in 3D nanostructures such as FinFETs and Nanowire FETs. GaN FinFETs offer an alternative topology as compared to the conventional HEMTs. The presence of gates along the sidewall of the GaN FinFETs help in depleting the 2DEG channel laterally. Lateral strain relaxation at the AlGaN/GaN interface has also been demonstrated in GaN nanostructures [2], thus leading to reduction in the polarization field. These factors may enable the realization of E-mode operation of GaNFETs.

Although carrier transport has been extensively studied in GaN HEMTs, there is a dearth of literature pertaining to their FinFET counterparts. In this work, the low field electron mobility is determined by solving the Boltzmann transport equation in the Quasi-1D region of a GaN FinFET. Three electron-phonon scattering mechanisms (acoustic, piezoelectric and polar optical phonon scattering) and interface-roughness scattering at the AlGaN/GaN interface are considered in our theoretical model. The overlap integrals are calculated using the electron wavefunctions in the Q1D region from the 2D Schrödinger-Poisson solver. The electron mobility at T=300 K increases as a function of the electron line density in the Q1D region. Such behavior may be explained using the results for the effective electric field in the growth direction (E_{eff}) and the average distance of electrons from the AlGaN/GaN hetero interface (y_{avg}). We find that E_{eff} is almost invariant with the electron line density, whereas y_{avg} increases with increasing the line density. This leads to a reduction in the interface roughness scattering and a corresponding increase in the electron mobility. Reduction in lateral strain reduces the piezoelectric polarization and hence the electron line density for a given gate bias. A reduction in the polarization field also reduces the interface roughness scattering, leading to an increase in the electron mobility.

[1] Ki-Sik Im *et al.*, *Solid-State Electronics* **97**, pp. 66-75, 2014.
[2] M. F. Fatahilah *et al.*, *Micro Nano Eng.* **3**, pp. 59–81, 2019.

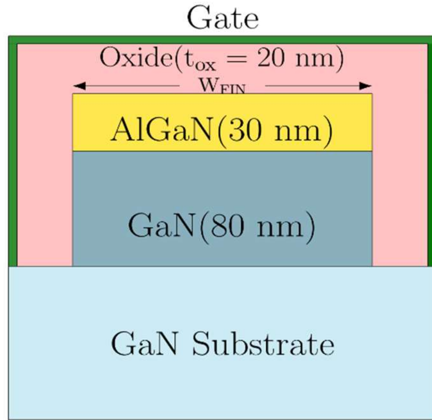

Fig. 1 Cross section of the AlGaN/GaN MIS FinFET studied in this work.

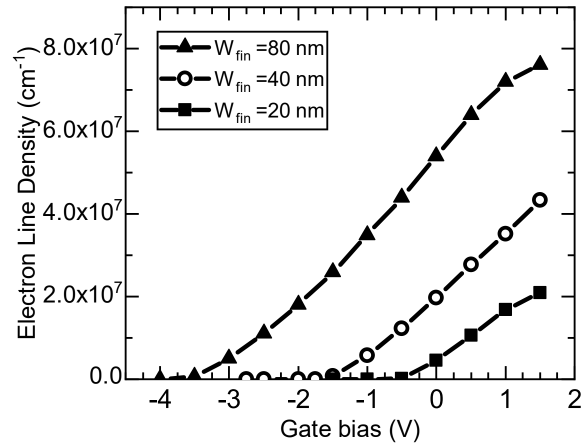

Fig. 2 Electron line density in the FinFET Q1D region as a function of gate bias V_G. The threshold voltage increases with decreasing fin width due to the appearance of lateral channels.

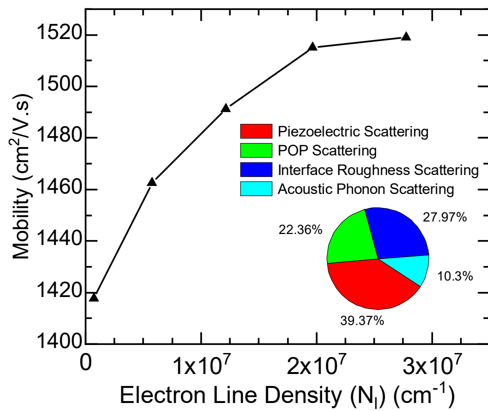

Fig. 3 Electron mobility as a function of electron line density for a 40 nm wide FinFET at T=300K. The inset pie chart shows the contribution of individual scattering mechanisms for V_G = 0 V. T = 300K.

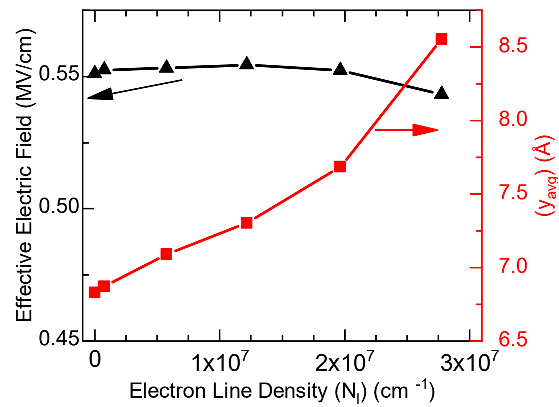

Fig. 4 Effective electric field in the growth direction (left) and the average electron separation from the AlGaN/GaN interface (right) plotted as a function of electron line density. T=300K.

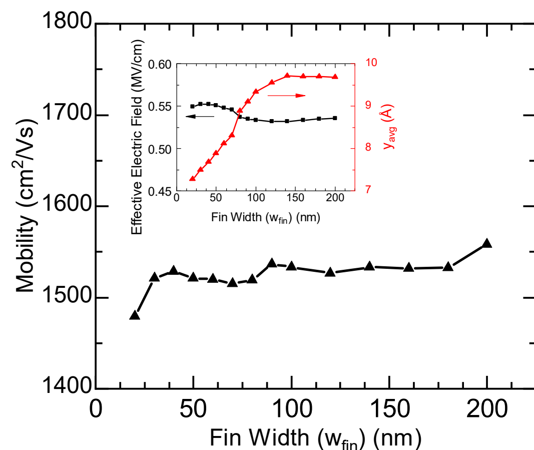

Fig. 5 Variation of electron mobility with fin width. Inset plot of effective electric field and y_{avg} shows a transition from Q1D to Q2D system as fin width increases. V_G = 0 V in the analysis.

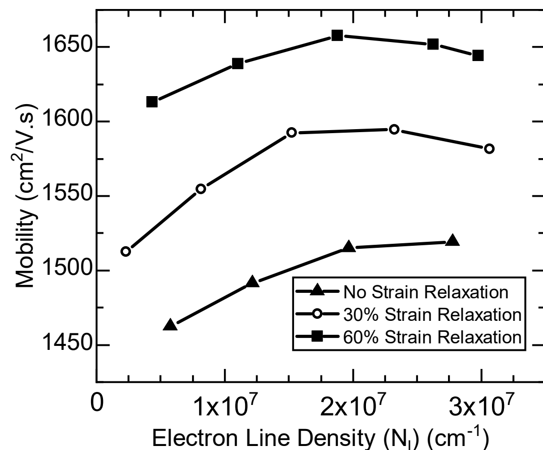

Fig. 6 Electron mobility as a function of the electron line density. Parameter in these curves is the relaxation of the lateral strain at the AlGaN/GaN heterointerface. T=300K.

978-3-9504738-3-4

Impact Ionization and Breakdown in Ultra-Wide Bandgap Materials

Jonah Shoemaker[1], Reza Vatan[1], Robert Nemanich[1], Robert Kaplar[2], Stephen Goodnick[1]
[1]*Department of Electrical Engineering, Arizona State University, Tempe, AZ, USA*
stephen.goodnick@asu.edu
[2]*Sandia National Laboratories, Albuquerque, NM, USA**

A major advantage of ultra-wide band gap (UWBG) materials for power electronic applications are the predicted high breakdown voltages limited by avalanche breakdown due to impact ionization. However, experimental data on the impact ionization coefficients in these new class of materials is limited, with a high variability in critical field based on material quality. Understanding of the fundamental limits on impact ionization is therefore critically important in assessing the potential performance for high voltage high temperature devices. In the present paper, we report on first principles calculation of the impact ionization rate and impact ionization coefficient in diamond and other UWBG materials, and associated critical field in high voltage diodes.

The full band (Fig. 1) impact ionization transition rate for an initial hot carrier with wave vector $\boldsymbol{k}_{1i}$ is given by Fermi's golden rule (including energy conservation):

$$\frac{1}{\tau(\boldsymbol{k}_{1i}, n)} = \frac{2\pi}{\hbar}\frac{V}{(2\pi)^3}\sum_{n_{1f},n_{2i},n_{2f}}\iiint d\boldsymbol{k}_{1f}d\boldsymbol{k}_{2i}d\boldsymbol{k}_{2f}|M(n_{1i},\boldsymbol{k}_{1i},n_{1f},\boldsymbol{k}_{1f},n_{2i},\boldsymbol{k}_{2i},n_{2f},\boldsymbol{k}_{2f})|^2$$

$\boldsymbol{k}_{1f}$, $\boldsymbol{k}_{2i}$ and $\boldsymbol{k}_{2f}$ are the wave vectors of the hot carrier final state and ionized carrier initial and final states, respectively. M is the screened Coulomb matrix element, given by $|M|^2 = |M_D|^2 + |M_E|^2 - (M_D^* M_E + M_D M_E^*)/2$. The direct matrix element M_D is

$$M_D = \sum_{\boldsymbol{G}_{1i},\boldsymbol{G}_{2i},\boldsymbol{G}_{1f},\boldsymbol{G}_{2f}} a^*_{n_{1f}\boldsymbol{k}_{1f}}(\boldsymbol{G}_{1f})a^*_{n_{2f}\boldsymbol{k}_{2f}}(\boldsymbol{G}_{2f})\,a_{n_{1i}\boldsymbol{k}_{1i}}(\boldsymbol{G}_{1i})a_{n_{2i}\boldsymbol{k}_{2i}}(\boldsymbol{G}_{2i})$$
$$\times\frac{e^2}{4\pi\varepsilon(\boldsymbol{q}_D,\omega_D)q_D^2}\delta\big(\boldsymbol{k}_{1i}+\boldsymbol{G}_{1i}+\boldsymbol{k}_{2i}+\boldsymbol{G}_{2i}-\boldsymbol{k}_{1f}-\boldsymbol{G}_{1f}-\boldsymbol{k}_{2f}-\boldsymbol{G}_{2f}\big)$$

where $\boldsymbol{q}_D = \boldsymbol{k}_{1f} + \boldsymbol{G}_{1f} - \boldsymbol{k}_{1i} - \boldsymbol{G}_{1i}$ and the transfer frequency is $\omega_D = \big(E(\boldsymbol{k}_{1i}) - E(\boldsymbol{k}_{1f})\big)/\hbar$. The full wave vector and frequency dependent dielectric function is calculated from the Lindhard dielectric function, giving the energy averaged electron and hole rates (Fig. 2).

The impact ionization coefficient is calculated from full band cellular Monte Carlo (CMC) simulation as shown in Fig. 3. The effect of different electron-phonon deformation potentials shows a strong sensitivity of the impact ionization coefficient and critical field on the assumed deformation potentials, and work is currently underway to calculate such potentials for various UWBG materials from first principles.

*Sandia National Laboratories is managed and operated by NTESS under DOE NNSA contract DE-NA0003525.

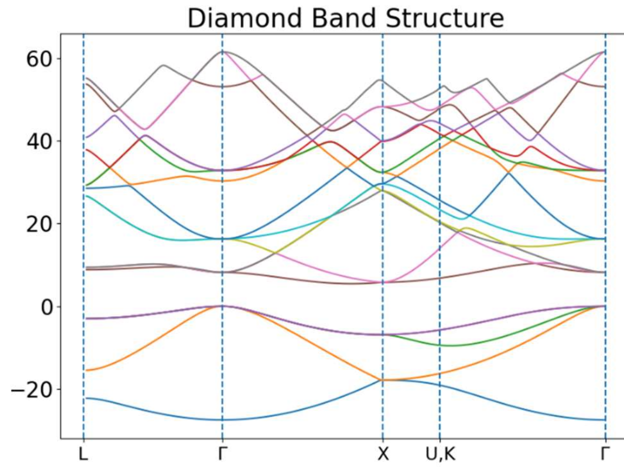

Fig.1: Empirical pseudopotential band structure of diamond, 12 nearest shell sets.

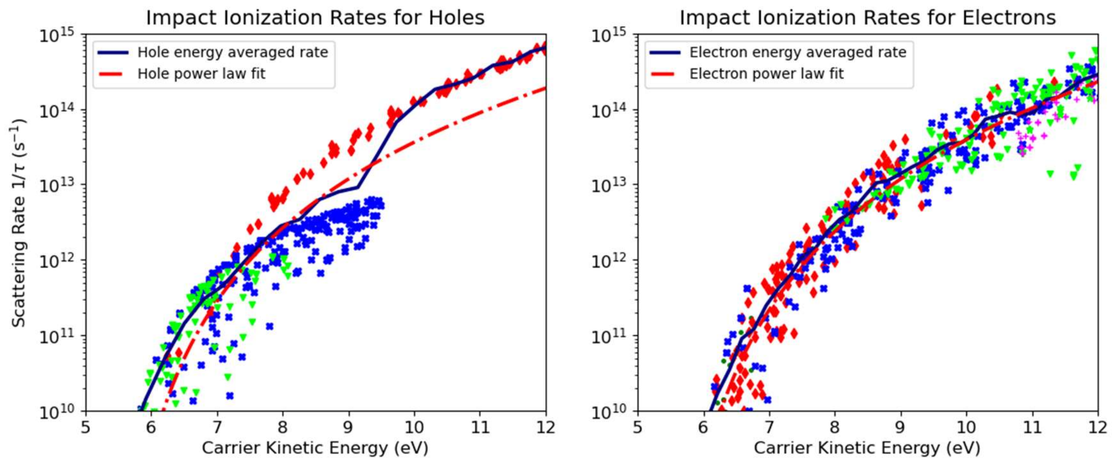

Fig.2: Impact ionization transition rates of holes and electrons in diamond, obtained from Fermi's golden rule as described above. 5 nearest shell sets were used in the overlap integrals. Energy averaged rate (solid blue) and power law fit (dashed red) are also shown.

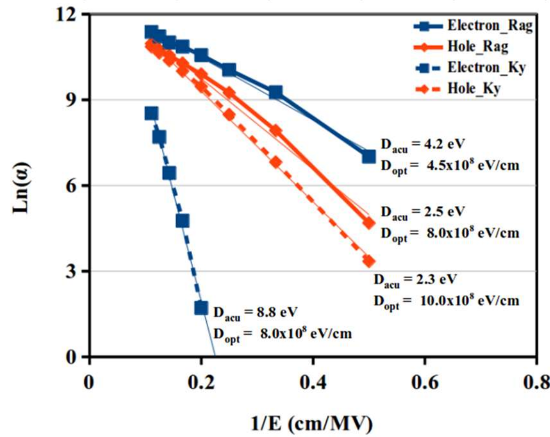

Fig.3: Impact ionization coefficients in diamond, obtained using the energy dependent rates in Fig.2 in full-band cellular Monte Carlo simulations. The solid vs dashed lines were obtained from two different sets of deformation potentials found in literature.

9 783950 473834